Title
Quantitative Microrheology and Modeling of Jammed Ionic Monodisperse Emulsions

Author
Kim, Ha Seong

Publication Date
2019

Peer reviewed|Thesis/dissertation

UNIVERSITY OF CALIFORNIA

Los Angeles

Quantitative Microrheology and Modeling of Jammed Ionic Monodisperse Emulsions

A dissertation submitted in partial satisfaction of the requirements for the degree Doctor of Philosophy in Chemistry

by

Ha Seong Kim

2019

ABSTRACT OF THE DISSERTATION

Quantitative Microrheology and Modeling

of Jammed Ionic Monodisperse Emulsions

by

Ha Seong Kim

Doctor of Philosophy in Chemistry

University of California, Los Angeles, 2019

Professor Thomas G. Mason, Chair

Emulsions are an interesting class of soft materials and have a wide range of practical applications in industry and in consumer goods. To design and tailor the mechanical properties of concentrated emulsions at high droplet volume fractions for specific applications and products, it is helpful to have a good quantitative understanding of emulsion rheology. In this dissertation, we describe the improvements that we have made in the quantitative description of the linear plateau elastic shear modulus, G'_{p}, of jammed monodisperse colloidal emulsions that are stabilized by ionic surfactant molecules.

We have created an improved analytical model, which accurately describes the G'_{p} of jammed monodisperse micro- and nano-scale emulsions. We incorporate entropic, electrostatic, and interfacial (EEI) contributions into a quasi-equilibrium free energy while retaining key aspects of random jamming of deformable droplets, and we calculate G'_{p} via free energy

minimization. This analytical EEI model successfully describes the empirically measured volume-fraction dependent $G'_p(\phi)$ for microscale emulsions and nanoemulsions without any *ad hoc* adjustments to the empirically measured ϕ and with very few adjustable parameters that appear to be universal. In addition, we use this EEI model to identify different ϕ-regimes of jamming caused by electrostatic repulsions and droplet interfacial deformations.

Using jammed monodisperse emulsions as model system, we have improved diffusing wave spectroscopy (DWS) microrheology analysis for quantifying the rheological properties of dense colloidal systems, particularly $G'_p(\phi)$ of jammed repulsive emulsions. We show that we can correct for collective light scattering effects present in highly scattering concentrated colloidal systems through an empirically determined average structure factor and thereby obtain corrected mean square displacements (MSDs), which lead to accurate values of G'_p through the generalized Stokes-Einstein relationship (GSER) of passive microrheology. This advance enables accurate optical microrheology measurements of concentrated emulsions over a wide range of frequencies beyond the capabilities of traditional mechanical rheometers. This approach of correcting DWS MSDs for collective scattering is general and can be applied to other types of highly scattering concentrated colloidal dispersions, not just emulsions.

Motivated by advances in DWS microrheology for repulsive emulsions, we perform DWS microrheology studies on depletion-induced attractive emulsions near and below the jamming volume fraction of hard spheres. By adapting the analytical approach developed for repulsive emulsions, we show that in some limits DWS microrheology of attractive emulsions can be extracted and compare accurately with macroscopic mechanical measurements. We reveal systematic features in an excess MSD that is present only for the attractive emulsions, and we attribute this excess MSD to additional dynamics of clusters of droplets that are only loosely

attached to the main stress-bearing struts of the main gel network of droplets. More theoretical attention is needed in attractive emulsion systems in order to determine how to analyze DWS MSDs and predict the excess MSDs. Interestingly, these measured excess MSDs can be fit using an empirical modified bound Brownian particle equation that we created to describe these extra fluctuations in the DWS signals. This application of DWS microrheology to attractive emulsions herein serves as a basis from which additional DWS microrheology studies of attractive soft colloidal systems can be performed and analyzed.

The dissertation of Ha Seong Kim is approved.

William M. Gelbart

Amy Catherine Rowat

Alexander Michael Spokoyny

Thomas G. Mason, Committee Chair

University of California, Los Angeles

2019

To my wife Soo Jung, family, and friends.

TABLE OF CONTENTS

LIST OF FIGURES

LIST OF TABLES

ACKNOWLEDGMENTS

Without the support I have received from my wife, family, and friends, this dissertation could not have been completed. I would like to dedicate the following section in expressing my sincere gratitude to everyone who has helped me in pursuing my Ph.D at UCLA.

I would like to first thank my Ph.D. advisor, Thomas G. Mason. As a mentor, he has had the biggest influence on my development as a successful scientist in the last 6 years. Not only has he shared his experience, insights, and instrumental skills in solving practical scientific research problems, but has also showed me how to raise interesting scientific questions and think critically. Tom has also been a great friend who has continuously provided support, encouragement, and important career advice during my Ph.D. Without his guidance and support, this dissertation would not have been possible and I would like to thank him again.

I would also like to thank my Prof. Alex Spokoyny, Prof. William Gelbart, and Prof. Amy Rowat for being part of my Ph.D. committee. Special thanks go to Prof. William Gelbart who has agreed to serve on my committee on at the last moments of my Ph.D.

I want to also extend my gratitude to Prof. Frank Scheffold and his group members at University of Fribourg, Switzerland. Without the collaborative work with Prof. Frank Scheffold, the contents of this dissertation would also not have been possible. I also want to thank Prof. Frank Scheffold for inviting me to stay in Fribourg for two short months, during which I have had wonderful experience and learned a lot about light scattering methods. For their contribution with diffusing wave spectroscopy experiments of highly scattering colloidal emulsions, I want to especially thank Dr. Nesrin Şenbil and Dr. Chi Zhang. Also, I thank Dr. Gaurasundar Conley for kindly welcoming me during my short visit to Fribourg and first showing me how to use diffusing wave spectroscopy in Fribourg.

It was also a pleasure to work with fantastic members of the Mason group this past 6 years. I want to thank Dr. Kenny Mayoral who first introduced me to Tom's group. I would also like to thank Mr. Matthew Pagenkopp who has been a great friend who shared valuable knowledge and engaged in numerous discussions about emulsions formulation. I also will forever value the memories and fun times I had with other members in my group: Prof. Manas Khan, Dr. Po-Yuan Wang, Dr. Dimitri Bikos, Mr. Orin Yue, Ms. Yixuan Xu, and Mr. Tianren Yu. I also would like to thank UCLA for the financial support during my graduate studies.

Last but not least, I would like to thank my wife, my parents, my sister, and all other family members for supporting me during my Ph.D. My deepest appreciation goes out to my wife Soo Jung Kim, who has provided me with unconditional support during my pursuit of Ph.D. Soo Jung! Thank you for all your love, support, and encouragement. The last 5 years of my Ph.D. has been a much happier experience for me because of you! I also want to thank my parents and my sister. Without your support, this long journey would have been much more difficult to complete.

The following chapters have been adapted from the versions of the corresponding journal publications: Chapter 1, Kim, H.S. and Mason, T. G. (2017). Advances and Challenges in the Rheology of Concentrated Emulsions and Nanoemulsions. *Adv. Colloid Interface Sci.*, **247**, 397-412. DOI: 10.1016/j.cis.2017.07.002; Chapter 2, Kim, H.S., Scheffold, F., Mason, T. G. (2016). Entropic, Electrostatic, and Interfacial Regimes in Concentrated Disordered Ionic Emulsions, *Rheol. Acta*, **55** (8), 683-697. DOI: 10.1007/s00397-016-0946-3, and section 2.4.5, Braibanti, M., Kim, H. S., Senbil, N., Pagenkopp, M. J., Mason, T.G., Scheffold, F. (2017) The Liquid-glass-jamming Transition in Disordered Ionic Nanoemulsions.; *Sci. Rep.,* **7**, 13879. DOI: 10.1038/s41598-017-13584-w; Chapter 3, Kim, H.S., Senbil, N., Zhang, C., Scheffold, F.,

Mason, T. G. Diffusing Wave Microrheology of Highly Scattering Concentrated Monodisperse Emulsions. (2019). *Proc. Natl. Acad. Sci. U.S.A.* **116** (16) 7766-7771. DOI: 10.1073/pnas.1817029116. Chapter 4 contents have not been published and the current status is *in preparation*. Portions of the herein thesis have been copyrighted previously by the authors in these listed works and are used with permission. Anyone wishing to reproduce any portion of the herein dissertation that is also found in one of these works should contact the respective journals and authors to obtain appropriate permission. Symbols assigned to certain variables in Chapters 1, 2, 3, 4, and 5 may differ according to the specific chapter in which they appear.

VITA

2011	Bachelor of Science, Chemistry, Harvey Mudd College, Claremont, CA, U.S.A.
2013	Master of Science, Materials Science and Engineering, University of Illinois at Urbana-Champaign, Champaign, IL, U.S.A.
2015	Master of Science, Chemistry, University of California, Los Angeles (UCLA), Los Angeles, CA, U.S.A.
2016	Scholarship of the University of Fribourg, Switzerland
2016	Visiting Doctoral Research Student, University of Fribourg, Fribourg, Switzerland
2018	2018 Rheologica Acta Publication Award

PUBLICATIONS

1. **Kim, H.S.**, Şenbil, N., Zhang, C., Scheffold, F., Mason, T. G. "Diffusing Wave Microrheology of Highly Scattering Concentrated Monodisperse Emulsions", *Proc. Natl. Acad. Sci. U.S.A.*, **116** (16), 7766-7771 (2019).

2. Tan, K.W., Werner, J.G., Goodman, M., **Kim, H.S.**, Jung, B., Sai, H., Braun, P.V., Thompson, M.O., Wiesner, U. "Synthesis and Formation Mechanism of All-Organic Block Copolymer-Directed Templating of Laser-Induced Crystalline Silicon Nanostructures", *ACS Appl. Mater. Interfaces*. **10** (49), 42777-42785 (2018).

3. **Kim, H.S.** and Mason, T. G. "Advances and Challenges in the Rheology of Concentrated Emulsions and Nanoemulsions", *Adv. Colloid Interface Sci.*, **247**, 397-412 (2017)

4. Braibanti, M., **Kim, H. S.**, Şenbil, N., Pagenkopp, M. J., Mason, T.G., Scheffold, F. "The Liquid-glass-jamming Transition in Disordered Ionic Nanoemulsions", *Sci. Rep.*, **7**, 13879 (2017).

5. **Kim, H.S.**, Scheffold, F., Mason, T. G. "Entropic, Electrostatic, and Interfacial Regimes in Concentrated Disordered Ionic Emulsions", *Rheol. Acta*, **55** (8), 683-697 (2016). [This publication received the 2018 *Rheologica Acta* Publication Award]

6. Kim, J., Aagesen, L.K., Choi, J.H., Choi, J.; **Kim, H.S.**, Liu, J. Cho, C.-R., Kang, J.G., Ramazani, A., Thornton, K., Braun, P.V. "Template-Directed Directionally Solidified Three-Dimensionally Mesostructured AgCl-KCl Eutectic Photonic Crystals", *Adv. Mater.* **27**, 4551-4559 (2015).

7. Kim, J., **Kim, H.S.***, Choi, J.*, Jeon, H., Yoon, Y., Liu, J., Park, J., Braun, P.V. "Epitaxial Growth of Three-Dimensionally Mesostrcutured Single-Crystalline Cu_2O via Templated Electrodeposition", *Chem. Mater.* **26** (24), 7051-7058 (2014).

8. Fu, M., Chaudhary, K., Lange, J.G., **Kim, H.S.,** Juarez, J.J., Lewis, J.A, Braun, P.V. "Anisotropic Colloidal Templating of 3D Ceramic, Semiconducting, Metallic, and Polymeric Architectures", *Adv. Mater.* **26**, 1740-1745 (2014).

Chapter 1 – Introduction

Reprinted/Adapted from "Advances and Challenges in the Rheology of Concentrated Emulsions and Nanoemulsions." *Adv. Colloid Interface Sci.*, **247**, Kim, H.S. and Mason, T. G. pages 397 - 412 (2017), with permission from Elsevier.

1.1 Emulsions

Emulsions are soft materials composed of droplets of one liquid dispersed in a different immiscible liquid[1]; emulsions are used in many industrial applications and in consumer products[2]. One of the most interesting and appealing aspects of emulsions is that, while being composed entirely of viscous liquids or solutions, they can be made into soft solids that have tunable rheological properties which depend upon their compositions and flow histories. These solid-like properties emerge through the crowding, which can lead to glassy behavior, and ultimately jamming of droplets when the droplet volume fraction ϕ is raised.

Emulsions are typically made through an emulsification process in which an externally applied energetic flow does work against the interfacial tension, σ, causing larger droplets to elongate and rupture via a capillary instability into smaller droplets[3]; emulsification under extreme high-flow conditions can lead to formation of nanoemulsions, which contain droplets having an average radius a < 100 nm[4-6]. During emulsification, some of the applied energy is stored through the creation of additional interfacial area of the droplets which also leads to an increase in the interfacial surface area to volume ratio and also the Laplace pressure $\Pi_L = 2\sigma/a$ of undeformed droplets. Hence, emulsions and nanoemulsions are technically thermodynamically metastable dispersions and susceptible to droplet coalescence[7]. Nevertheless, the addition of

strong stabilizers, such as amphiphilic surfactants, can eliminate changes in the droplet size distribution over many years or even decades. Such long-lived metastable emulsions and nanoemulsions can serve as idealized soft materials for scientific studies. By contrast, lyotropic liquid crystalline phases or "microemulsions" which can contain nanoscale droplets are made by a different pathway than emulsification; such pathways include spontaneous equilibrium self-assembly of droplets that are in effect swollen micelles[8-11] which is a pre-existing form of low-energy emulsification[12]. The "microemulsion" nomenclature is a historical oddity given that the characteristic droplet radii in these equilibrium microemulsion phases have always been in the nanoscale regime[5]. Amphiphilic surfactants, which inhibit droplet coalescence, can be added to emulsions to stabilize droplet interfaces via adsorption, thereby making certain emulsion compositions stable even in the presence of thermal-entropic Brownian excitations. Furthermore, by selecting a liquid for the dispersed droplet phase that is highly immiscible in the continuous liquid phase, Ostwald ripening[7] can be suppressed to a negligible rate; so, some emulsions can remain stable for many years or even decades, making the application of near-equilibrium thermodynamic principles reasonable.

1.2 Factors Affecting Rheology of Concentrated Emulsions

Many different rheological properties of stable model concentrated emulsions have already been explored[13-15]. An emulsion's composition plays a key role in its rheological behavior, not only by influencing the long-term stability of droplets, but also by affecting the kinds of interfacial interactions that exist between droplets as well as the emulsion's overall interfacial structure[16] (see Figure 1.1). In particular, for oil-in-water (O/W) emulsions, the choices of the surfactant and electrolyte concentrations can strongly influence such interactions. All of these factors, in turn, can influence the emulsion's rheological properties. For example,

ionic surfactants, such as sodium dodecyl sulfate (SDS), are a very important class of stabilizers which adsorb at droplet interfaces and typically provide short-ranged screened

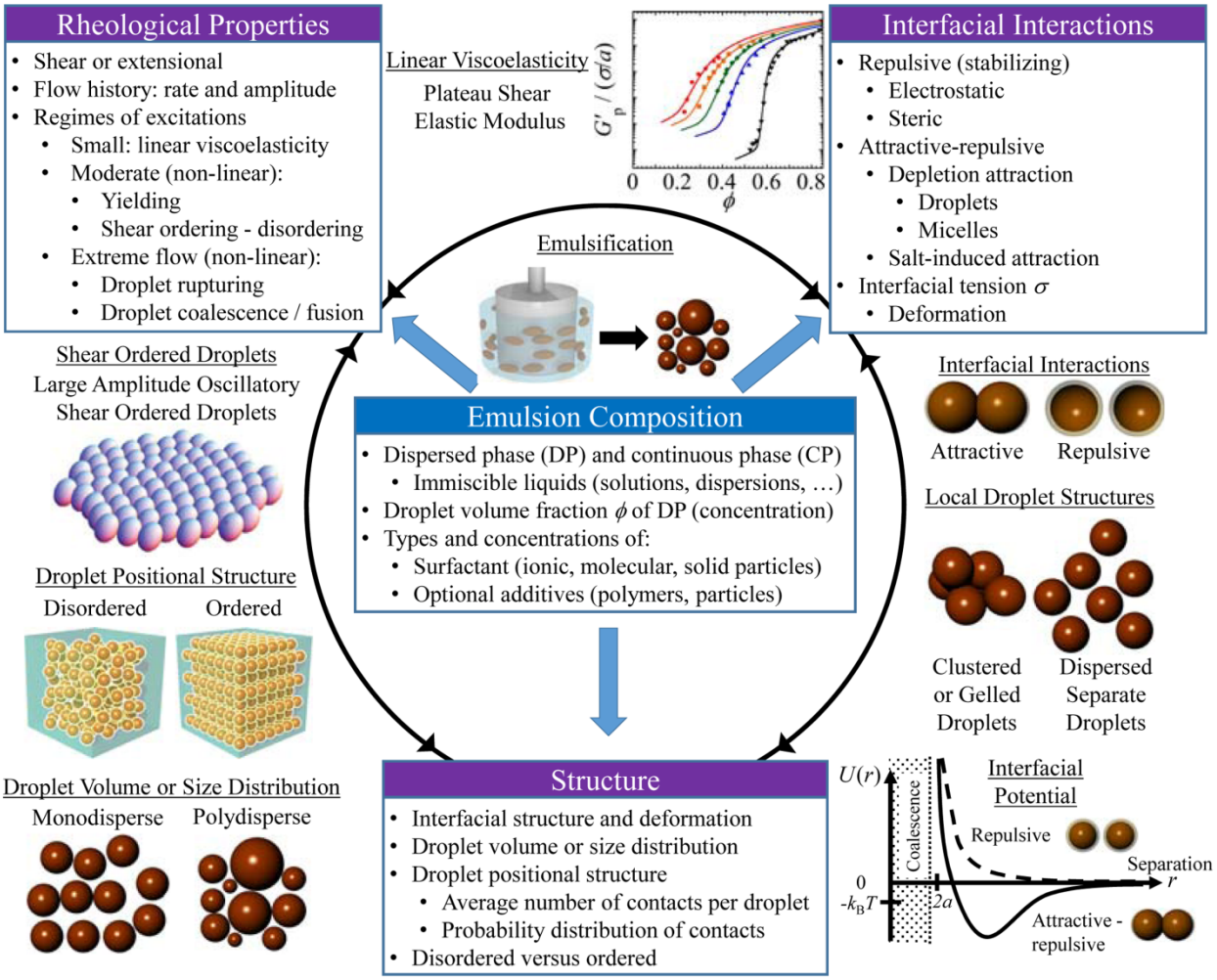

Figure 1.1. A complex array of factors can influence the rheological properties of concentrated emulsions. Traditional non-equilibrium emulsions and nanoemulsions are made by selecting a certain initial composition and imposing a flow that causes larger droplets to be ruptured via interfacial instabilities into smaller droplets. After emulsification, a starting point for describing the interfacial structures in an emulsion is the distribution of droplet volumes which is often expressed as a radial "size" distribution of undeformed spherical droplets. The average size and polydispersity of this distribution, as well as the droplet volume fraction ϕ, can strongly influence the rheological properties of the resulting emulsion. Other factors that can play important roles are: the interactions between droplet interfaces, which typically fall into categories of repulsive or attractive-repulsive, which are often linked strongly to the composition; the prior imposed flow-history and the instantaneous flow conditions during rheological testing; and the droplet positional structure and interfacial deformations of individual droplets. Figure reprinted with permission by Elsevier, Ha Seong Kim, and Thomas G. Mason, copyright 2018.

electrostatic repulsions that yield excellent stabilization against coalescence. Compared to hard interactions at the same ϕ, these electrostatic repulsions lead to an increase of the osmotic pressure; such repulsions also mediate the deformation of droplet interfaces in concentrated emulsions. Additives, such as salts[17-18], can be incorporated into an emulsion's composition and later electrostatic interaction potentials to cause significant interdroplet attractions. Other additives, such as polymers[19-21] or surfactant molecules[15, 22-24] can give rise to clusters and gels of droplets through depletion attractions. An emulsion's droplet size distribution is also of a concern as small droplets are known to induce attractions via depletion effects, as has been shown in idealized binary emulsion systems[25], illustrating the entropic depletion attraction originally predicted by Asakura and Oosawa[26-27]. When secondary attractions, such as those induced by electrostatic or depletion effects, are significantly greater than k_BT, where k_B is Boltzmann's constant and T is temperature, then droplets can flocculate or even gel without coalescing. Such gelation can significantly alter the emulsion's rheological properties[15, 23, 28-29]. In summary, an emulsion's composition can influence its different properties, including its droplet size distribution after emulsification and also droplet-droplet interactions which can affect the emulsion's stability as well as its interfacial structure. These, in turn, can have a very significant influence on the emulsion's rheological properties.

The positional and interfacial structures of droplets in a concentrated emulsion, which are inherently linked to the droplet size distribution through prior emulsification and to the applied flow history, are crucial aspects that govern an emulsion's rheological properties. Here, we define the emulsion's positional structure to be the set of centers of mass of all droplets, and we define the emulsion's interfacial structure to be the set of surfaces of droplet interfaces corresponding to those centers of mass. In the simplest case, the elasticity of concentrated emulsions is mostly

affected by packing or jamming structure, which depends on ϕ. As ϕ is increased by crowding droplets, which can be achieved by applying an osmotic pressure, the droplet interfaces begin to significantly deform, leading to elasticity. Historically, hard spheres that have been rapidly concentrated form a disordered positional structure known as random close packing (RCP)[30]. However, the volume fraction associated with RCP, ϕ_{RCP}, has been more precisely defined in recent work, leading to the concept of maximal random jamming (MRJ)[31]. The volume fraction associated with MRJ of hard monodisperse spheres is $\phi_{MRJ} \approx \phi_{RCP} \approx 0.646$. For disordered, ionic, monodisperse emulsions, the onset of elasticity has been associated with ϕ_{MRJ}, after correcting for screened electrostatic repulsions[32-35]. Polydispersity, which is defined as $P_a = \delta a/a$ where δa is the standard deviation of the radial size distribution, is known both experimentally[32-33, 35-39] and through simulation[40] to increase ϕ_{MRJ}, showing that an emulsion's droplet size distribution is interrelated to both its microscopic structure and its rheological properties. The prior flow history of an emulsion, even at flow rates well below those used for emulsification, can also influence its structure as well as its rheological properties. Certain disordered emulsions of uniformly sized droplets have been shown to order under applied flow through shear-induced ordering[41-43]. The volume fraction associated with jamming in such ordered structures is significantly higher than ϕ_{MRJ}; hexagonal close packing is known to have $\phi_{HCP} \approx 0.74$ [44]. Also, application of strong flow in certain rheological measurements (*e.g.* steady shear at high shear rates) can actually induce further emulsification of larger droplets into smaller droplets[45-46] and affect polydispersity. Thus, for some types of emulsions, it may not even be possible to probe certain rheological properties without actually changing the fundamental interfacial structures within the emulsion.

1.3 Monodisperse Emulsions and Nanoemulsions

Monodisperse emulsions and nanoemulsions, which exhibit relatively low polydispersities, have led to significant improvements in the quantitative understanding and description of emulsion rheology[5, 32-33, 35, 46-47]. By carefully controlling composition and measuring rheological properties, a reasonable quantitative understanding of the linear rheological properties of disordered uniform O/W emulsions and nanoemulsions, which have screened charge interfacial repulsions through ionic surfactants, has been achieved[32, 48-49].

Only a handful of emulsification methods provide direct approaches for making monodisperse emulsions having low polydispersity $P_a \leq 0.1$. Some examples of direct methods include controlled shear rupturing[50-51], membrane or porous glass emulsification[52-53], and classic Bragg extrusion of a dispersed phase through a capillary[54-55], which is now effectively used in a wide range of more complex microfluidic and lab-on-a-chip platforms[56-58]. For some of the above methods, the gap or channel sizes, as well as the peak flow rate, often limit the smallest attainable droplet sizes to the microscale range, and relatively small volumes are produced at high droplet volume fractions.

Size fractionation of emulsions produced from traditional emulsification approaches, which typically have larger polydispersities but offer larger processing volumes, offers an alternative route in preparing monodisperse emulsions in large enough volumes to be studied through traditional mechanical rheometry. Depletion flocculation[59] is effective for size-fractionating larger colloidal droplets, but ultracentrifugal droplet fractionation[46-47] is typically a more useful and practical method for nanoemulsions having $a < 100$ nm, provided that a mass density mismatch between the dispersed phase and the continuous phase exists to drive sedimentation or creaming of the droplets. In this latter method, uniform nanoemulsions, which

have $P_a \approx 0.10$ - 0.15, have been obtained from a crude polydisperse nanoemulsion by repeatedly ultracentrifuging, splitting the concentrated elastic plug that forms, and diluting[46].

Whether nanoscale or microscale, monodisperse colloidal emulsions that are dilute can then be subsequently concentrated in a rapid manner using applied osmotic pressure Π. If a mass density difference exists between the continuous and dispersed phases, then centrifugation or ultracentrifugation may be preferred; alternatively, if a mass density difference does not exist, then dialysis using solutions having high Π, for instance a polymer solution, can also be used to concentrate the emulsion and raise its ϕ. If Π is applied rapidly to quench-in disorder, which is often relatively simple to do with centrifugal methods, then even monodisperse droplets (*i.e.* having $P_a \approx 0.1$ or less) commonly go through a glass transition and then a jamming transition while retaining a disordered droplet positional structure, as the droplet volume fraction ϕ is raised.

1.4 Linear Viscoelasticity of Concentrated Repulsive Emulsions

1.4.1 Linear Shear Elastic Moduli of Disordered Concentrated Emulsions

In this section, we consider the linear shear viscoelastic response of relatively simple concentrated emulsions in which the interfaces of all droplets have short-range repulsive interactions with the interfaces of other nearest neighboring droplets; emulsions composed of attractive droplets will be addressed in a later section. Highly concentrated emulsions subjected to a small strain, below the yield strain, are known to exhibit elasticity which arises from the work done against the interfacial tension as the droplets deform.

This shear elasticity can be quantified by measurements of frequency-dependent complex linear modulus $G^*(\omega) = G'(\omega) + iG''(\omega)$, where $G'(\omega)$ is the storage modulus and $G''(\omega)$ is the loss modulus. A mechanical rheometer (Figure 1.2(a)), often the instrument of choice in

measuring viscoelasticity, can be used to measure $G^*(\omega)$ by performing a linear oscillatory frequency sweeps at small strain amplitudes γ_0. In the measurement, the mechanical rheometer applies a small-amplitude sinusoidal strain $\gamma(t) = \gamma_0 \sin(\omega t)$ to the emulsion and measures the sample response of the perturbation in the form of sinusoidal stress $\tau(t)$ which lags the input strain signal by some phase δ as shown in Figure 1.2(b). This sinusoidal stress is related to the applied strain where $\tau(t) = \gamma_0[G'(\omega)\sin(\omega t) + G''(\omega)\cos(\omega t)]$, such that non-negative $G'(\omega)$ and $G''(\omega)$ can be obtained. For concentrated emulsions, $G'(\omega)$ exhibits a dominant plateau well above $G''(\omega)$ at intermediate ω, and it is possible to define a plateau elastic shear modulus G'_p.

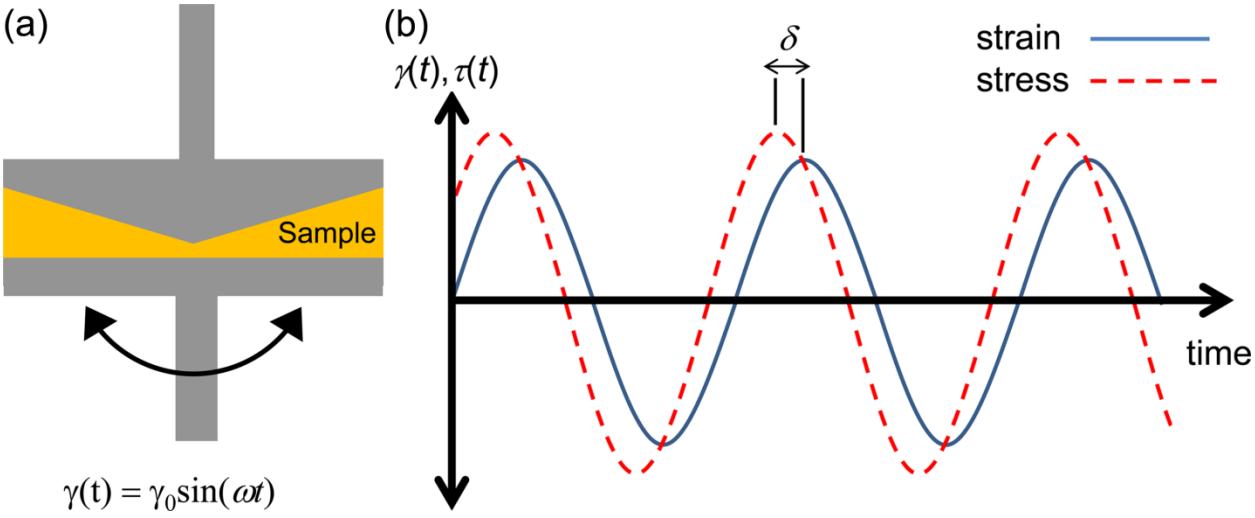

Figure 1.2. Mechanical rheometer geometry and oscillatory rheology test. (a) A schematic representation of cone and plate rheometer geometry in a strain-controlled rhometer, which was used for oscillatory rheology test of concentrated emulsions. (b) Typical input and output signal of oscillatory rheology test. A sinusoidal strain signal (solid line) of a fixed frequency is applied to the sample and the sample response is measured in terms of sinusoidal stress signal (dashed line) with a phase lag δ with respect to the input. Using the amplitude and the phase lag information, components of the complex shear modulus G^* can be found.

In early work, Princen *et al.*[36-39] measured the complex linear shear modulus of concentrated polydisperse emulsions and attempted to fit $G'_p(\phi)$ using empirical models. However, no direct link could be easily made to theory or microscopic models because of the

uncontrolled polydispersity in the droplet size distribution. Measurements, performed by Mason *et al.*[15, 32-33, 35], of the ϕ-dependence of linear plateau shear elastic modulus $G'_p(\phi)$ of disordered concentrated depletion-fractionated emulsions led to a better understanding of the observed elasticity. They showed that colloidal monodisperse repulsive polydimethylsiloxane (PDMS) O/W emulsions stabilized by SDS having four different radii a could be described by a semi-empirical $G'_p(\phi_{eff}) \sim (\sigma/a)\phi_{eff}(\phi_{eff} - \phi_c)$ for $\phi > \phi_c$ [32-33, 35]where the critical volume fraction ϕ_c is $\phi_{MRJ} \approx 0.646$ for monodisperse spheres[31, 60]. To account for screened electrostatic repulsions between the anionically stabilized droplets, Mason *et al.* used an effective volume fraction $\phi_{eff} \approx \phi[1 + (h_f/2a)^3]$, where h_f is a ϕ-dependent film thickness between the two droplet surfaces having values ranging from a few to about ten nanometers. This effective volume fraction crudely accounted for the contribution of the electrostatic screened charge contribution around the interfaces of the spherical droplets which also had a Debye screening length λ_D of a few nanometers. The specific ϕ-dependence of h_f was chosen in an *ad hoc* manner to cause data for $G'_p(\phi_{eff})$ taken at four different droplet sizes to overlap onto a master curve[32-33, 35] and was not clearly linked to a fundamental theory. However, this way of accounting for the stabilizing repulsions was reasonable as an empirical analytical approach, and the resulting master curve linked the onset of emulsion elasticity to the jamming of disordered droplets at ϕ_{MRJ}. In comparison with Princen's earlier measurements, the lower volume fraction associated with the onset of elasticity found by Mason *et al.* highlighted the importance of effects of droplet size polydispersity on a concentrated emulsion's elasticity. Furthermore, the frequency dependence of Mason's measured shear moduli $G^*(\omega)$ at ϕ_{eff} near but below ϕ_c closely resembled that of glassy hard-sphere colloids[61], highlighting the importance of entropy and thermal excitations in colloidal emulsion systems.

1.4.2 Glass Transition versus Jamming of Droplets in Colloidal Emulsions

The following brief discussion emphasizes the consequences of entropic excitations in concentrated monodisperse emulsion systems in which the droplet volume fraction has been raised rapidly so the system of droplets remains disordered, precluding equilibrium entropic crystallization via the colloidal disorder-order transition[62]. Based on measurements of $G^*(\omega)$ for colloidal monodisperse disordered concentrated emulsions having ϕ_{eff} near but below ϕ_{MRJ}, Mason *et al.*[61] transferred the notion of the colloidal glass transition in entropic systems of hard spheres[63] to the elasticity of concentrated emulsions[32, 35]. Even after accounting for charge-screened electrostatic repulsions, Mason observed that a dominant plateau shear modulus G'_p persisted to the lowest frequencies measured for ϕ_{eff} just below ϕ_{MRJ}. Ultimately, $G^*(\omega)$ of concentrated emulsions developed a low-frequency relaxation visible in the measurement range for ϕ_{eff} below $\phi_g \approx 0.58$, where ϕ_g is the volume fraction associated with the ergodic-nonergodic glass transition[16]. Thus, Mason's measurements were consistent with the notion of a zero-frequency elastic shear modulus that is dominantly entropic in origin for $\phi_g < \phi_{eff} < \phi_{MRJ}$[32, 35]. Here, we refer to this range of $\phi_{eff,}$ below jamming but above the glass transition where droplet dynamics are non-ergodic yet droplets are not yet jammed, as the glass regime. In addition, a well-defined G'_p at a non-zero frequency still was measured even for ϕ_{eff} somewhat below ϕ_g, although only a portion of the slow glassy relaxation appeared in the measurement range of ω, ultimately cutting off the reported $G'_p(\phi_{eff})$ towards low ϕ_{eff}. Here, we refer to this range of ϕ_{eff} as the near-glass regime. Even in the absence of applied mechanical excitations, slow structural evolution (*i.e.* annealing) and aging of concentrated emulsions over a relatively narrow range of ϕ_{eff} can exist as a consequence of entropic excitations and local variations in the structure[64-65]; these effects are most pronounced in the near-glass regime, where dynamical heterogeneities are

frequently and readily observed[66]. Thus, in the glass and near-glass regime, G'_p arises from excluded volume effects and increases with ϕ as a consequence of increased caging of droplets by their neighbors without significant droplet deformation[35]. In the near-glass regime, entropic effects dominate, and entropically driven changes in the positional structure of the droplets, analogous to hard-sphere colloids, leads to a low frequency glassy relaxation that has been modeled by glassy power laws inspired by mode coupling theory[67]. For ϕ_{eff} well below ϕ_g, the elastic shear response due to entropic excluded volume effects in dense systems of droplets becomes small compared to the viscous response of the liquids in the emulsion, and ultimately G'' dominates. While the above discussion refers to volume fractions for perfectly monodisperse spheres, these volume fractions may not be the same when significant droplet size polydispersity exists. The way in which polydispersity influences all of the quantitative aspects of the glassy behavior and the jamming behavior of dense systems of droplets remains as one of the most interesting and difficult challenges in emulsion rheology.

1.4.3 Entropic-Interfacial Model

To model the measured $G'_p(\phi)$ of disordered uniform colloidal emulsions, Mason introduced a quasi-equilibrium approach of free energy minimization[32], which has been more recently highlighted in a journal article by Mason and Scheffold[48]. Prior models related to the elasticity of colloidal dispersions had established relations that were limited to either disordered hard spheres[68], in which deformation of the interfaces of the spheres was not allowed, or to perfect crystals of droplets, respectively, without regard to entropy or stabilizing interfacial repulsions[69]. Using basic notions from equilibrium statistical mechanics and prior studies of concentrated colloidal hard spheres, Mason developed expressions for entropic and interfacial

free energy per droplet (F_{ent}/N and F_{int}/N) while neglecting electrostatic interactions. The two free energy expressions are:

$$F_{ent} / N = -3k_B T \ln\left(\phi_c + \phi_d - \phi - \alpha\gamma^2\right) \tag{1.1}$$

$$F_{int} / N = 4\pi a^2 \xi\sigma\phi_d{}^2 \tag{1.2}$$

where ϕ_d is a deformation volume fraction arising from weak deformations of the droplet interfaces, N is the number of droplets in the emulsion system, γ is the shear strain amplitude, and α and ξ are dimensionless parameters related to shear and configurational effects, respectively[32, 48]. The entropic contribution to the free energy per droplet given by equation (1.1) was obtained by considering the free volume expressions for hard colloidal spheres near jamming[68]. The interfacial contribution to the free energy per droplet given by equation (1.2) was obtained by assuming an average deformed droplet structure caused by crowding of neighboring droplets. In this approach, the emulsion's linear elastic shear modulus can be modeled by considering an average local microstructure and an effective number of regions of closest approach of a given droplet's interface with the interfaces of neighboring droplets or an average coordination number, $\langle z_c \rangle \approx 6$, for disordered systems[60]. Mason *et al.* proposed that $G'_p(\phi)$ can be deduced by minimizing a total free energy per droplet, the sum of the two free energies above, with respect to the deformation volume ϕ_d and then minimizing the resulting free energy expression with respect to the shear strain γ. The obtained expression for $G'_p(\phi)$ is:

$$G'_p(\phi) = 6\alpha\xi\frac{\sigma}{a}\phi[(\phi - \phi_c) + \sqrt{(\phi - \phi_c)^2 + \phi_\Gamma{}^2}] \tag{1.3}$$

where $\phi_\Gamma{}^2 = (3k_B T/a^3)/(2\pi\xi\sigma/a)$ is defined as the square of the dimensionless volume representing ratio of entropic and interfacial energy density scales[32, 48]. Good agreement with

measurements were achieved using model adjusted parameter values of $\alpha = 0.74 \pm 0.32$ and $\xi = 0.14 \pm 0.06$. In the athermal limit where entropy becomes unimportant (*i.e.* $\phi_\Gamma \rightarrow 0$ as $T \rightarrow 0$ or for non-colloidal systems), equation (1.3) reduces to $G'_p(\phi) = 12\alpha\xi(\sigma/a)\phi(\phi-\phi_c)$, which is consistent with the semi-empirical formula used to fit $G'_p(\phi_{eff})$ for $\phi_{eff} \geq \phi_{RCP} \approx 0.64$ beyond the jamming limit[32-33, 48]. Furthermore, the inclusion of the entropic term provides a smooth crossover to the shear modulus of the colloidal glass of droplets, which later Ikeda *et al.* has also shown when describing glassy systems of colloidal soft uniform objects[70-71].

1.4.4 Electrostatic-Interfacial Model

While the effects of the short-range stabilizing screened charge repulsion were already apparent in $G'_p(\phi)$ of microscale colloidal emulsions, additional experiments with fractionated nanoemulsions showed that the effect of this repulsion could become extremely pronounced, such that strong elasticity could be obtained in O/W emulsions that are mostly composed of water at ϕ far below ϕ_{MRJ}[46]. This finding is consistent with the higher surface-area-to-volume ratio of nanoemulsions, as the droplet radius more closely approaches the Debye screening length λ_D, which is fixed by composition. By shifting the measured $G'_p(\phi)$ of the nanoemulsions, causing it to overlap onto the known master curve for $G'_p(\phi_{eff})$, and using a simple model that connected the interfacial interactions to the elastic shear modulus using $\langle z_c \rangle \approx 6$, Wilking and Mason[46] deduced the distance-dependent interaction potential, $U(h)$, showing a repulsive Debye form: $U(h) \sim \exp(-h/\lambda_D)/(h)$, where h is the separation between proximate droplet interfaces. Thus, they effectively turned a macroscopic rheometer into a surface forces apparatus, provided a series of rheological measurements covering a range of ϕ are made. Moreover, the measurements and model presented by Wilking and Mason set the stage for eliminating the prior *ad hoc* assumptions related to the ϕ-dependent film thickness and treating the electrostatic

contributions in ionically stabilized emulsions properly.

Expanding on the model introduced by Wilking and Mason that deduced $U(h)$ from $G'_p(\phi)$, Scheffold *et al.* considered the problem in reverse by predicting $G'_p(\phi)$ given a screened-charge $U(h)$ through a similar kind of near-equilibrium energy minimization approach that had been previously employed to link interfacial and entropic energetic contributions to G'_p. This model involved a free energy that incorporated both a screened-charge repulsive electrostatic energy and an elastic interfacial energy arising from weak deformations above the onset of elasticity near the jamming point yet for $\phi \leq 0.85$, below the bi-liquid foam-like limit[49]. By combining the two energies and taking the electrostatic pair potential to be $U_{elec}(h) = 2\pi a \psi_0 \varepsilon_0 \varepsilon_r \exp(-\kappa h)$, where κ is the inverse Debye length λ_D^{-1}, ψ_0 is the electrostatic surface potential, and ε_0 is the permittivity of vacuum[62], Scheffold *et al.* calculated $G'_p(\phi)$ of nanoemulsions and micro-scale emulsions. These calculations matched the experimental results without any need to create an effective volume fraction, ϕ_{eff}, for volume fractions $\phi \geq \phi_c$ beyond jamming. This marked an important improvement over a limited range of ϕ, yet predictions for $G'_p(\phi)$ for colloidal emulsions in the glassy regime, below jamming, could not be made because entropic effects from thermal fluctuations were omitted from that model.

1.4.5 Structural Aspects: Simulations and Measurements

Although the analytical models describing macroscopic rheometry measurements of $G'_p(\phi)$ for ionically stabilized, disordered, uniform, oil-in-water emulsions have been developed, it nevertheless assumes a relatively simple local average structure around a given droplet. For instance, the local coordination number $\langle z \rangle$ has been assumed to be independent of ϕ, and the separation distance h between droplet interfaces near the regions of closest approach is only an average, rather than a distribution[32, 48]. Despite these simplifications, the analytical model does

well in describing the measured trends over a very wide range. Early simulations by Lacasse *et al.*[35, 72], which described disordered concentrated emulsions using a local coordination number *z*-dependent anharmonic pair-potential, have also been used to explain the shear viscoelasticity of concentrated emulsions. Lacasse *et al.*[35, 72] demonstrated a good agreement between the measured $G'_p(\phi_{eff})$ and simulations for ϕ beyond $\phi_{RCP} \approx \phi_{MRJ}$, yet these simulations neglected electrostatic interactions and entropic contributions. These simulations by Lacasse *et al.* also predicted the non-affine motion of the disordered droplets under small shear strain[72], which recently has been observed using confocal microscopy on sheared emulsion droplets[73]. While Lacasse *et al.* established that non-affine motion of droplet centers at small shear strains was consistent with the observed increase $G'_p(\phi)$ above jamming, a later model, which accounts for the contribution by the droplet's non-affine and affine displacement to the emulsion's moduli, has also been developed[74]. However, this later model does not account for entropic excitations, which were also left out of Lacasse *et al.*'s simulations; such entropic excitations can be important for emulsions of colloidal droplets in the glassy regime and weakly jammed limit, and entropic excitations are captured in near-equilibrium energy minimization models.

Measurements of droplet microstructures in concentrated emulsions have been obtained and verified through experimental measurements, particularly through the use of confocal microscopy and light scattering in quiescent states and also under flow. Real-space 3D imaging, as exemplified by the confocal fluorescence micrograph in Figure 1.3(a)[75], is providing increasingly more 3D interfacial and positional structural information for both jammed[75-79] and glassy[80] emulsion systems. From the 3D micrograph, Voronoi tessellation, which is a set of Voronoi cells or convex polyhedron formed by planes perpendicularly bisecting the vectors joining the center of a given droplet to other neighboring droplets, can be constructed as seen in

Figure 1.3(b), to determine characteristics of the local droplet positional structure using known analytical methods[81]. Using the Voronoi tessellation methods, the probability distributions of local coordination number, PDF(z), and average local number of contacts $\langle z \rangle$ for jammed emulsions at $\phi > \phi_c$ shown in Figure 1.3(c) and (d), have also been measured. This experimentally determined PDF(z) reveal a peak for ϕ near and just above ϕ_{MRJ}, but this does not exactly match the peak predicted by simulation for disordered jammed systems (see Figure 1.3(c)). Such differences are likely a consequence of polydispersity in the experiments, and also differences in the effective interactions between droplet interfaces, which is not completely hard in the experiments. However, the measured $\langle z(\phi) \rangle$ as a function of droplet volume fraction from confocal microscopy has been found to closely match to prior simulation results by Lacasse *et al.* for disordered monodisperse emulsions[35, 82]. These experiments reasonably match the simulated $(\phi - \phi_{MRJ})^{1/2}$ dependence for $\phi > \phi_{MRJ}$ of $\langle z \rangle$ above the $z_c \approx 6$ at ϕ_{MRJ} (see Figure 1.3(d)). However, $\langle z \rangle$ itself only ranges from about 6 at ϕ_{MRJ} to about 12 for highly concentrated droplets approaching the bi-liquid foam regime, so any ϕ-dependent rheological properties, such as elastic shear modulus or yield stress, that have $\langle z \rangle$ as contributing factor are typically only very weakly modified by the ϕ-dependence of $\langle z \rangle$ at and above ϕ_c. Other measurements that have been obtained via real-space imaging include: force distributions[76], droplet deformations[76], and droplet movements as a consequence of shear[73, 83].

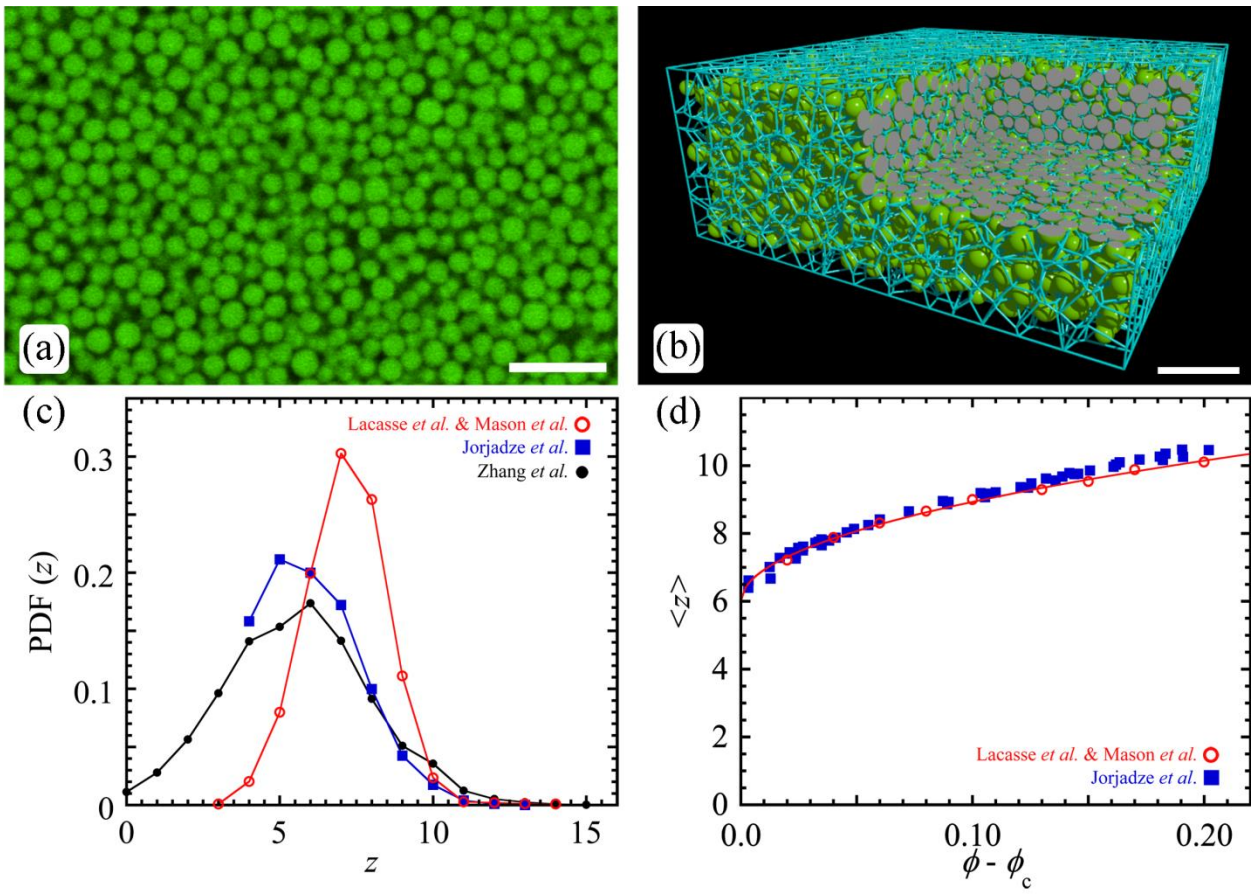

Figure 1.3. Quiescent 3D structures and structural characteristics of concentrated emulsions from optical microscopy experiments and simulations. (a) Confocal micrograph section of a concentrated monodisperse emulsion having $a = 1.05$ μm with $P_a \approx 0.15$ at $\phi \approx 0.646 \pm 0.014$ from Zhang *et al.*[75] (b) 3D reconstruction and analysis of the droplet positions with lines representing edges of Voronoi cells around the droplet centroids. Scale bars in (a) and (b) are ≈ 10 μm. (c) Normalized probability distribution function (PDF) of local coordination number z (*i.e.* number of contacts, number of faces on Voronoi cells) per droplet above the jamming volume fraction $\phi_c \approx \phi_{MRJ}$. Black circles represent measurements from Zhang *et al.*[75] and blue squares represent measurements from emulsions with $a = 3.3 \pm 0.74$ μm at $\phi \approx 0.664$[79], both near the jamming point. Lines guide the eye. Simulations by Lacasse *et al.*[35, 72] at $\phi = 0.66$, slightly above the jamming point, preceded measurements by Jorjadze *et al.*[79] and Zhang *et al*[75]. (d) Average local coordination number $\langle z \rangle$ as a function of $\phi - \phi_c$. Red open circles are simulation results for deformable monodisperse spheres at $\phi = 0.66$, slightly above the jamming point, from Mason *et al.*[35] and Lacasse *et al.*[72], fitted by a red line, showing the $(\phi - \phi_{MRJ})^{1/2}$ dependence of the difference of the average local coordination number with that at jamming, $\langle z \rangle - \langle z_c \rangle$, beyond the jamming point, where $\langle z_c \rangle = 6$ at ϕ_{MRJ}. Blue squares represent measurements as in part (c). Figure reprinted with permission by Elsevier, copyright 2018.

1.4.6 Optical Microrheology Measurements

Measurements of $G^*(\omega)$ have been made using diffusing wave spectroscopy (DWS), an optical microrheological technique, and have enhanced measurements at high ω. DWS measures time-dependent mean square displacements of droplets in concentrated emulsions, from which approximate values of $G^*(\omega)$ can be obtained using generalized Stokes-Einstein relation[67, 84]. Using DWS, $G^*(\omega)$ can be measured at high frequencies that are many orders of magnitude beyond the limit of mechanical rheometers which are often limited to $\omega \leq 10^2$ rad/s. Measurements of $G^*(\omega)$ on monodisperse emulsions using DWS showed $G'(\omega) \sim \omega^{1/2}$ at high frequencies. This scaling relation has been ascribed to an anomalous viscous loss effect[85], but recent theory, based on analyzing relaxation modes of jammed emulsions, was also found to give the scaling relation[86]. In the future, quantitative comparisons of the predicted magnitudes of G' at different ϕ, not just its $\omega^{1/2}$ scaling with experiments are therefore necessary in order to determine the extent of the applicability of these two different models. Moreover, the low-frequency relaxation behavior and loss modulus of concentrated emulsion systems over a wide range of droplet volume fractions and interactions are still interesting to investigate.

1.5 Rheology of Attractive Emulsions

For some emulsion compositions, the interaction potential between droplet interfaces can have a strong secondary attractive well, typically deeper than thermal energy k_BT, yet there still remains a shorter-range repulsion that effectively prevents droplet coalescence. Such attractive emulsions can form isolated flocs or clusters, or, for very deep secondary attractive wells, they can even gel, yielding highly interconnected networks of droplets depending on ϕ. Gelation of droplets in emulsions has been observed over a wide range of ϕ, including at very low ϕ through

diffusion limited or reaction limited processes[18, 87-88]. In attractive emulsions, if a deep well exists in the potential as a consequence of the secondary attraction, neighboring droplets remain proximate even when ϕ drops well below ϕ_{MRJ}. This can lead to important differences in rheological properties of attractive emulsions compared to purely repulsive ones. Due to the fundamental differences in droplet interactions and structures formed, which can be very sensitive to the history of applied flow and even gravitational effects, attractive emulsions have been observed to have significantly different rheological behavior than their purely repulsive counterparts[15, 23, 89-90].

1.5.1 Linear Plateau Elastic Storage Modulus of Attractive Emulsions

A key initial comparative study of attractive and repulsive emulsions in the concentrated regime was made by Mason *et al*. on fractionated monodisperse O/W emulsions (a = 250 nm, P_a ≈ 0.1). Their linear viscoelastic behaviors, including $G'_p(\phi)$, were measured at lower SDS concentrations (~ 10 mM) very close to the critical micelle concentration (CMC), corresponding to purely screened-charge repulsions, and also at very large SDS concentrations (~ 200 mM) well above the CMC, leading to strong secondary attractive well via surfactant micelle-induced depletion, as shown in Figure 1.4[15, 23]. A dominant $G'_p(\phi)$ of attractive emulsions extended down to ϕ well below that of the repulsive emulsions that had the same size distribution. At larger ϕ, $G'_p(\phi)$ of attractive and repulsive emulsions were about the same, although the G'_p of the attractive systems were observed to be slightly smaller over a range of ϕ between about ϕ_{MRJ} and ϕ_{HCP}, potentially as a result of a reduction in the Debye screening length that would be expected to occur at higher electrolyte concentrations. However, at even higher ϕ, towards the bi-liquid foam limit, the data for $G'_p(\phi)$ for both attractive and repulsive emulsions largely overlapped, indicating that droplet deformations, overcoming the Laplace pressure of the droplets, in very

dense emulsions systems governs the G'_p of both. Although other rheological measurements, such as strain and frequency sweeps, were made on depletion-induced attractive emulsion systems at the same time as $G'_p(\phi)$ by Mason *et al*., this data was not published until later[23]. Overall, Mason showed that depletion-induced attractions in emulsions, which could in principle be created by a wide range of depletion agents, could have a very important impact on their rheological properties.

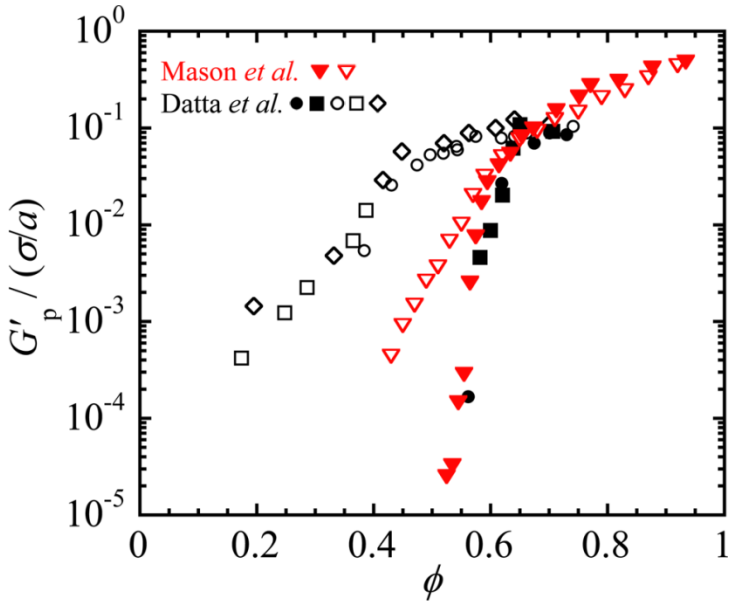

Figure 1.4. Linear plateau shear elastic moduli of attractive emulsion systems. Linear plateau elastic shear moduli G'_p in units of Laplace pressure scale σ/a as a function of droplet volume fraction ϕ of attractive (solid symbols) and repulsive (open symbols) silicone emulsions. Red triangle points are a set of experiments with SDS-stabilized PDMS emulsions dispersed in water, whereas other black points are measurements from non-ionic Pluronic P105 stabilized silicone emulsions suspended in formaldehyde. The attractive emulsions are denoted in open symbols while the non-attractive emulsions are denoted by solid symbols. The average radii a in nm of emulsions are: 250 (triangles), 128 (circles), 106 (squares), 100 (diamond). The attractive energies U_{attr} are: 21 k_BT (triangles), 9 k_BT (circles), 7 k_BT (squares), 9 k_BT (diamonds). Figure data is adapted from Mason *et al*.[15] and Datta *et al*.[23] Figure reprinted with permission by Elsevier, copyright 2018.

Later, in a similar set of experiments, Datta *et al*. measured $G'_p(\phi)$ of polymer micelle-induced depletion-induced attractive emulsions ($a \sim 100$ nm, $P_a = 0.30 \sim 0.35$) at $\omega = 1$ rad/s and also found attractive emulsions to exhibit large elasticities below $\phi < \phi_c$ using $U_{attr} = 7$ - 9

k_BT as shown in Figure 1.4(a)[23]. While the data for the repulsive emulsion systems by Datta *et al*. and Mason *et al*. overlap reasonably well, there are significant differences in the behavior of $G'_p(\phi)$ between these two different attractive emulsions at lower ϕ, even as both have dominant G'_p that extend to ϕ far below ϕ_{MRJ} as a consequence of the attractions. There are many potential reasons for the observed differences: the polydispersities of the two systems were different, the shapes of the interfacial interaction potentials were not identical in all regards, the methods of gelling and loading the samples into the rheometer were not entirely the same, and even gravitational effects could have played a role, since attractive emulsions that are not density matched can readily compact (causing evolution of G'_p due to the resulting compositional inhomogeneity) after loading into a rheometer.

In other work, Erramreddy and Ghosh[91] report a rise and then a drop in G' as a function of increasing SDS concentrations used in emulsification of $\phi = 0.4$ O/W silicone nanoemulsions, but quantitative interpretation of this is somewhat difficult by polydispersity and uncertainties in the remaining concentration of SDS in the continuous phase and droplet sizes in the emulsified sample. For a different emulsion system in which gelation is induced by thermoresponsive oligomeric chemical linkers, Helgeson *et al*. reported significant values of $G'_p(\phi)$ for $\phi > 0.14$ for a = 21 nm emulsions[29], further indicating attractive emulsions can exhibit elasticity in at lower concentrations due to gelation networks. Modeling the elasticity of attractive systems is challenging because the nature of the range of the attractions, as well as the changes in droplet structure and local heterogeneities in the density of droplets, could alter the results. Pre-shear conditions after introducing the attractions and sample handling effects (*e.g.* creaming for non-density matched droplets) could be very important for these systems and make comparisons between measurements of different groups difficult. However, the effect of attractions on shear

elasticity of concentrated emulsions have not fully been explored quantitatively and contrasted against that of repulsive emulsions. Further work is thus necessary to understand the elasticity of attractive emulsions.

1.6 Overview

Rheological measurements of concentrated monodisperse emulsions have led to key advances in the basic scientific understanding of dense glassy and jammed systems of deformable objects. Simulations and theoretical models are now in agreement with some of the simplest rheological properties of certain well-controlled emulsions and nanoemulsions that have highly uniform size distributions yet are disordered. Optical microrheology measurements have enabled understanding of high frequency rheology of monodisperse emulsions, such as the $\omega^{1/2}$ scaling of shear elasticity of concentrated emulsions. It is also shown that depletion-attracted emulsions exhibit a different behavior from the repulsive counterpart in $G'_{\mathrm{p}}(\phi)$ near the jamming point, which can be attributed to the formation of gels.

Despite these achievements, there still exist improvements to the quantitative understanding of monodisperse emulsion rheological properties which can further aid understanding of jammed emulsions. A model which can describe measurements using empirically measured ϕ while simultaneously describing the glassy entropic affects are needed. Improvements to DWS microrheology method, which go beyond showing qualitative trends and $\omega^{1/2}$ scaling relation and enable quantitatively accurate measurements of G' at different ϕ, are desirable for quantitative understanding of high-frequency rheology beyond the limit of traditional mechanical rheometers.

In the following chapters, we present recent studies, which have led to an improved quantitative rheological understanding of jammed ionic monodisperse emulsions. In Chapter 2,

we introduce a new analytical model which combines the three dominant interactions (entropy, electrostatic, and interfacial deformation) present in jammed ionic colloidal emulsions. This model marks an improvement from prior models that have only incorporated a combination of two of the three dominant interactions at most. This combined model enables accurate comparison with mechanically measured G'_p over the range of glassy regime to jammed regime while using empirically determined ϕ, rather than *ad hoc* adjusted ϕ_{eff}. In Chapter 3, we present an improved analysis for DWS microrheology which allows accurate measurements of G'_p through the generalized Stokes-Einstein relation. The improved analysis furthermore opens up possibility for accurate quantitative investigation of high-frequency rheological properties of highly scattering colloidal systems, including jammed emulsion systems. Lastly, in Chapter 4, we perform DWS measurements on concentrated emulsions in the presence of depletion attractions. We compare these results to the repulsive emulsions near the jamming regime to investigate the role of depletion attractions in the linear mechanical properties of emulsions.

Chapter 2 - Entropic-Electrostatic-Interfacial Model for the Plateau Shear Elasticity and Osmotic Pressure of Disordered Jammed Monodisperse Emulsions

Reprinted by permission from Springer Nature: Springer *Rheologica Acta* "Entropic, Electrostatic, and Interfacial Regimes in Concentrated Disordered Ionic Emulsions", 55 (8), pages 683-697 by Kim, H.S., Scheffold, F., Mason, T. G. (2016).

2.1 - Introduction

Emulsions are one of the most important classes of soft materials. A first liquid is dispersed as droplets in a second immiscible liquid phase; the first liquid and second liquid are known as the dispersed phase (DP) as the continuous phase (CP), respectively. Typically, a surface-active agent, or surfactant, which is soluble in the CP but not in the DP, is added to inhibit coalescence of the droplets after they have been formed. Amphiphilic surfactants preferentially adsorb at the interfaces of the droplets, thereby providing repulsive forces that reduce or eliminate droplet recombination. Provided that the DP is highly insoluble in the CP, slow coarsening of the droplet size distribution via Ostwald ripening is negligible over practical measurement time scales ranging up to years[7], so such surfactant-stabilized emulsions can have droplet size distributions that are effectively time-independent. Many emulsions are stabilized using ionic surfactants, such as anionic SDS, which are highly soluble in an aqueous or polar CP but not significantly soluble in a non-aqueous or non-polar DP. For such ionic emulsions, short-range screened-charge repulsions between droplet interfaces, imparted by adsorbed amphiphilic ions, inhibit droplet coalescence, even when the droplets are concentrated through the application

of an osmotic pressure Π to high droplet volume fractions ϕ approaching and beyond the point at which droplets begin to deform as they interact with neighboring droplets.

For colloidal ionic emulsions, during the process of osmotic compression from a dilute gas-like dispersion of droplets, work is done against entropy, which is the origin of the osmotic pressure of Brownian droplets at low ϕ. As ϕ is increased further, work is done against electrostatic screened-charge repulsions and also against the interfacial tension σ of droplet interfaces populated with adsorbed ionic amphiphilic molecules. This interfacial tension sets the scale of the energetic cost of deforming droplets and creating additional interfacial area in the emulsion. Thus, there are three essential contributions to the free energy that are required to describe colloidal ionic emulsions: entropic, electrostatic, and interfacial. For emulsions having droplet radii larger than a few micrometers, the entropic term is typically negligible, and even the electrostatic term can often be neglected, if the Debye screening length λ_D is much smaller than the average droplet radius a. However, for colloidal emulsions, which have droplet radii ranging from several nanometers to several micrometers, accounting for all three terms is necessary when predicting their equilibrium properties, such as osmotic pressure Π and the linear plateau elastic shear modulus G'_p.

For uniform emulsions that have highly peaked monomodal size distributions, the positional structure of the droplets in the emulsion also plays an important role. When rapidly concentrated by applying a substantial osmotic pressure, for instance through ultracentrifugation, droplets in these monodisperse emulsions remain disordered even as the emulsion solidifies[33]. Thus, the colloidal disorder-order transition[62] is bypassed, and the droplets remain in a disordered structure as a consequence of quenching ϕ in the presence of Brownian excitations, which leads to a glassy ergodic-nonergodic transition[92] and then to jamming and isotropic

viscoelastic emulsions that have statistically reproducible macroscopic physical properties. The maximally probable jamming point[31, 82], a more precisely defined notion related to random close packing[60], for monodisperse spheres occurs at a critical volume fraction of $\phi_c \approx 0.646$. Going beyond earlier work of Princen[38], Mason[32-33, 35] measured $G'(\phi)$ of disordered microscale monodisperse emulsions stabilized by an ionic surfactant and previously established that this ϕ_c effectively set the beginning of the rise in measurements of $G'(\phi)$ after accounting for electrostatic repulsions between droplets in an *ad hoc* manner. Later rheological measurements by Wilking and Mason[46] on uniform repulsive ionic nanoemulsions showed that jamming can be seen at ϕ well below ϕ_c, thereby revealing the increasing importance of electrostatic repulsions for nanoemulsion systems as the droplet radius gets closer to the Debye screening length.

Although analytical models[32, 48, 69, 93] and numerical studies[35, 49, 70-72, 82, 94] have had some success in describing certain limited regimes of emulsion rheology, none have treated ionic colloidal emulsions by combining all three energetic contributions (*i.e.* entropic, electrostatic, and interfacial) into a total free energy that is minimized in a near-equilibrium approach to provide thermodynamic Π and G'_p. For uncharged colloidal emulsions, an energy minimization approach using a microscopic parameter describing average droplet deformation has been introduced by Mason[32, 49]; this model involved only entropic and interfacial terms. Exploring smaller colloidal emulsions, Wilking and Mason[46] measured $G'_p(\phi)$ of uniform disordered nanoemulsions and interpreted this data using a model based on two energetic contributions from repulsive electrostatic interactions and interfacial droplet deformation, linked by droplet jamming at ϕ_c. Through this interpretation, they deduced the electrostatic interaction potential as a function of average separation between droplet interfaces, essentially creating a macroscopic rheological form of a surface-forces measurement[95]. By keeping these same two energetic

contributions in an electrostatic-interfacial model that involved energy minimization, Scheffold *et al.* [49] took this idea further and predicted $G'_p(\phi)$ for disordered, ionic emulsions while neglecting entropy, which was assumed to be a constant value of several k_BT, where T is the temperature. Following on initial simulations[72], recent numerical work on the jamming transition of soft spheres has been carried out in the zero-temperature limit neglecting entropic contributions[79, 82, 96-98]. In this jamming work, where entropic excitations are absent, important scaling relations have been discovered, and these can be employed to derive measurable quantities such as the shear modulus or pressure based on the excess number of soft particle contacts and the pair interaction potential. However, none of these prior models of disordered uniform droplets, whether analytical or numerical, have combined all three relevant energetic terms in a near-equilibrium energy minimization approach.

Here, to overcome these limitations, we present a near-equilibrium free energy model for disordered colloidal ionic emulsions that includes all three terms and connects them using a model of nearest-neighboring droplet interactions that includes the disordered structure of jammed monodisperse droplets. This connection is made geometrically by introducing an average droplet deformation parameter, ϕ_d, as has been done previously in a two-term entropic-interfacial model[32, 49] for non-ionic emulsions. The three-term free energy is minimized with respect to ϕ_d for different droplet volume fractions ϕ relative to ϕ_c, yielding predictions of the emulsion's osmotic equation of state $\Pi(\phi)$. By further introducing a shear strain γ into this model, performing energy minimization, and then taking appropriate thermodynamic second derivative with respect to γ, we predict the plateau elastic shear modulus G'_p as a function of ϕ. We show that these predictions closely match measurements of Π and G'_p of model disordered colloidal ionic emulsions of silicone O/W taken at a fixed aqueous concentration of amphiphilic SDS

electrolyte. Moreover, we show that this model also explains measurements of $G'_p(\phi)$ of nanoemulsions in which a non-amphiphilic salt (sodium chloride, NaCl) has also been added. From this, we reveal that the surface potential on the droplets increases when the concentration of added NaCl begins to exceed that of the SDS. While distributions of microscopic properties, such as coordination number, are not taken into account explicitly, this entropic-electrostatic-interfacial (EEI) model, through a near-equilibrium energy minimization approach, reasonably predicts the shear modulus and osmotic pressure of Brownian, ionic, screened-charge, uniform, disordered, colloidal emulsions.

2.2 - Materials and Methods

2.2.1 - Nanoemulsion Preparation, Fractionation, and Characterization

We first create a polydisperse microscale O/W premix emulsion by emulsifying trimethyl-terminated polydimethylsiloxane (PDMS) silicone oil (viscosity 10 cSt, mass density 0.935 g/cm^3, Gelest) at ϕ = 0.3 into a 20 mM aqueous SDS solution (MP Biomedicals, Ultrapure)[6]. We process this premix emulsion at a liquid pressure of 10,000 psi through a 75 micron Y-type diamond interaction chamber using a Microfluidics M-110P homogenizer, recirculating for three passes using a cooling coil immersed in an ice-water bath. The resulting sub-microscale emulsion is fractionated via ultracentrifugation to reduce the polydispersity in the droplet size distribution. To size-fractionate the resulting polydisperse nanoemulsion, we dilute it to ϕ = 0.15 using a 10 mM SDS solution and ultracentrifuge at 15,000 rpm for 9 hours (L8-55 Beckman, SW 28 TI Rotor). We recover cylindrical elastic plugs at the top of the ultracentrifuge tubes and divide these into three disk-like sections (*i.e.* top, middle, and bottom sections) having equal lengths using a stainless steel blade. Similar sections of the plugs from different centrifuge tubes are combined to create three concentrated emulsions, yielding a first size-fractionation step.

We then separately dilute each of these three concentrated emulsions with 10 mM SDS solution to set $\phi = 0.15$, and we perform two additional ultracentrifugal size-fractionation steps (15,000 rpm for 6 hours, and 12,000 rpm for 8 hours). Repeated dilution of these concentrated emulsions with 10 mM SDS during size-fractionation ensures that the final SDS concentration in the CP is fixed to 10 mM, irrespective of the SDS concentration used to make the initial polydisperse emulsion. By taking the top sections of the first step, the middle sections of the second step, and the middle sections of the third step, we obtain a fractionated emulsion that has an average droplet radius that lies between larger sub-micron and micron-scale droplets[35] and smaller nanoscale emulsions[46] at [SDS] = 10 mM in prior published results. This concentration is only slightly higher than the critica micelle concentration of SDS near 8 mM, so energies associated with micellar-driven depletion attractions and between droplets are all much less than thermal energy and can be neglected for microscale and nanoscale droplet radii[62].

We measure the average hydrodynamic radius of this fractionated emulsion using dynamic light scattering (DLS) (90 deg, laser wavelength 633 nm, temperature 295 K, diluted using a 10 mM SDS solution to $\phi \sim 10^{-4} - 10^{-5}$), yielding an average hydrodynamic radius of a = 104 ± 2 nm. The polydispersity in the size distribution of these fractionated droplets is ≈ 20%, as inferred from small angle neutron scattering experiments on other emulsions that have been fractionated in a similar manner[47]. We also measure ϕ of the fractionated concentrated emulsion by evaporating the water from about 150 mg of emulsion at room temperature, since the oil and SDS are non-volatile[99]. To obtain smaller volumes of concentrated emulsion at desired ϕ, we dilute this stock fractionated concentrated emulsion with 10 mM aqueous SDS solutions and stir gently to avoid introducing air bubbles.

2.2.2 - Linear Shear Mechanical Rheometry

We load approximately 150 μL of the fractionated emulsion into a cone-and-plate shear rheometer (Rheometrics RFS II, controlled strain, 25 mm diameter, 0.1° cone angle, titanium). We perform a frequency sweep from 1.0×10^2 rad/s down to 1.0×10^{-2} rad/s at a peak shear strain amplitude of $\gamma = 1.0 \times 10^{-2}$ and then a strain sweep at a frequency of $\omega = 1.0$ rad/s from $\gamma = 2.0 \times 10^{-3}$ to $\gamma = 2.0$. The shear strain amplitude used in the frequency sweep is below the yield shear strain of all emulsion samples. We determine the plateau elastic shear moduli using the inflection point of the $G'(\omega)$ curve on the frequency sweep. If no inflection point can be identified on the $G'(\omega)$ curve, then G' at $\omega = 1.0$ rad/s is reported. We use an enclosing vapor trap filled with water to prevent water evaporation from the emulsion during the measurements. Residual torques arising from the vapor trap are much less than the torques due to the loaded emulsions for all measurements. We have tested for the possibility of wall slip, and it is not present for these fractionated nanoemulsions in the small shear strain limit.

2.2.3 - Interfacial Tension Measurements

We measure the interfacial tension between the aqueous 10 mM SDS solution, into which different concentrations of NaCl have been added, and the PDMS oil using a du Nouy ring[100-101]. Before each measurement, we clean the du Nouy ring (CSC Scientific, platinum-iridium, circumference = 5.996 cm; $R/r = 55.6$, where R is the radius of the ring and r is the radius of the platinum wire) by rinsing it with de-ionized water and flaming it with a methanol flame. We pour the aqueous solution, which has a higher mass density, into a small crystallization dish (80 mm diameter) and then slowly pipette the PDMS oil on top of the aqueous layer. The du Nouy ring is attached to a custom bottom-hole surface tensiometer and submerged through the PDMS oil into the aqueous phase. This tensiometer has been previously calibrated by measuring the air-

liquid surface tension of deionized water, obtaining the reported value to within ±5%. After waiting 5 minutes while the ring is fully submerged, we command the tensiometer to lower the crystallizing dish using a LabVIEW-controlled motor, and we digitally record the force on the ring by the bottom hook of the balance as the ring is slowly pulled through the interface at a rate of 0.10 mm/s until the interface detaches from the ring. We use the peak force and the mass densities to calculate the interfacial tension. All surface tension measurements have been performed at room temperature, T = 298 K, the same as has been used for the rheometry measurements.

2.3 – Entropic-Electrostatic-Interfacial (EEI) Model

We consider a disordered colloidal emulsion system of soft, deformable, uniform droplets composed of a first viscous liquid, the dispersed phase, that effectively form a Brownian suspension in a second immiscible liquid, the continuous phase, at a temperature T. Each droplet has a fixed volume, $V_{drop} = 4\pi a^3/3$, where a is its undeformed radius. The number of droplets in the system is N, the system's total volume is V, and the droplet volume fraction is $\phi = NV_{drop}/V$. Droplet stability is assured by adding an adequate concentration of an ionic amphiphilic surfactant, presumed to be present in only the continuous phase, some of which has adsorbed onto droplet interfaces. Thus, screened-charge electrostatic repulsions exist between the interfaces of droplets, and ions only reside in the continuous phase and at the surfaces of the droplets where the charged head groups of adsorbed ionic surfactant molecules are located. Droplet interfaces can deform near regions of closest approach (ROCAs) with nearest neighboring droplets. Such volume-preserving deformation of a droplet necessarily implies that work has been done against interfacial tension σ to increase its surface area. A characteristic Laplace pressure scale of an undeformed droplet is therefore σ/a, and an applied osmotic

pressure Π must approach this Laplace pressure scale to cause any significant droplet deformation.

In a dilute system of droplets at low ϕ, entropy dominates the free energy because the average separation h between neighboring droplets' interfaces at ROCAs, on average, is significantly larger than the characteristic thickness of the Debye layers, λ_D, of the screened-charge repulsion, represented schematically by blue boundaries around droplets as shown in Figure 2.1(a). At higher ϕ in the near-glass regime where ϕ is still below the ergodic-nonergodic glass transition, the droplets form cages around each other but the cages are transient due to entropic fluctuations; the system remains ergodic, exhibiting a low-frequency relaxation. As the system is further concentrated (Figure 2.1(b)), neighboring droplets no longer form transient cages, and the system becomes a non-ergodic glass; the low-frequency relaxation disappears, yet the droplets are not strictly jammed and Brownian fluctuations of droplets can still be significant. As ϕ is further increased, the separation between the droplets' interfaces becomes small enough that adjacent Debye layers of neighboring droplets begin to overlap, and the droplets begin to repulsively jam through screened-charge repulsions as shown by the electrostatic regime in Figure 2.1(c). This electrostatic repulsion also leads to tiny interfacial deformations near ROCAs of neighboring droplets in order to increase the separation between the charged droplet interfaces. Droplets experience greater electrostatic repulsion upon further concentration, so this leads to greater deformation of the droplets' surfaces to create facet-like areas of reduced curvature at ROCAs. At even larger Π, work is primarily done against interfacial tension and droplet deformation, and droplet deformation can become significant, as shown by the interfacial regime in Figure 2.1(d).

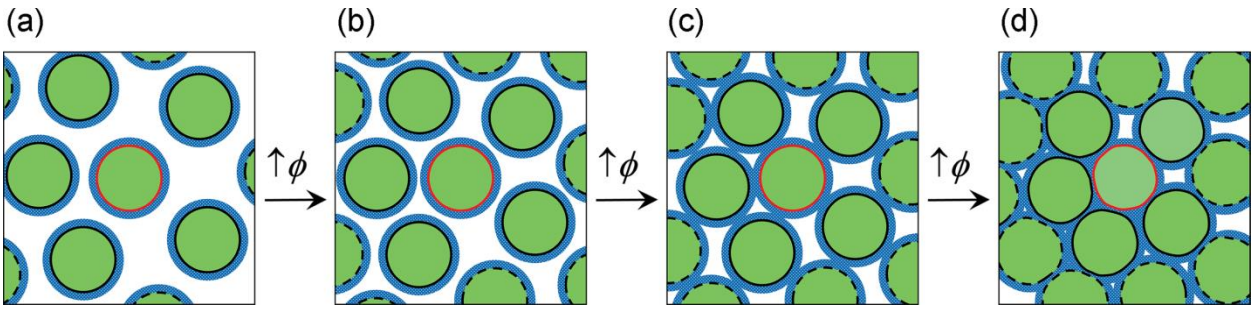

Figure 2.1. Rapidly concentrating uniform ionic O/W emulsions at high droplet volume fractions beyond glassy regime. Rapidly increasing the volume fraction ϕ of uniform colloidal droplets in ionic O/W emulsions leads to a disordered structure and a shear elasticity that arises from a combination of entropic, electrostatic, and interfacial forces. Dispersed-phase oil droplets (green) and surfaces populated with ionic surfactant molecules, which cause charge-screened repulsions between droplet interfaces. The aqueous continuous phase (white) contains ions, leading to a Debye screening length λ_D (blue coronas). A central droplet (red outline) is surrounded by its nearest neighbors (black outline), and these are surrounded by second nearest neighbors (dashed outline). Osmotic compression raises ϕ from the dilute limit into the following regimes: (a) the entropic near-glass regime, which is ergodic, so cages of nearest neighbors are transient, as a result of entropic fluctuations; (b) the entropic glass regime, which is non-ergodic; (c) the electrostatic jammed regime, in which Debye layers of the droplet begin to overlap significantly and screened electrostatic repulsive forces dominate as the droplets are jammed together; and (d) the interfacial jammed regime, in which droplets become increasingly deformed, but still weakly deformed, and work is predominantly done against interfacial tension.

As a fluid-like, dilute, Brownian dispersion of disordered droplets is concentrated by an applied Π, we assume that ϕ passes rapidly through the colloidal disorder-order transition[102-103], corresponding to $0.495 \leq \phi \leq 0.545$ for hard spheres, thereby suppressing crystallization, and into the near-glass regime, just below the glass transition volume fraction, corresponding to $\phi_g \approx 0.56$ - 0.58 for hard spheres, associated with an ergodic-nonergodic transition and the disappearance of a low-frequency relaxation. As ϕ is further raised through and beyond ϕ_g into the glass regime, and beyond that into the jamming regime, the system remains disordered. Thus, in a colloidal ionic emulsion system, as ϕ is raised, work is done against a combination of entropy, screened-charge electrostatic interfacial repulsions, and droplet interfacial tension and deformation. Consequently, we construct a model of the system's total free energy, which includes these three

contributions, and we calculate the osmotic pressure Π and the linear shear elastic plateau storage modulus G'_p, of this system by minimizing its total free energy in the limits of small droplet deformation and infinitesimal shear strains. As ϕ is raised, we assume that the most probable out of equilibrium states of disordered droplet configurations in the highly jammed system are effectively sampled by a near-equilibrium approach to the jammed regime through the glassy regime[48]. Inherent in this near-equilibrium approach is the implicit assumption that the particular disordered state of the colloidal emulsion at a given ϕ, even if only one manifestation of a large ensemble of microscopic droplet positional and interfacial structures that could arise from one trial to the next in preparing the emulsion, still gives rise to highly reproducible average macroscopic properties, including G'_p and Π. Thus, the dominant contribution to the free energy progresses from an entropic regime to an electrostatic regime, and then to an interfacial regime, in which more substantial droplet deformation can occur.

As a first step in building a suitable model for the free energy of a dense ionic emulsion, we consider a simpler disordered system of N uniform spheres having volume $V_{sphere} = 4\pi a^3/3$ in which the only contributions are entropic and all interactions between the spheres are purely hard. When ϕ is raised rapidly enough to avoid crystallization that could otherwise be caused by the entropic disorder-order transition, these disordered spheres can pass through the glass regime, characterized by a glass transition volume fraction $\phi_g \approx 0.56$ - 0.58[63, 68, 104], and jam in a disordered configuration at a critical volume fraction ϕ_c, where Π diverges. Randomly jammed or packed hard spheres are known to have $\phi_c = \phi_{MRJ} = \phi_{RCP} \approx 0.646$[31, 60]. For ϕ just below ϕ_c, the time- and ensemble-average free volume corresponding to accessible translational microstates of the center of mass of a sphere has been found to be proportional to the product of the volume per sphere with the cube of the volume fraction difference away from jamming[68]. This implies that

the number of translational microstates in the three-dimensional (3D) system is $\Omega \sim (\phi_c - \phi)^{3N}$ for $\phi < \phi_c$. Thus, according to Boltzmann's law, the 3D translational entropy of the hard-sphere system for ϕ near but below ϕ_c can be estimated as: $S_{HS} = k_B \ln \Omega \approx k_B \ln(\phi_c - \phi)^{3N} = 3Nk_B \ln(\phi_c - \phi)$. Thus, for a disordered system of hard spheres, it can be inferred that the entropic translational free energy scales as: $F_{ent,HS} = -TS_{HS} = -3Nk_BT \ln(\phi_c - \phi)$.

We next consider the entropic free energy of a system of disordered uniform colloidal particles that have hard interactions, yet are not completely spherical in a special manner that we describe as follows. Starting with spherical particles in a dense jammed system, we imagine slightly deforming all particles while conserving their internal volumes, in a manner that creates tiny facet-like areas, which locally have smaller curvature, near all ROCAs of all particles. The result of such selective tiny deformations causes the particles in the jammed system to lose contact with each other, and thus, unjam. Thus, this procedure of deformation at ROCAs increases the free volume available for translational motion of the particles. For irreversible deformations, the system of deformed particles, if further compressed, would jam at a slightly higher critical volume fraction ϕ_c' compared to ϕ_c of perfect spheres. The difference between ϕ_c' and ϕ_c can be connected to an effective deformation volume fraction ϕ_d related to translational motion: $\phi_d = \phi_c' - \phi_c$, where $\phi_d > 0$, but ϕ_d is still small, far from the limit of strong droplet deformation. Since the spherical particles have only been slightly deformed, the entropic contribution to the free energy of a disordered system scales in a similar manner as for spheres, but diverges at a higher ϕ_c' instead of ϕ_c: $F_{ent}/N \approx -3k_BT \ln(\phi_c' - \phi) \approx -3k_BT \ln(\phi_c + \phi_d - \phi)$. In the dense system, the slightly deformed particles cannot easily re-orient because of their neighbors, so we ignore rotational contributions to the entropic term in the free energy.

Next, we construct the interfacial free energy of deformable spheres based on a simplified model of droplet compression above the jamming point by its nearest neighbors for a certain applied osmotic pressure Π. We assume that the emulsion is an isotropic effective medium and therefore that there is an average near-equilibrium separation between centers of neighboring droplets as well as average local geometrical features at all ROCAs. For simplicity of representation in the schematic, we show a middle cross-section of a single cubic box (see Figure 2.2), implying six nearest neighboring droplets in 3D; the scaling form resulting from the following argument can also be generalized to a disordered configurational structure for the real emulsion system even if numerical prefactors differ. We define Δr to be an average deformation length along the centerline between adjacent droplets normal to a small circular facet; each facet has an area of πr_d^2, where r_d is the average radius of the facet (see Figure 2.2). We assume weak deformation near and above the jamming point, implying $\Delta r << a$. As a consequence, there is a gain in accessible translational microstates resulting from these deformations at ROCAs, which is directly related to ϕ_d[48]. For ϕ near the jamming point, each droplet in a disordered system of spheres also has ≈ 6 nearest neighboring droplets on average; we assume that changes in coordination number around the jamming point play only a minor role in the free energy near the jamming point. In going from an uncompressed to a weakly compressed state, the osmotic pressure effectively causes a small change in volume of an imaginary box around a droplet of $6(2a)^2\Delta r$. Dividing this change in volume by the box's original volume gives the deformation volume fraction $\phi_d = 24a^2\Delta r/(2a)^3 = 3\Delta r/a$, so ϕ_d is linearly proportional to Δr. Using the Pythagorean theorem, $a^2 = r_d^2 + (a - \Delta r)^2$, so the area of a deformed facet is $\pi r_d^2 \approx \pi a^2[1 - (1 - \Delta r/a)^2] \approx \pi a^2(2\Delta r/a) \approx 2\pi a\Delta r$ to leading order in Δr in the weak compression limit. The linear dependence of the facet area on Δr and therefore ϕ_d is a key geometrical result, but six times this

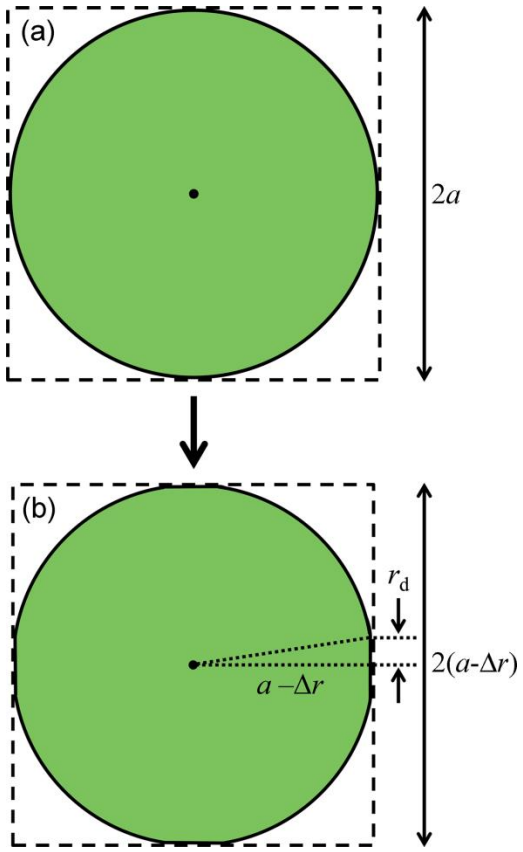

Figure 2.2. Schematic two-dimensional cross-section of a single oil droplet (green) in an aqueous surfactant solution (white) that is deformed by applying a uniform osmotic compression through a small reduction in the volume of an enclosing, rigid, semi-permeable cube (dashed lines). (a) Prior to deformation, the droplet is spherical and has radius a; the cube's edge length is $2a$. (b) After deformation, the enclosed droplet is isotropically compressed by a length $2\Delta r$ from the original cube. Small circular facets having radii r_d form at regions where the droplet interface is deformed. The droplet volume is conserved.

facet area does not represent the excess surface area of a droplet as a result of the osmotic compression, since volume conservation of the droplet must be respected.

To obtain the connection between the interfacial free energy and ϕ_d, we use force balance to obtain Π in terms of ϕ_d and then we integrate. By Newton's law, the force given by the weakly deformed droplet's Laplace pressure exerted over the area of one of its facets, on average, must be equal to the force given by the applied osmotic pressure over a face of the cube where that facet is located: $(2\sigma/a)(\pi r_d^2) \approx \Pi(2a)^2$. Thus, the osmotic pressure is linearly proportional to the

deformation volume fraction ϕ_d: $\Pi \approx (\pi\sigma/a^2)\Delta r \approx (\pi/3)(\sigma/a)\phi_d$. We define the interfacial free energy f_{int} associated with deformation of a single droplet to be a function of ϕ_d (*i.e.* the volume fraction above the jamming point of droplets with neighboring droplets: $\phi_d = \phi_c' - \phi_c$). We obtain f_{int} from Π using the differential equation[35] $\Pi(\phi) = [\phi^2/(4\pi a^3/3)]\partial f_{int}/\partial\phi$, which, when converted to be a function of ϕ_d, is approximately $\Pi(\phi_d) \approx [\phi_c'^2/(4\pi a^3/3)]\partial f_{int}/\partial\phi_d$, assuming that ϕ_d is significantly smaller than ϕ_c for weak droplet deformation. Using the force balance result $\Pi(\phi_d) \sim \phi_d$ and integrating, we obtain $f_{int} \sim \sigma a^2 \phi_d^2$, which is quadratic to leading order in ϕ_d, where $\phi_d \geq 0$. Thus, the change in a droplet's surface area resulting from a uniform osmotic compressional deformation is $\sim a^2\phi_d^2$ to leading order. Here, as a convenient convention, we omit a constant term related to the area of an undeformed droplet in f_{int}; this convention does not influence calculated values of Π and G'_p. In addition, for simplicity, we ignore small variations in the local coordination number that can occur around the jamming point, recognizing that this could be incorporated later into a more complex model.

In a real disordered material, the prefactor associated with f_{int} could be different than the one we have calculated from the cubic model, so we simply generalize the interfacial free energy per droplet to be: $f_{int} = F_{int}/N \cong 4\pi\xi\sigma a^2\phi_d^2$. We have introduced a dimensionless numerical parameter ξ to bridge between the cubic model and a real isotropic disordered emulsion system; ξ is related to the distribution of facet sizes and local neighbor configurations of the real emulsion system[48], and it could even depend on real polydispersity in the droplet size distribution. This simple model of energy associated with droplet deformation in a disordered concentration emulsion captures the most relevant main feature. We recognize that other refinements, such as the known logarithmic correction to the harmonic dependence of the free

energy[69], changes in local coordination number near and above ϕ_c[72], and changes in the effective values of ϕ_c for disordered systems of spheres having differing polydispersities[40], could be incorporated into more complex models in the future. Such adjustments would refine the main result of the simple deformation model for F_{int}/N near and just above the jamming point.

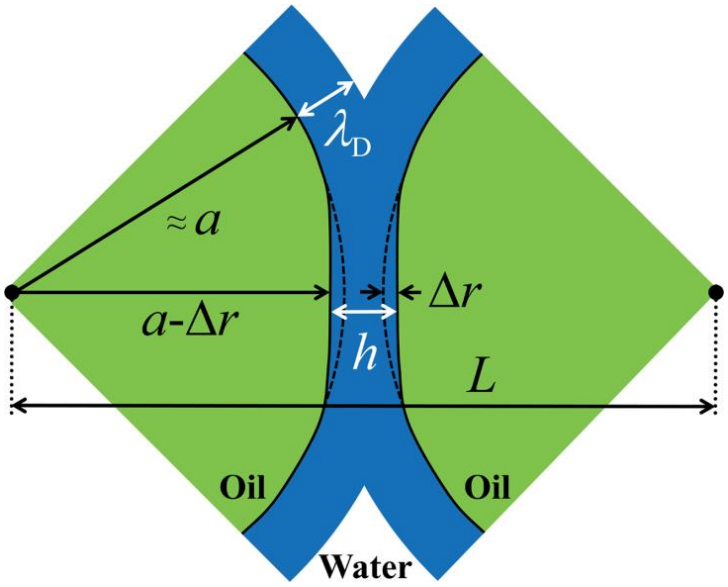

Figure 2.3. Schematic showing deformation of charged interfaces of two ionically stabilized droplets (green: oil) in a concentrated O/W emulsion at a region of closest approach (ROCA) for osmotic compressions approaching the Laplace pressure scale σ/a. The radius of an undeformed droplet is a and its interfacial tension is σ. Debye screened-charge layers having a screening length λ_D (blue) overlap significantly near the ROCA. The distance between the centers of the droplets is L, the length along the centerline of droplet deformation is Δr, and the separation between the oil-water interfaces at the ROCA is h. Ions (not shown) are present in the continuous aqueous phase, and charged amphiphiles (not shown) populate droplet surfaces.

Next, we consider the contribution to the free energy per droplet associated with electrostatic interactions, F_{elec}/N, via screened-charge electrostatic repulsions between the surfactant-coated interfaces of the deformed droplets. In the limit of weakly deformed droplets that have pairs of opposing deformed facets near all ROCAs, we assume that the dominant contribution to the electrostatic interactions arises primary from screened repulsions between these proximate facets, which are separated by an average distance of closest approach h as seen

in Figure 2.3. The high density of droplets having charged surface regions and counterion screening layers precludes the use of simple formulae developed for pair interactions of isolated spheres that have charged surfaces. The screened electrostatic potential between two disks (*i.e.* proximate deformed facets of neighboring droplets) separated by a distance h in a dilute solution having an ionic strength I is: $F_{elec}/N \approx 2\pi a \varepsilon_r \varepsilon_0 \psi_0 \exp(-h/\lambda_D)/h$, where the effective surface charge potential over all ROCAs is ψ_0, the Debye screening length is $\lambda_D = (\varepsilon_r \varepsilon_0 k_B T/(2e^2 I))^{1/2}$, ε_0 is the permittivity of vacuum, ε_r is the relative dielectric constant of the continuous phase, and e is the elementary charge[62, 105]. Here, ψ_0 is negative for anionic surfactants; for simplicity we report and plot only the magnitude of ψ_0. For common concentrations of ionic surfactants used to stabilize emulsions, λ_D is typically on the scale of few nanometers. This form for the free energy is identical to that used in a model that has successfully scaled nanodroplet elasticity[46], and it differs only slightly from a form used to model screened electrostatic interactions between isolated charged droplets that does not include the factor of $1/h$ [49]. Inherent in the expression for F_{elec}/N is the use of a linearized Poisson-Boltzmann model in the Debye-Hückel limit[62], so the surface potential on the droplets is fixed and the ionic strength is assumed to be relatively small. In the limit of small droplet deformation, changes in the total droplet surface area, which could influence the equilibrium adsorbed density and therefore the surface potential, are small and so we assume that ψ_0 does not depend on ϕ. Thus, the assumed electrostatic free energy contribution does not attempt to treat complex effects, including surfactant adsorption equilibria, high ionic strengths, and local variations in surfactant density on droplet interfaces near and in between ROCAs. These more complex effects related to electrostatic interactions could be potentially relevant for a subset of ionic emulsions; treatment of such effects lie beyond the scope of this simplified model.

To connect the electrostatic free energy with the rest of the EEI model, we must determine the dependence of h on the deformation volume fraction ϕ_d. We define the average center-to-center distance L between neighboring droplets to be: $L = h + 2(a - \Delta r) \approx h + 2a$ since the droplets are weakly deformable. At the shifted jamming point ϕ_c', we envision a deformed droplet enclosed by a larger, effective spherical shell having volume $V_{eff} = 4\pi(L/2)^3/3$. Our definition of the shifted volume fraction at the critical jamming volume fraction implies that $V\phi_c' = NV_{eff} = N[4\pi(L/2)^3/3]$. At the shifted jamming point, the true "bare" droplet volume fraction must still satisfy $V\phi = NV_{drop} = N(4\pi a^3/3)$. Since N and V are fixed, dividing these two equations implies that $\phi_c'/\phi = L/(2a)^3$, where $\phi_c' = \phi_c + \phi_d$. Solving for h in terms of ϕ, ϕ_d, and the universal jamming point ϕ_c, we find $h = 2a\,[(\phi_c'/\phi)^{1/3} - 1]$, leading to:

$$h = 2a\,(\phi_c + \phi_d)^{1/3}\,[\phi^{-1/3} - (\phi_c + \phi_d)^{-1/3}] \qquad (2.1).$$

For weak deformations around and near the jamming point, $\phi_d << \phi_c$ so ϕ_d will make only a minor modification to the $(\phi_c + \phi_d)^{1/3}$ factor present in the expression for h in equation (2.1), but it can still make a significant impact on the difference in brackets. Consequently, we further simplify the expression for h to:

$$h \approx 2a\,\phi_c^{1/3}\,[\phi^{-1/3} - (\phi_c + \phi_d)^{-1/3}] \qquad (2.2).$$

We modify this model of the near-equilibrium free energy of an ionic colloidal emulsion so that it can also be used to calculate the linear plateau elastic shear modulus G'_p, a rheological property based on an applied perturbative shear strain γ. The shear deformation changes the positional configurations of the droplets such that the shifted jamming point of the sheared system is lowered by a quadratic term proportional to γ^2, since the free energy cannot depend on the sign of γ, from the shifted jamming point of the unsheared system, ϕ_c'. Consequently, we

substitute $\phi_c' - \alpha\gamma^2 = \phi_c + \phi_d - \alpha\gamma^2$ into the above expressions for F_{ent}/N and F_{elec}/N (*i.e.* into h in equation (2.2)) wherever ϕ_c' occurs. Here, we have introduced α as a dimensionless parameter that describes the average shear effects to the configurations of the droplets, and effectively incorporates non-affine local displacements that can occur in such systems during osmotic compression and shear[72, 82]. Thus, the complete set of equations for the free energy per droplet contributions to the sheared emulsion system are:

$$F_{int} / N = 4\pi a^2 \xi \sigma \phi_d^{\,2} \tag{2.3}$$

$$F_{ent} / N = -3k_B T \ln\left(\phi_c + \phi_d - \phi - \alpha\gamma^2\right) \tag{2.4}$$

$$F_{elec} / N = 2\pi a^2 \psi_0^{\,2} \varepsilon_0 \varepsilon_r \exp\left(-h/\lambda_D\right)/h \tag{2.5},$$

where the separation at closest approach is

$$h = 2\phi_c^{1/3} a\left[\phi^{-1/3} - \left(\phi_c + \phi_d - \alpha\gamma^2\right)^{-1/3}\right] \tag{2.6}.$$

The total free energy per droplet is simply $F_{tot}/N = (F_{int} + F_{ent} + F_{elec})/N$, and ϕ_d is a parameter that must be minimized in order to satisfy the near-equilibrium condition of free energy minimization, consistent with the second law of thermodynamics.

To obtain Π in the absence of shear and G'_p for an applied perturbative shear, we first minimize the total free energy:

$$\left.\frac{\partial F_{tot}}{\partial \phi_d}\right|_{\phi_d = \phi_d^*} = 0\,, \tag{2.7}$$

from which we determine ϕ_d*, the deformation volume fraction satisfying the minimization condition, in terms of other parameters, including γ in the case when a shear has been applied. A transcendental equation arises from the minimization condition, so *FindRoot* function in

Mathematica (Wolfram Research Inc.) is used to solve numerically for the one positive real root of ϕ_d* that corresponds to a meaningful physical value. Once we have obtained this ϕ_d*, we substitute it back into the expression for the total free energy wherever ϕ_d occurs to obtain the minimized total free energy F_{tot}*. We then take appropriate thermodynamic derivatives of F_{tot}* to determine Π and G'_p[48]:

$$\Pi = \left[\phi^2 / \left(NV_{drop}\right)\right]\left[\partial F_{tot} / \partial \phi\right]_{\phi_d = \phi_d^*, \gamma = 0} \tag{2.8}$$

$$G'_p = \left[\phi / \left(NV_{drop}\right)\right]\left[\partial^2 F_{tot} / \partial \gamma^2\right]_{\phi_d = \phi_d^*, \gamma = 0} \tag{2.9}.$$

To obtain the osmotic pressure Π, solutions of ϕ_d* are found for a range of ϕ values at $\gamma = 0$, such that the local slope of F_{tot}* with respect to ϕ can be calculated and used in equation (2.8). The plateau elastic shear modulus G'_p is found numerically as follows. For a particular ϕ value, solutions of ϕ_d* are found over a small range of γ values from 0 to about 0.01, below the measured yield strain of concentrated disordered emulsions, corresponding to the linear rheological regime. At each ϕ, the curvature $\partial^2 F_{tot}$*/$\partial \gamma^2$ is obtained by finding the least-squares fit of parabolic F_{tot}*(γ) centered around $\gamma = 0$ for small γ. The parabolic coefficient from the fit is then used to determine G'_p. This process is repeated for different ϕ, yielding G'_p as a function of ϕ. We have verified this approach using a high density of ϕ and γ values (*i.e.* $\Delta\phi = 0.009$ and $\Delta\gamma = 0.0005$ intervals), and we find excellent agreement with a prior analytical solution[48] when electrostatic forces have been eliminated (*i.e.* when $\psi_0 = 0$ V). By first solving the transcendental equation for ϕ_d* to determine the minimized F_{tot}* and then finding slopes and curvatures of F_{tot}* numerically, we obtain the thermodynamic properties Π and G'_p for a system of uniform deformable ionic droplets as a function of ϕ below, through, and above the jamming point.

However, the EEI model is not expected to be appropriate in limits as $\phi \rightarrow 1$, away from the weak deformation limit where ϕ_d^* would become large, and as $\phi \rightarrow 0$, where the scaling form used for the entropic term for ϕ near ϕ_c would be inappropriate.

2.4 - Results and Discussion

2.4.1 – EEI Model Comparison to Mechanically Measured G'_p

We compare the predictions of the EEI free energy minimization model with five sets of $G'_p(\phi)$ measured for uniform, disordered, ionic, O/W emulsions having microscale, sub-microscale, and nanoscale droplet radii, as shown in Figure 2.4. We fix T = 298 K, since measurements have been made at room temperature, and we also fix ϕ_c = 0.646, based on the known ideal limit of maximal random jamming of perfectly monodisperse spheres, recognizing that residual polydispersity in a real emulsion could shift this value somewhat[40, 75]. We use a Debye screening length of $\lambda_D \approx 3.4$ nm, predicted from $\lambda_D = [\varepsilon_r \varepsilon_0 k_B T/(2e^2 I)]^{1/2}$, where the ionic strength I of the SDS solution is $I \approx 8.2$ mM, corresponding to the known critical micelle concentration (CMC) of SDS. This value of λ_D is only about 10% larger than the calculated Debye length using I = 10 mM, disregarding micelle formation and the CMC. Because the diameter of SDS micelles (*i.e.* ≈ 4 nm) is larger than the Debye length and the SDS concentration is very close to its CMC, any small residual concentration of SDS micelles would not be expected to contribute significantly to the screening length. We fix the surface tension to be σ = 9.8 mN/m based on a prior measured value for PDMS oil and 10 mM SDS solution.

We determine the remaining parameters by optimizing the global fit of the EEI model to all sets of measurements in Figure 2.4, yielding ξ = 0.15, α = 0.85, and $|\psi_0|$ = 270 mV. These values lie within uncertainty limits of separate entropic-interfacial and electrostatic-interfacial

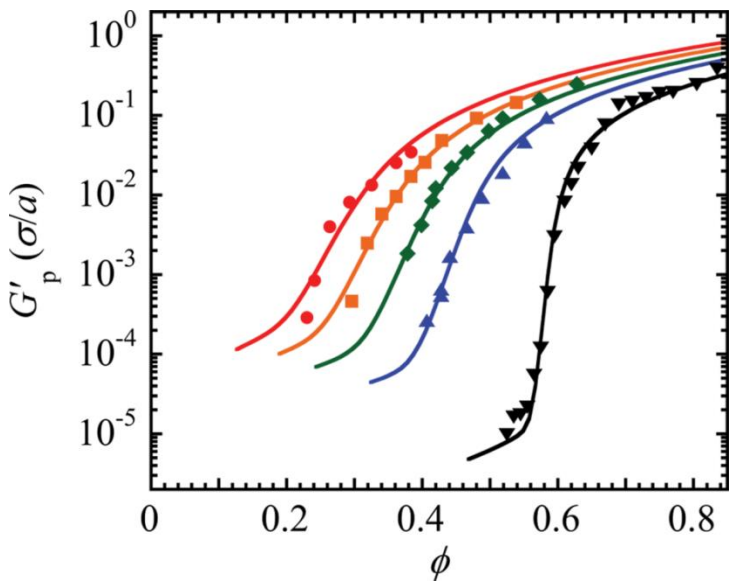

Figure 2.4. Plateau elastic shear moduli G'_p, in units of Laplace pressure scale σ/a, as a function of droplet volume fraction ϕ for uniform microscale and nanoscale 10 cSt trimethyl terminated PDMS O/W emulsions stabilized by a 10 mM SDS solution. Points represent measurements by mechanical shear rheometry and solid lines are obtained via calculation using equation (2.9). Droplet radii are (from left to right) a (nm): 28 (33) [red circles], 47 (47) [orange squares], 73 (67) [green diamonds], 104 (108) [blue up-triangles], and 530 (530) [black down-triangles] at $T = 298$ K. Values for a listed in parenthesis are used in the calculation. Data for $a < 100$ nm are from, for $a = 530$ nm are from, and for $a = 104$ nm are from the herein work. We fix the jamming point to be $\phi_c = 0.646$ and temperature $T = 298$ K. We also fix $\sigma = 9.8$ mN m^{-1}. Calculation parameters (see text) that yield the best overall fits to all data are: $\xi = 0.15$, $\alpha = 0.85$, $\lambda_D = 3.4$ nm, and $\psi_0 = 270$ mV.

models[48-49], where we have made minor modifications to measured droplet hydrodynamic radii within the range of polydispersity (*i.e.* ≈ ±15%) to improve the global agreement. The value of ψ_0 obtained from the global fit is reasonably close to an estimated value of $|\psi_0| \approx 210$ mV using Grahame's equation $\psi_0 = [(2k_BT)/(ze)]\sinh^{-1}[\sigma_e/(8c_o\varepsilon_r\varepsilon_o RT)^{1/2}]$, which is based on Gouy-Chapman theory[62], where c_0 is the bulk molar concentration of the counterions in the CP, $z = 1$ is appropriate for monovalent ions arising from dissociated SDS. In this calculation we have used a measured and reported value of $\sigma_e \approx 2$ e/nm^2 for the adsorbed surface density of dodecyl sulfate anions (DS^-) at the interface of decane and water at c_0 = [SDS] = 10 mM [106]. Differences in the dispersed phase compositions and differences in the experimental system from the assumed

boundary conditions inherent in Grahame's equation could account for at least some of the difference between the estimated and fitted values of ψ_0. Overall, the EEI model matches the measurements over a wide range of radii from nanoscale to microscale emulsions. It captures features including the interfacial contributions to G'_p at high ϕ as well as electrostatic and entropic contributions at lower ϕ. Variations in residual droplet polydispersity, which for the measured emulsions is typically is about 10 - 20%, between different $G'_p(\phi)$ could account for at least some part of small deviations of the data from the model. At the lowest ϕ shown, the reported G'_p values do not necessarily correspond to a zero-frequency G', so the frequency dependence of the storage modulus could play a role in any departures of the EEI model from the data there.

2.4.2 – EEI Model Comparison to Osmotic Pressure Measurements

The same parameters can be used with the EEI model to describe the measured osmotic equation of state $\Pi(\phi)$ of a uniform disordered microscale O/W PDMS emulsion having a = 480 nm and stabilized using 10 mM SDS, as shown in Figure 2.5 [32, 35, 48]. Given the large scatter in the data for Π at lower ϕ, and the higher difficulty in measuring precise values of Π using an ultracentrifugation technique[35], the comparison of measured and calculated $\Pi(\phi)$ using parameters that had been optimized only using $G'_p(\phi)$ data represents good agreement. If the five sets of $G'_p(\phi)$ are disregarded, even better agreement with the measured $\Pi(\phi)$ could be obtained using a slightly higher value of ξ = 0.22 in the model. Because ϕ_c = 0.646 is used in our current calculations, rather than an effective jamming volume fraction of $\phi_{c,eff} \approx 0.62$ in prior work[48], in which electrostatic effects had only been accounted for in an *ad hoc* manner, the EEI model represents an improvement over prior analyses and is consistent with existing data describing the

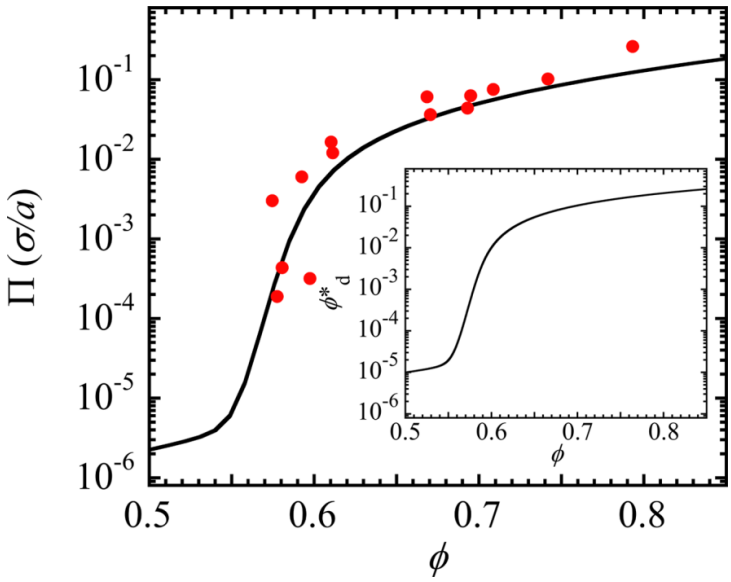

Figure 2.5. Osmotic pressure Π in units of Laplace pressure scale σ/a, for SDS-stabilized PDMS O/W emulsions having average radius a = 480 nm. Points represent measurements by centrifugation and solid lines are obtained via calculation using equation (2.8) using same parameter values as for G'_p in Figure 2.4. The calculated deformation volume fraction, ϕ_d^*, as a function of volume fraction ϕ for a = 480 nm is shown in the inset. The osmotic pressure data are from Mason *et al*[32, 35].

osmotic equation of state of disordered uniform emulsions. Furthermore, the largest values of ϕ_d^* (see Figure 2.5 inset) shows the relative change in surface area per droplet in any of our calculations, $\xi\phi_d{}^{*2}$, is at most few percent; thus, the droplets are only weakly deformed over the intermediate range of ϕ where we compare the EEI model with measurements.

2.4.3 – EEI Model G'_p Comparison to Nanoemulsions with Added NaCl

Adding a solution of a non-amphiphilic salt, such as NaCl, to the aqueous continuous phase can be used to effectively melt and liquify elastic ionic nanoemulsions over a certain range of ϕ[46, 49]. The measured $G'_p(\phi)$ of monodisperse emulsions having a = 47 nm at [SDS] = 10 mM for several different added [NaCl] are shown in Figure 2.6. At larger [NaCl] the onset of elasticity, corresponding to the rise in G'_p, occurs at larger ϕ. To explain the origin of this effect, we consider the influence of [NaCl] on several parameters in the EEI model, as follows.

The interfacial tension between an oil and an aqueous surfactant solution is typically reduced when soluble salts are added to the aqueous solution[107]. We have measured the interfacial tension σ between the oil and an aqueous solution containing fixed [SDS] = 10 mM while varying [NaCl] added. The results are plotted relative to σ_0 between PDMS oil and a 10 mM SDS aqueous solution in Figure 2.7(a) (squares). The measured reduction in σ/σ_0 can be fit using a semi-empirical function, $\sigma/\sigma_0 = 1 + A(\exp(-[\text{NaCl}]/[\text{NaCl}]^*) - 1)$, yielding $A = 0.338 \pm 0.007$ and $[\text{NaCl}]^* = 28 \pm 2$ mM with a correlation coefficient of $R^2 = 0.998$. This reduction in interfacial tension by the added non-amphiphilic electrolyte indicates that DS^- have been driven from the continuous phase onto the interfaces of the oil droplets.

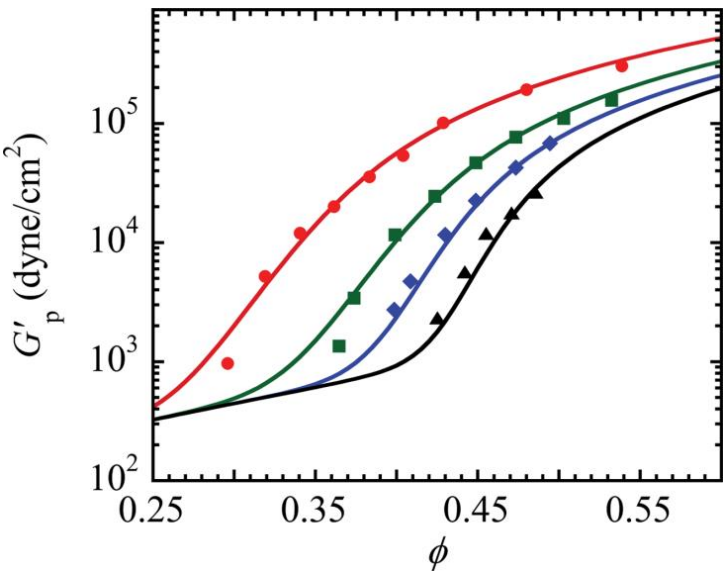

Figure 2.6. Plateau elastic shear moduli G'_p as a function of droplet volume fraction ϕ for a = 47 (46) nm, 10 cSt PDMS O/W emulsions stabilized by 10 mM SDS with varying NaCl concentrations at T = 298 K. Points represent measurements by mechanical shear rheometry and solid lines are obtained via calculation using equation (2.9). The concentrations of added NaCl (mM) (from left to right) are: 0 (red circles), 10 (green squares), 40 (blue diamonds), and 90 (black triangles). Surface tension and electrostatic parameters used to calculate the corresponding lines are shown in Figure 2.7; all others are the same as in Figure 2.4. Data from Wilking *et al*[46].

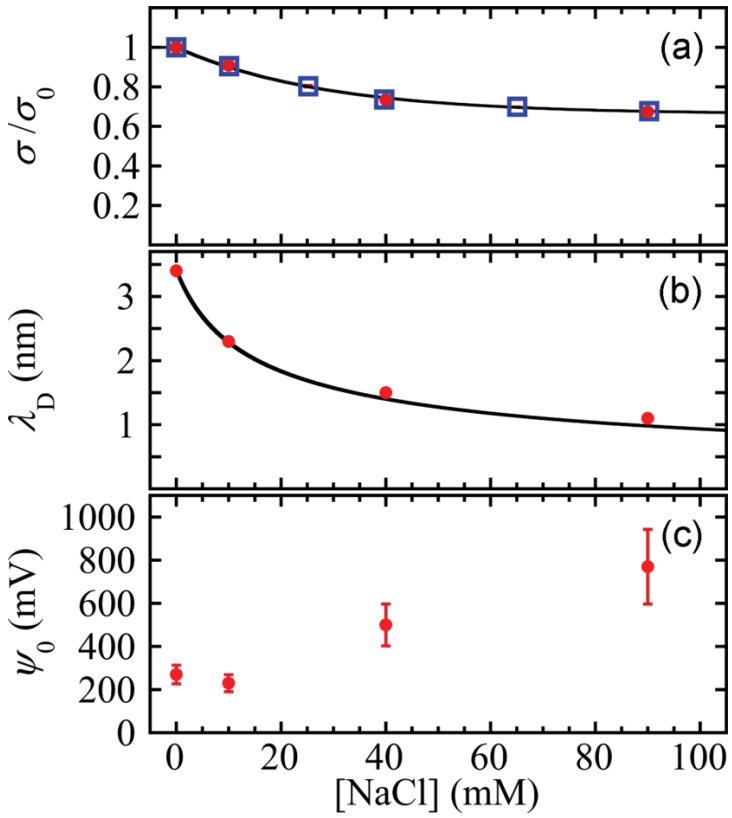

Figure 2.7. Parameter values used to fit $G'_p(\phi)$ data of emulsions to which salt NaCl has been added in Figure 2.6, for uniform, concentrated, disordered PDMS emulsions in aqueous 10 mM SDS solution. (a) Experimental measurements of interfacial tension, measured using a du Nouy ring method, are plotted as relative surface tension σ/σ_0, referenced to the interfacial tension of σ_0 = 9.8 mN m^{-1}, between 10 mM SDS and PDMS oil are shown as blue squares. An empirical exponential model (black line) for the relative interfacial tension is shown (see text). Red points on the fitted line are used for the calculations. (b) Debye lengths, λ_D, used in the fits (red points) follow the predicted Debye length in an electrolyte: $\lambda_D = (\varepsilon_r\varepsilon_0 k_B T/(2e^2 I))^{1/2}$ (black line). (c) Surface potential, ψ_0 values that give the best fits reveal that ψ_0 increases with [NaCl] once [NaCl] approaches and exceeds the fixed [SDS] ≈ 10 mM. Reported uncertainties in ψ_0 (error bars correspond to one standard deviation) have been determined using minimization of chi-square values of the fits to $G'_p(\phi)$.

The increased ionic strength in the aqueous phase also affects the electrostatic interactions between the droplets by reducing $\lambda_D = [\varepsilon_r\varepsilon_0 k_B T/(2e^2 I)]^{1/2}$, where this formula is valid only in the limit of dilute electrolyte concentrations[49, 62]. Values of λ_D for added [NaCl] = 0, 10, 40, and 90 mM used in the model are 3.4, 2.3, 1.5, and 1.1 nm, respectively (see Figure 2.7(b)). These values of λ_D yield good agreement with the measured $G'_p(\phi)$ and deviate only slightly

from the Debye screening equation at higher [NaCl]. Because the activities of ionic species can deviate from the ideal dilute Debye limit, slight departures of λ_D from the ideal prediction at higher [NaCl] could be anticipated.

Using the measured reduction in σ/σ_0 and the predicted reduction in λ_D with [NaCl], we adjust ψ_0 to obtain the best overall agreement for each $G'_p(\phi)$ curve in Figure 2.6; the results for ψ_0([NaCl]) are shown in Figure 2.7(c). For [NaCl] ≤ 10 mM, which is comparable to or smaller than [SDS], ψ_0 does not change much within the uncertainties obtained from the fits. However, for [NaCl] ≥ 40 mM, there is a marked increase in ψ_0, indicating a greater surface charge. At least some of this increase in ψ_0([NaCl]) is likely to arise from additional adsorbed DS^- on the surfaces of droplets, caused by the higher concentration of additional non-amphiphilic anions in the continuous phase. This increased adsorption is qualitatively consistent with the reduction in surface tension related additional DS^- on the droplet surfaces, a consequence of a shift in the DS^- adsorption equilibrium caused by the addition of NaCl to the continuous phase. However, considering the mass balance of free and adsorbed surfactant, we find that increased adsorption of DS^- from the CP onto the surfaces of the droplets cannot be solely responsible for the increase in the value of ψ_0. This suggests that non-ideal ionic effects, such as the development of a secondary attractive minimum in the droplet pair potential at high added non-amphiphilic salt concentrations is likely to also be happening[32, 87]. Such secondary minima are not captured by the electrostatic term in our model, so a more complex model is most likely needed to describe the regime of high concentrations of added non-amphiphilic salts. Overall, the calculated values of $G'_p(\phi)$ agree well with the measured data using the parameters shown in Figure 2.7. Thus, we have used the EEI model in combination with the existing macroscopic measurements for $G'_p(\phi,$[NaCl]) to estimate the microscopic ψ_0([NaCl]).

2.4.4 – EEI Model Predictions of Linear Rheological Behavior

Having determined appropriate parameters for the EEI model, which yield good agreement with a large number of measurements of $G'_p(\phi)$ over a wide range of droplet radii and added [NaCl], we vary certain parameters while fixing others in order to predict the linear rheological behavior of disordered ionic emulsion systems over a wide range of conditions. Figure 2.8 shows the systematic variation of predicted $G'_p(\phi)$ for various radii, fixing other parameters to match with PDMS O/W emulsions stabilized at [SDS] = 10 mM. The smaller the droplet radii are, the more likely the crossover behavior occurs towards lower ϕ, below the maximally random jamming point ϕ_c = 0.646, as a consequence of the screened-charge electrostatic repulsion. As the characteristic droplet radius becomes closer to λ_D, the droplets effectively jam at much lower volume fractions. The EEI model appropriately captures this jamming effect as well as the entropic modulus scale for ϕ below the effective jamming point.

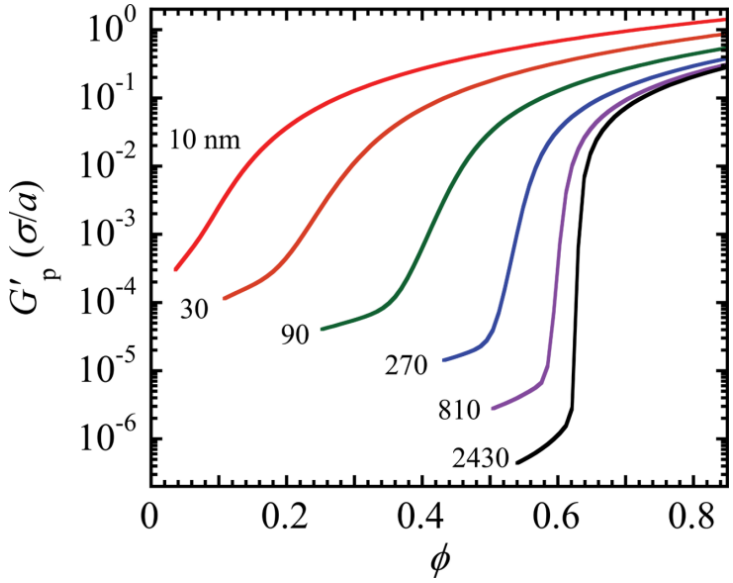

Figure 2.8. Calculated plateau elastic shear moduli G'_p, in units of Laplace pressure scale σ/a, as a function of droplet volume fraction ϕ, based on the EEI model describing colloidal ionic emulsions for various droplet radii a in a 10 mM aqueous SDS solution. For model parameters, see Figure 2.4 caption.

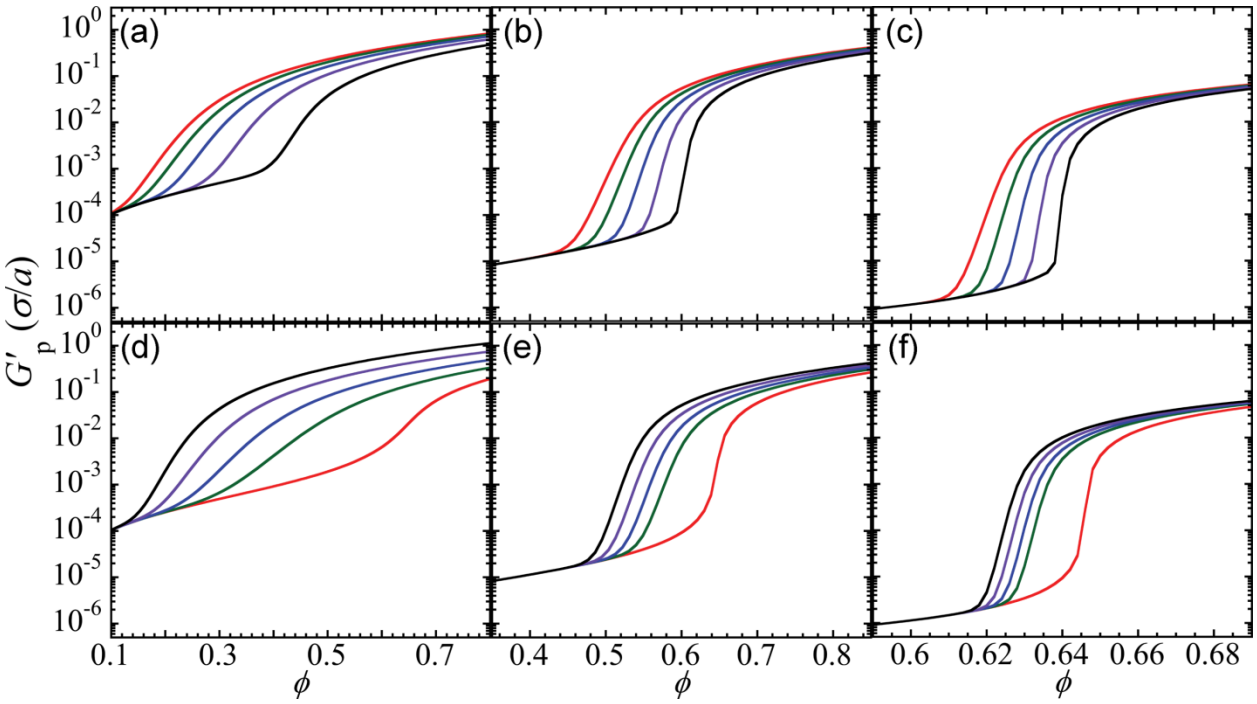

Figure 2.9. Calculated dependence of plateau elastic shear modulus G'_p as function of droplet volume fraction ϕ on electrostatic parameters for O/W emulsions in aqueous 10 mM SDS solution. Droplet radii a (nm) are: (a,d) 30, (b,e) 270, and (c,f) 2430. For (a,b,c) the Debye length is varied, λ_D (nm): 5, 4, 3, 2, and 1 (lines from left to right) at a fixed surface potential ψ_0 = 270 mV. For (d,e,f) the surface potential is varied ψ_0 (mV) = 810, 270, 90, 30, and 0 (lines from left to right) at fixed λ_D = 3.4 nm. All other parameters are fixed and the same as those in Figure 2.4.

In Figure 2.9, we show how G'_p is influenced by different values for electrostatic parameters λ_D and ψ_0. For nano- and micro-scale emulsions (a = 30 nm, 270 nm, and 2430 nm), at a given droplet size and fixed surface potential, the rapid rise in G'_p associated with disordered jamming shifts towards lower ϕ as λ_D is increased, as shown in Figures 2.9(a) - 2.9(c). The limit $\lambda_D \rightarrow 0$ effectively turns off the electrostatic term in the free energy, so $G'_p(\phi)$ in that limit reflects only entropic and interfacial contributions. Increasing the surface potential while fixing λ_D for the same set of ionic emulsions causes this rapid rise to shift towards lower ϕ, as shown in Figures 2.9(d) - 2.9(f). Setting ψ_0 = 0 mV also corresponds to an absence of electrostatic effects, so interactions between neighboring surfaces of deformable droplets are effectively hard.

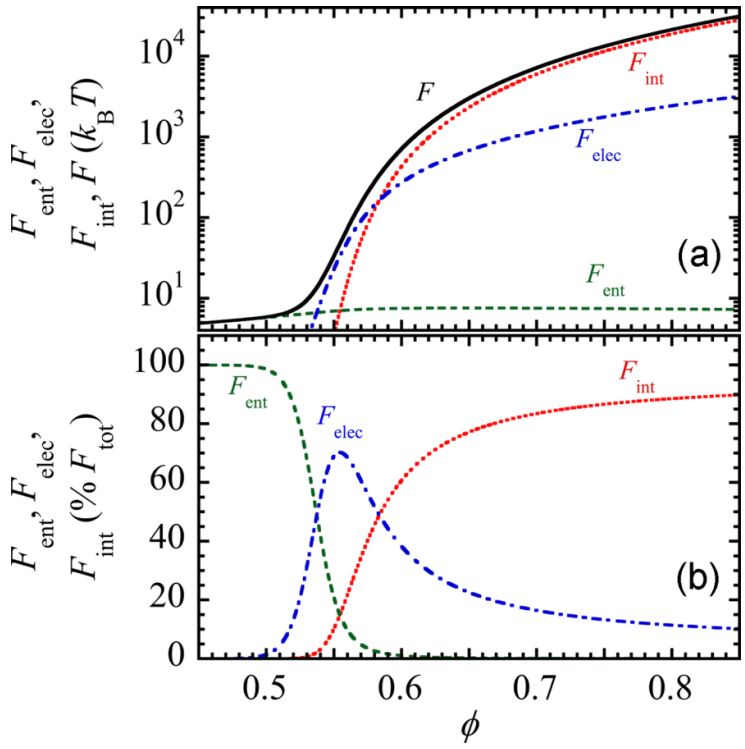

Figure 2.10. Calculated free energies per droplet F as function of droplet volume fraction ϕ for uniform disordered emulsions having a = 270 nm oil droplets in 10 mM aqueous SDS solution. Same parameters as from Figure 2.4 are used. (a) entropic (F_{ent}, dashed line), electrostatic (F_{elec}, dashed-dotted line), interfacial (F_{int}; dotted line), and total $F = F_{ent} + F_{elec} + F_{int}$ (black solid line). (b) Percent relative contributions of F_{ent}, F_{elec}, and F_{int} to the total F.

We next calculate the relative contributions of entropic, electrostatic, and interfacial terms to F_{tot}, G'_p, and Π using the EEI model. Figures 2.10 - 2.12 show the absolute and relative contributions for PDMS emulsions having a = 270 nm at [SDS] = 10 mM over a range of ϕ. The relative percent graphs, shown in Figures 2.10(b) - 2.12(b), obtained from free energy minimization, are consistent with the qualitative regimes depicted in Figure 2.1. Furthermore, Figure 2.10(a) shows that the entropic free energy per droplet remains about ≈ 5 k_BT above the crossover to the electrostatic regime. This value resulting from free energy minimization of the EEI model is close to an assumed value in the electrostatic-interfacial energy model[49].

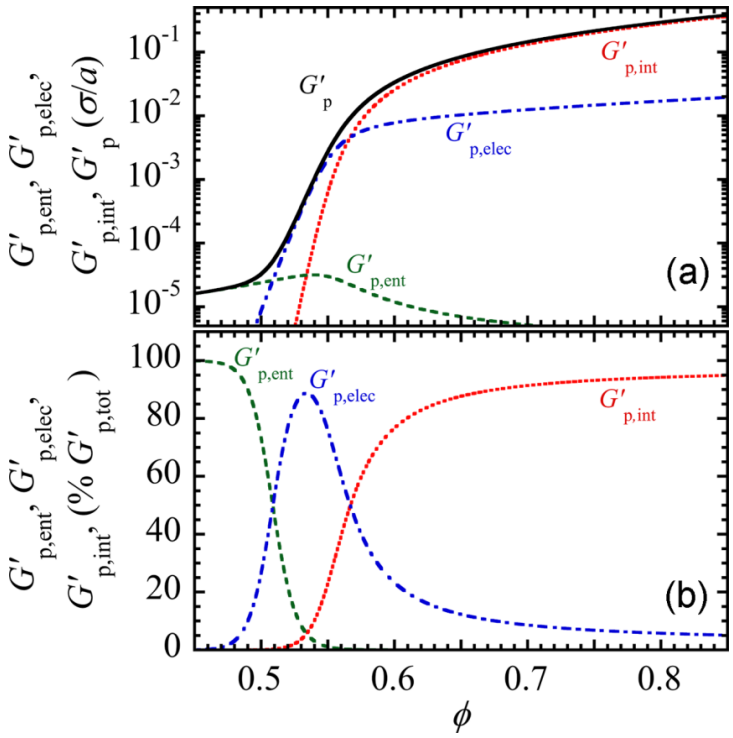

Figure 2.11. Calculated plateau elastic shear moduli G'_p for a = 270 nm oil droplets in 10 mM aqueous SDS solution as a function of droplet volume fraction ϕ. Same parameters as used in Figure 2.4. (a) Entropic ($G'_{p,ent}$, dashed line); electrostatic ($G'_{p,elec}$, dash-dot line); and interfacial ($G'_{p,int}$, dotted line); total ($G'_p = G'_{p,ent} + G'_{p,elec} + G'_{p,int}$, solid black line). (b) Percent relative contributions of $G'_{p,ent}$, $G'_{p,elec}$, and $G'_{p,int}$ to the total G'_p.

Using parameter values that correspond to PDMS droplets in 10 mM aqueous SDS solutions, we determine the two values of ϕ corresponding to crossover in G'_p between the entropic and electrostatic regimes and between the electrostatic and interfacial regime for a given droplet radius. We repeat this process for a wide range of droplet radii and show the results as lines separating the dominant contributions to G'_p in Figure 2.13. The labeled areas in the plots indicate which of the three terms contribute the most to G'_p. The two lines in Figure 2.13 converge to the critical jamming point ϕ_c in the limit of very large, macroscopic droplets, and the electrostatic regime effectively disappears.

The dependence of G'_p on temperature has also been explored. Temperature mostly affects the magnitude of the entropic term, although temperature also affects λ_D in the

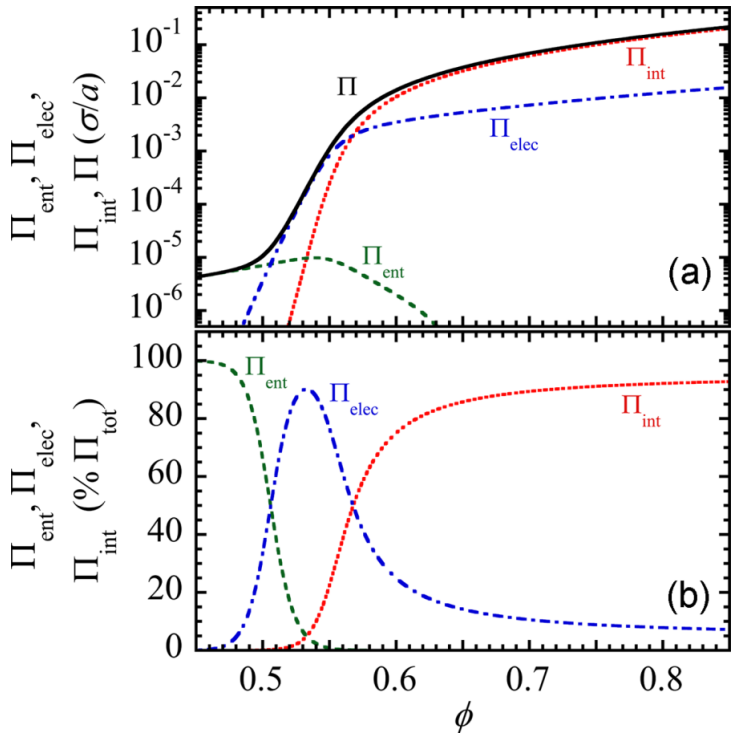

Figure 2.12. Calculated contributions to the osmotic pressure Π for *a* = 270 nm oil droplets in 10 mM aqueous SDS solution as a function of droplet volume fraction ϕ. Same parameters as used in Figire 2.4. (a) Entropic (Π_{ent}, dashed line); electrostatic (Π_{elec}, dash-dot line); and interfacial (Π_{int}, dotted line); total ($\Pi = \Pi_{ent} + \Pi_{elec} + \Pi_{int}$, solid black line). (b) Percent relative contributions of Π_{ent}, Π_{elec}, and Π_{int} to the total osmotic pressure.

electrostatic term. In the entropic regime, the calculated G'_p from the numerical minimization procedure is found to increase linearly with respect to increasing temperature, consistent with $G'_p \sim k_B T/V_f$[62, 68]. In principle, if the temperature T could be tuned to approach 0 K while preserving the CP in a liquid state, then the entropic contribution to the free energy would be effectively turned off, and the two-term electrostatic interfacial free energy would lead to the jamming result[46, 49]. Given the narrow range of temperatures over which the aqueous phase exists in a liquid state (*e.g.* from about 273 K to 373 K), varying temperature over this range only makes a minor change in the osmotic equation of state and in the linear viscoelastic modulus. Thus, for O/W emulsions, the most effective means of investigating the entropic regime is not by varying temperature, but rather by reducing the droplet radius and also the Debye screening length.

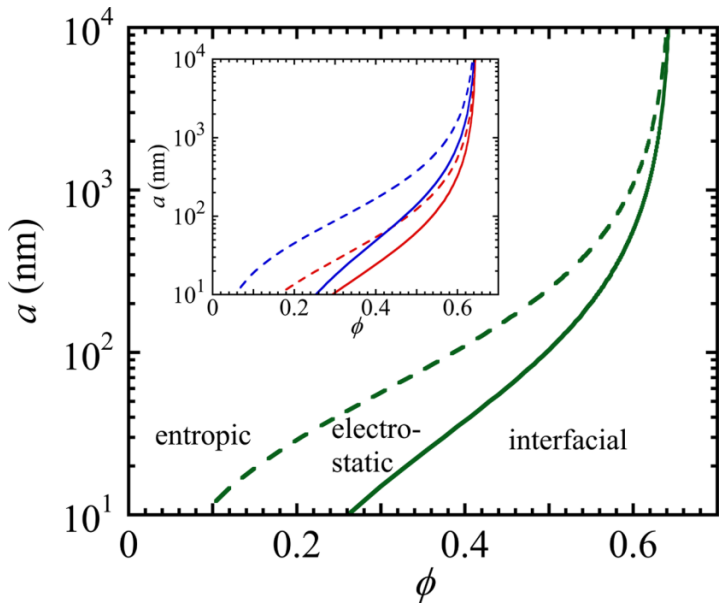

Figure 2.13. Calculated regimes of dominant contributions by entropic, electrostatic, or interfacial terms to the plateau elastic shear moduli G'_p for 10 cSt PDMS oil droplets stabilized by 10 mM SDS for varying radii a and droplet volume fraction ϕ at a Debye screening length of λ_D = 3.4 nm (green lines). Other parameter values are the same as in Figure 2.4. The dotted line represents equal relative contributions of entropic and electrostatic terms; the dashed line represents equal relative contributions of the electrostatic and interfacial terms. Inset: lowering λ_D to 1.8 nm (red lines) reduces the electrostatic and interfacial zones; whereas raising λ_D to 5.0 nm (blue lines) expands the electrostatic and interfacial zones (all other parameters are fixed).

2.4.5 – Initial EEI Model Comparison to DWS Microrheology

This section is adapted with permission (Creative Commons License 4.0) from the following journal article: Braibanti, M., **Kim, H. S.**, Senbil, N., Pagenkopp, M. J., Mason, T.G., Scheffold, F. "The Liquid-glass-jamming Transition in Disordered Ionic Nanoemulsions". *Sci. Rep.*, **7**, 13879 (2017).

The EEI model is also used to compare against DWS measurements of nanoemulsion's plateau elastic shear moduli G'_p at T = 295 K (*i.e.* 22°C). The G'_p of PDMS O/W nanoemulsions, having a = 130 nm and stabilized by 10 mM SDS containing varying concentrations of NaCl, are calculated by relating the DWS-measured plateau mean square displacement $\langle \Delta r^2 \rangle_p$ to the long-time limit of the generalized Stokes-Einstein relation: $G'_p = k_B T/(\pi a \langle \Delta r^2 \rangle_p)$.

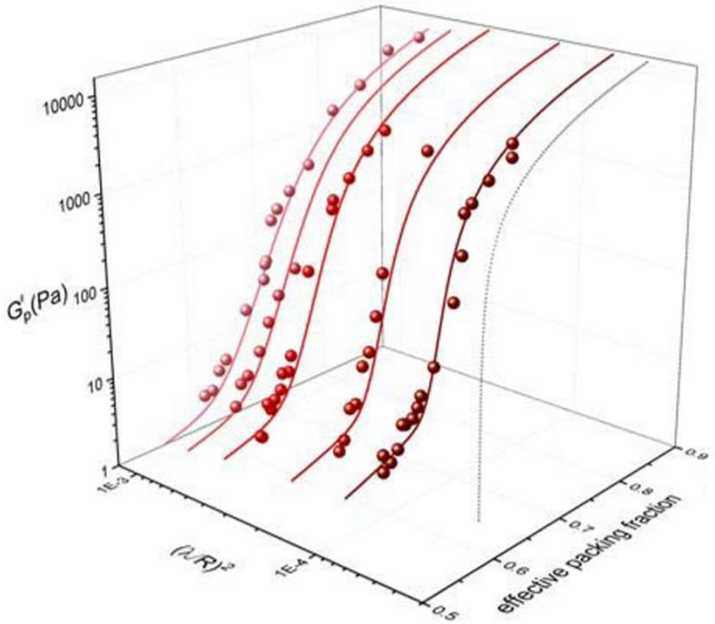

Figure 2.14. Comparison of EEI model to diffusing wave spectroscopy microrheology determined nanoemulsion plateau shear elastic moduli G'_p at varying concentration of NaCl. The PDMS O/W nanoemulsions having radius $a = R = 130$ nm are stabilized by 10 mM SDS containing 0, 10, 20, 40, and 90 mM NaCl (left to right) to vary the ionic strength of the system. The spherical dots indicate G'_p determined from the extracted mean square droplets from diffusing wave spectroscopy at $T = 22$ °C and the lines indicate G'_p determined by the EEI model as a function of effective packing fraction and different ionic strengths indicated by $(\lambda/R)^2$ where λ is the Debye length. The EEI model predictions are made using $\psi_0 = 230$ mV and otherwise the same parameters were used as determined by Figures 2.4 and 2.7. The effective packing fractions are determined as $(\phi_g/\phi_g^{(1)})\phi$ for the experimental data and $(\phi_c/\phi_{J,e})\phi$ for the EEI model calculations. The variables are: $\phi_g = 0.58$, $\phi_c = 0.646$, $\phi_{J,e}$ is defined where $F_{elec} = 5\ k_BT$ in the EEI model, and $\phi_g^{(1)}$ is determined by determining fitting to the α-relaxation time master curve for hard spheres taken from prior work by Brambilla *et al*[108]. The grey line shown without the data points indicates the athermal (T → 0 K) limit. Figure adapted from Braibanti *et al*.[109]

The EEI model values of G'_p can be matched to achieve good agreement with DWS measured values of G'_p over a wide range of NaCl concentrations set by ionic strength length scale (λ/R) as shown in Figure 2.14. This good agreement is only achieved through the use of effective packing or volume fractions rather than the determined parameters used to match the mechanical measurements shown in Figure 2.6. The effective droplet packing fractions for these measurements are adjusted to be $(\phi_g/\phi_g^{(1)})\phi$, were $\phi_g = 0.58$ is the glass transition volume fraction for hard spheres and $\phi_g^{(1)}$ is an adjustable parameter determined from fitting the light scattering

data to α-relaxation time collapse on a master curve for hard spheres, determined from a prior result[108]. The data can be described by the EEI model after adjusting the droplet volume fraction values to a new effective packing fractions calculated in the EEI model to $(\phi_c/\phi_{J,e})\phi$. The parameters used are: ϕ_c = 0.646 and $\phi_{J,e}$ is defined as the volume fraction at which the electrostatic free energy contribution F_{elec} calculated by the EEI model from parameters found in Figure 2.7, except for a fixed effective surface potential of ψ_0 = 230 mV, is $5k_BT$. The set of $\phi_{J,e}$ points determined from the data is close to the ϕ values at which EEI model predicts the electrostatic term to dominate for the all sets of different ionic strengths investigated here. Thus, we identify $\phi_{J,e}$ as the electrostatic jamming point, at which droplets experience repulsive force arising from the overlap of the electrostatic core-shells defined by the Debye layer.

Although good agreement of the EEI model with DWS measurements is demonstrated, the use of an effective packing fraction to corroborate DWS results indicates that the discrepancy between the DWS optical measurements and the mechanical measurements is present. The discrepancy between the two measurements is explored in Chapter 3 of this dissertation, in which we also show EEI model can be matched the DWS measurements using same parameters used to describe the mechanically measured G'_p without this *ad hoc* correction.

2.5 - Conclusion

We have shown that minimizing a total free energy with respect to an average microscopic droplet deformation parameter accounts well for the shear elasticity and osmotic pressure of concentrated disordered ionic emulsions and nanoemulsions for droplet volume fractions below, near, and above ϕ_c. The EEI model connects three principle energetic terms, entropic, electrostatic, and interfacial, of this total free energy using a near-equilibrium approach

that assumes disordered jamming of monodisperse deformable droplets while conserving droplet volume. Simultaneous fitting of measured $G'_p(\phi)$ curves for a wide range of droplet radii establishes the values of two universal parameters, ξ and α, that essentially set the relative strengths of the terms and are based fundamentally on complicated geometrical aspects of the disordered system. It is remarkable that such a simple free energy, when minimized, can properly capture such a wide range of measurements without resorting to a highly detailed microscopic description. Rapidly quenching uniform deformable objects to jam them in the presence of Brownian fluctuations creates a reproducibly statistically similar disordered structural state, so the emulsion system is technically out-of-equilibrium. Nevertheless, we have shown that near-equilibrium free energy minimization of the relatively simple EEI model, based on disordered jamming at ϕ_c, can serve surprisingly well in describing the collective behavior of ionic colloidal emulsions.

This EEI model, in combination with the two universal fit parameters that we have determined, can be used to predict rheological regimes of a wide variety of ionic emulsions. These entropic, electrostatic, and interfacial regimes reflect the dominance of a particular term in the free energy, and we have mapped boundaries of these regimes as a function of droplet radius and volume fraction for different Debye screening lengths. Moreover, we have explicitly shown the relative contributions to the free energy, osmotic pressure, and shear modulus that each of these terms makes. Although this EEI model provides a powerful predictive platform for emulsion rheology, it nevertheless must be used with discretion; as we have shown, introduction of non-amphiphilic salt can alter important parameters, such as the interfacial tension and the surface potential, in addition to the Debye screening length. Polydispersity can also affect the shape of G'_p and we have not attempted to include it in our description.

In future work, it would be interesting to test the utility of the model's predictions for monodisperse disordered microscale and nanoscale emulsions that have a wider range of ionic amphiphile and non-amphiphile concentrations. Likewise, it would be interesting to perform multi-scale Brownian or molecular dynamics simulations, which can incorporate complex behavior such as entropy contribution of ions, on dense disordered systems of constant-volume droplets stabilized by ionic surfactants to arrive at predictions for the two universal parameters. A more sophisticated model or simulation could be developed to incorporate the microscopic details of the system, such as the local coordination number and the distribution of the degree of deformation of constituent droplets, into predictions for $\Pi(\phi)$ and $G'_p(\phi)$. The EEI model could further be advanced into the regime of attractive ionic emulsions by incorporating the effects of secondary minima in the interactions between proximate surfaces of neighboring droplets[15, 23, 29, 87]. Moreover, the EEI model at present does not explicitly treat polydispersity, which can alter ϕ_c and also change the shape of $G'(\phi)$ and $\Pi(\phi)$ of emulsions. While challenging, extending the EEI model and simulations to include polydispersity, such as a peaked monomodal droplet size distribution, would also be useful.

Chapter 3 – Diffusing Wave Microrheology of Disordered Jammed Monodisperse Emulsions

Reproduced with permission from Kim, H.S., Şenbil, N., Zhang, C., Scheffold, F., Mason, T. G. "Diffusing Wave Microrheology of Highly Scattering Concentrated Monodisperse Emulsions", *Proc. Natl. Acad. Sci. U.S.A.*, 116 (16), 7766-7771 (2019).

3.1 - Introduction

Diffusing wave spectroscopy (DWS)[110-111] is a light scattering technique that can be used to measure time-dependent mean square displacements (MSDS), $\langle \Delta r^2(t) \rangle$, of uniform spherical probe particles in opaque, highly scattering colloidal dispersions. In DWS, the transport of light is modeled as a random walk having an optical transport mean free path ℓ^*. The diffusion equation is then applied to a specific sample-cell geometry, which typically has a thickness far in excess of ℓ^*, while taking into account the illumination and detection configuration used. DWS is a powerful approach because it is capable of measuring colloidal dynamics over a wide range of time scales, and it is also sensitive to very small probe displacements approaching 1 Å[110-114]. Provided that the scattering probes are well dispersed and dilute, their self-motion MSDs can be accurately inferred from the measured DWS intensity autocorrelation function[110-114].

By contrast, for probes at densities well beyond the dilute limit, collective light-scattering effects could significantly influence decays and plateaus in DWS correlation functions, particularly when probes are at high-volume fractions ϕ and have diameters comparable to or smaller than the wavelength of the illuminating light[112]. Because the standard analytical framework of DWS neglects collective scattering of colloidal probes at high densities, DWS

MSDs extracted for such dense colloidal systems do not necessarily represent the true self-motion of the probes. Consequently, using DWS MSDs for thermal-entropic passive microrheology[84, 115] of dense dispersions, including concentrated emulsions, would likely lead to inaccurate predictions of their linear viscoelastic moduli, since passive microrheology requires accurate self-motion MSDs in the generalized Stokes-Einstein relation (GSER)[67, 84].

Despite these potential issues related to collective scattering, DWS MSDs have been used since the inception of passive microrheology to infer the linear viscoelastic response of numerous soft materials, such as hard spheres[67, 84], emulsions[67, 84], polymer solutions[41, 84, 116-117], DNA solutions[118-120], actin solutions[121-123], microgels[124], and micellar solutions[125-127]. For at least some of these systems, and particularly for concentrated emulsions, collective scattering could play a significant role. In addition, early DWS studies of nonergodic soft materials[84], including concentrated emulsions, were taken using a simple DWS apparatus that did not force a final long-time decay[128]. As a consequence, for such nonergodic materials, the values of the plateaus varied significantly from run to run, precluding accurate comparisons of shear elastic moduli obtained using DWS-GSER microrheology with mechanical rheometry[67].

To alleviate this undesirable variability in DWS correlation functions of nonergodic materials, one effective solution involves introducing a second cell[129-130] or a slowly moving rigid scatterer[131-132] (e.g., etched glass having a rough surface) into the light path that includes the nonergodic soft material. The motion of this additional moving scatterer forces the DWS correlation function to decay fully at a certain long time, which can be controlled by the rate of its motion, without significantly affecting the correlation function at earlier times. This improvement in technique effectively ensures that early-time behavior and plateau values of the DWS correlation function, obtained by the digital correlator's hardware and software, are

reproducible from run to run both for ergodic and for nonergodic soft materials, at least over time scales significantly shorter than those associated with the time scale of the final forced decay[130-132]. Moreover, if the slowly moving rigid scatterer is rotated at a fixed angular frequency, such that identical scatterers of this rigid object move into the illuminating beam periodically every cycle, then DWS echo signals[133] can also be collected at times longer than the forced decay. Such DWS echo signals are useful because they extend the temporal range of the DWS correlation function and extracted MSDs to time scales of tens of seconds while keeping the total measurement time short, on the order of minutes.

Motivated by these improvements in DWS techniques for nonergodic systems and also by the need to rectify collective scattering effects in DWS of dense colloidal systems, which can adversely affect passive microrheology, we present a systematic experimental comparison of the plateau elastic shear moduli, G'_p, measured using both mechanical rheometry and modern DWS microrheology, of disordered, jammed, microscale monodisperse emulsions, as a function of ϕ. Because uncertainties in G'_p can be large in the jamming regime even for small uncertainties in ϕ, we perform both DWS and mechanical rheometry experiments on exactly the same emulsion samples, each of which has a highly controlled ϕ. By using a high-viscosity oil inside our droplets, we suppress entropic interfacial fluctuations that can otherwise be detected by DWS at very early times for less viscous droplets[134], and, to avoid complications introduced by inertia, we focus on time scales longer than inertial time scales[84, 113] when making microrheological interpretations. Here, we show that long-time plateau MSDs measured using DWS, when corrected for the ϕ-dependent average structure factor and used in the GSER, yield $G'_p(\phi)$ which matches that of macroscopic mechanical rheometry, as well as an analytical model of droplet jamming, over about three orders of magnitude as droplets jam. Our study represents a major

improvement over earlier microrheological measurements made using a simpler and less refined DWS technique[67, 84] that was not as accurate, did not account for the ϕ-dependent average structure factor, and demonstrated only a qualitative trend in $G'_p(\phi)$ in the jamming regime compared with mechanical rheometry. Moreover, our study goes beyond recent light-scattering work on concentrated nanoemulsions that did not include a direct comparison with a measured $G'_p(\phi)$ and that used an ad hoc ϕ-independent correction factor to rescale the microrheological $G'_p(\phi)$[109]. Given the strikingly accurate quantitative comparison that we have obtained for jammed emulsions, we anticipate that our experimental and analytical approaches could serve as a basis for improving quantitative DWS-GSER passive microrheology of other jammed disordered systems of highly scattering colloidal objects.

3.2 – Materials and Methods

3.2.1 – Monodisperse O/W Emulsions Preparation and Characterization

We make emulsions using SDS (Fisher Scientific; electrophoresis grade 99% purity), PDMS (Gelest Inc.; viscosity 350 cSt), and deionized water (Millipore Milli-Q; resistivity 18.2 MΩ·cm). We prepare 500 mL of a crude microscale premix emulsion having oil droplet volume fraction ϕ = 0.20 in 2.5 mM aqueous SDS solution using a mixer (Fisher Scientific, PowerGen 1000 S1, speed 3). After allowing any residual foam to disappear, we process this premix emulsion using a high flow rate microfluidic homogenizer (Microfluidics, M-110P; 75 μm diameter Y-chamber) at a liquid pressure of ~70 MPa. We process the resulting emulsion through this homogenizer 4 additional times before collecting and diluting the resulting emulsion in 500 mL of 60 mM aqueous SDS solution after the final pass. We repeat the above procedure until we obtained a large volume of polydisperse emulsion (~20 L). We prepare a master sample of concentrated monodisperse emulsions by performing size-fractionations on obtained large

batch of polydisperse emulsions. We use size-fractionation steps developed by Bibette *et al*.[59] to decrease the polydispersity and form relatively monodisperse emulsions. We concentrate the resulting uniform emulsions to a higher ϕ via centrifugation (Beckman L8-55 ultracentrifuge, SW-28 swinging bucket, 10k rpm, 1.25 h). When these uniform droplets are rapidly concentrated to high droplet volume fractions, PDMS emulsions form a dense plug of cream, which is a soft viscoelastic solid[15, 33, 35], at the top of a rigid polycarbonate centrifuge tube that can be readily separated from the relatively clear solution below. After removing this dense plug of cream with a thin spatula, we dilute it with a much larger volume of 10 mM SDS solution to reach $\phi \sim 0.1$. We repeat these centrifugation and dilution steps for a total of 4 times, thereby setting the SDS concentration in the aqueous bulk continuous phase to 10 mM. After the final centrifugation, we collect the concentrated elastic emulsion, mix it thoroughly so that any size-separation which might have occurred during the final centrifugation step is no longer present, and label this resulting monodisperse emulsion as the master uniform emulsion sample (~55 mL total volume). We store this master emulsion sample in a temperature-controlled chamber set at 20°C to avoid evaporation-condensation of water vapor onto the walls and lid of the container that can occur if the temperature is not fixed, thereby avoiding changes in ϕ. Moreover, we have used a container size to ensure that only a very small volume for such vapor is available above the master emulsion. We have characterized the droplet volume fraction of this master emulsion using a gravimetric evaporation method[99], $\phi_m = 0.729 \pm 0.006$.

Samples of emulsions at different ϕ near but below ϕ_m have been prepared by diluting the master emulsion sample with 10 mM SDS solution using an analytical balance (Denver Instruments APX-200, 0.1 mg precision). The resulting ϕ of each different sample can be calculated from these measured masses using measured densities of the SDS solution and of the

PDMS[99]. Each emulsion having $\phi < \phi_m$ has been stirred with a small spatula for minutes to ensure complete mixing before measurements made using mechanical rheometry and DWS. At each ϕ, approximately 0.5 mL of emulsion is used for mechanical rheometry, and 1.5 mL of the exact same emulsion is used for DWS. The sample for DWS has been stored in a small vial with almost no headspace to prevent potential changes in ϕ that could result from water evaporation. The master emulsion is also diluted in 10 mM SDS to $\phi \sim 10^{-4}$ and then characterized by multiangle DLS (LS Spectrometer; LS Instruments) over 60°- 120° scattering angles, yielding an average hydrodynamic droplet radius $a = 459 \pm 15$ nm. The polydispersity is $\delta a/a \approx 0.176$, where δa is the standard deviation of the radial droplet size distribution.

3.2.2 – Mechanical Shear Rheometry

Before making measurements on emulsions, we ensured that our rheometer was calibrated by using a polymeric viscoelastic standard in an oscillatory frequency sweep; both the magnitude and frequency associated with the crossover matched reported values for the standard to within ±10%. At each ϕ, the loaded emulsion was subjected to a pre-shear at a strain rate $\dot{\gamma} = 100\ s^{-1}$ for a duration of 60 s. After this pre-shear, the emulsion was allowed to relax for 300 s prior to starting the oscillatory rheological tests. At a shear strain $\gamma = 0.01$, a frequency sweep was performed from an angular frequency $\omega = 10$ rad/s down to 0.01 rad/s. A strain sweep at $\omega = 1$ rad/s from $\gamma = 0.002$ up to 2 was also performed, and we verified that the strain of 0.01 selected for the frequency sweep was below the yield strain, ensuring that reported $|G^*|$ and G'_p values correspond to the linear regime. In the reported frequency sweeps, at lower ϕ, the reliable range of is limited by the rheometer's torque transducer at low ω and by the inertia of the cone at high

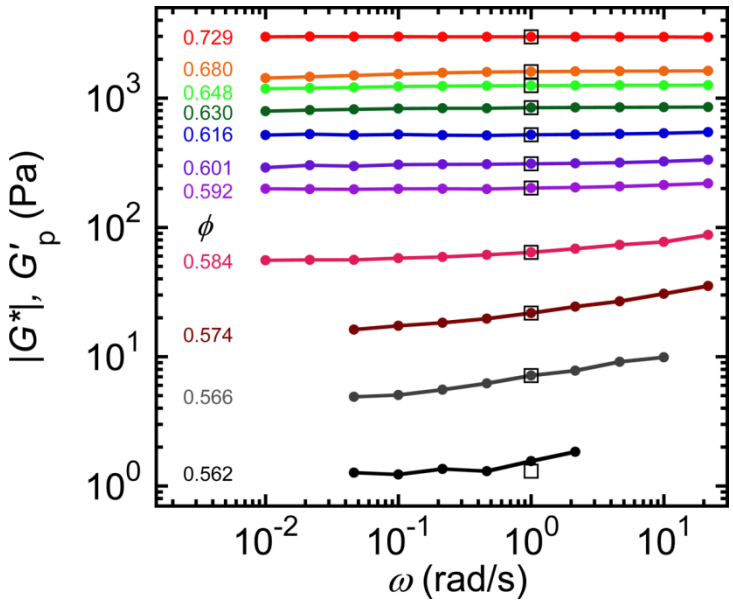

Figure 3.1. Measured frequency-dependent shear modulus of fractionated PDMS O/W a = 459 nm emulsion stabilized using 10 mM SDS. The magnitude of the complex shear modulus $|G^*(\omega)|$ (solid circles, lines guide the eye) as a function of frequency ω at droplet volume fractions, ϕ ranging from 0.729 to 0.562 (top to bottom, on left at a fixed peak shear strain of γ = 0.01 is shown. Measured plateau values of the mechanical shear storage modulus $G'_{p,mech}$ (open squares at 1 rad/s) are almost equal to $|G^*(\omega)|$ over the frequency range explored.

ω, so reported frequency sweeps at the lowest do not cover as wide a range in as at higher. The temperature T during all measurements using mechanical rheometry was regulated by a circulating water bath to T = 20 ± 1 °C. The magnitudes of the linear complex shear modulus $|G^*(\omega)|$ for the set of 10 mM SDS-stabilized PDMS O/W monodisperse emulsions, which all have an average droplet radius of a = 459 nm, are characterized by mechanical rheometry at room temperature T = 20 °C. The frequency dependent behavior of $|G^*(\omega)|$ for $0.562 < \phi < 0.729$ is shown in Figure 3.1. Over the range of ϕ measured, the emulsions are dominantly elastic and exhibit a nearly frequency-independent dominant elastic storage modulus $G'_{p,mech}$, which spans about three orders of magnitude. At the lowest ϕ for which torques are above the lower limit of the rheometer's transducer, we find that the rise in both $|G^*|$ and $G'_{p,mech}$ is very rapid as ϕ is

increased only slightly, consistent with prior linear rheological measurements on similar monodisperse emulsions that have different average a [35].

3.2.3 – Diffusing Wave Spectroscopy

We perform DWS measurements (DWS RheoLab III; LS Instruments) to obtain the intensity correlation functions for emulsions at different ϕ. Each emulsion sample is loaded into an L = 5 mm path-length glass cuvette. After the initial loading, each cuvette is very gently centrifuged to remove the air bubbles without creating gradients in ϕ; after removing air bubbles, each emulsion is then allowed to equilibrate for 1 day before any DWS measurements are performed. At all times, the temperature is controlled and maintained at T = 20 ± 0.1 °C. A coherent light source (wavelength λ_{DWS} = 687 nm) is directed to the surface of a rotating ground-glass diffuser so that the speckle beam from the rotating glass diffuser can provide an efficient ensemble-averaged signal from the recorded correlation echoes[133]. The scattered light is collected in a transmission or in a backscattering geometry to obtain normalized intensity autocorrelation function $g_2(t)$ in the homodyne limit. The values of ℓ^* of each emulsion samples were also determined by comparing time-averaged transmission intensities from these emulsions with transmission intensities measured for a set of polystyrene latex reference samples having different sizes with known ℓ^* using the DWS instrument's software[114]. A total of 5 - 10 runs of 300 s were performed and averaged for each emulsion sample[112]. DWS echo data are also acquired at longer times over 60 s for each run.

3.2.4 – Entropic-Electrostatic-Interfacial Emulsion Model

We use the EEI model[135] to calculate the predicted G'_p for our emulsions as described in Chapter 2 of this dissertation. For our specific fractionated emulsion system and measurement conditions, we use the following parameter values: average radius a = 459 nm and temperature

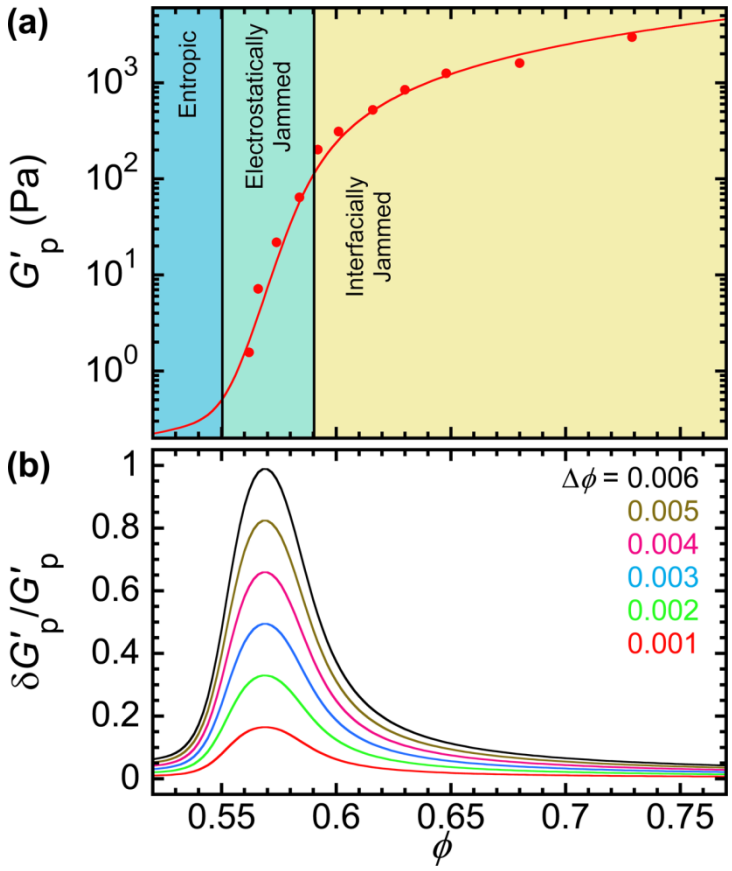

Figure 3.2. EEI Model comparison and results for plateau elastic shear moduli of measured emulsion sample. (a) Measured mechanical plateau elastic shear moduli, $G'_{p,mech}(\phi)$, of a monodisperse emulsion having an average droplet radius a = 459 nm (red solid circles). Red solid line: prediction of $G'_{p,EEI}(\phi)$ based on a model of disordered, uniform, concentrated, ionically stabilized droplets that has entropic, electrostatic, and interfacial terms in its free energy [*i.e.*, the EEI model[135]; main text]. Regimes in ϕ having different dominant contributions to G'_p in the EEI model are indicated by background colors: entropic (blue), electrostatic (green), and interfacial (yellow). (b) Predicted relative uncertainty in G'_p, given by $\delta G'_p/ G'_p$, associated with different uncertainties in ϕ given by $\Delta\phi$ (Upper Right Inset).

T = 293 K. Other parameters that we use in the EEI model have been obtained for SDS-stabilized PDMS O/W emulsions having the same bulk SDS concentration of 10 mM: surface tension σ = 9.8 mN/m, effective surface potential ψ_0 = 270 mV, Debye screening length λ_D = 3.4 nm, disordered hard sphere jamming point ϕ_c = 0.646, and dimensionless pre-factor parameters α = 0.85 and ξ = 0.15. We identified the range of ϕ at which the contributions to G'_p are dominated

by the entropic, electrostatic, and interfacial contributions to the free energy per droplet, and labeled these regimes entropic, electrostatic jamming, and interfacial jamming regimes, respectively (see Figure 3.2).

3.3 – Results and Discussion

3.3.1 – Mechanical Plateau Shear Modulus and Entropic-Electrostatic-Interfacial Model

In Figure 3.2(a), we compare the mechanically measured plateau elastic shear moduli $G'_{p,mech}$ of the monodisperse emulsion in this study, which has an average droplet radius a = 459 nm to predicted values of $G'_{p,EEI}$ obtained by the EEI model[135] for concentrated, ionically stabilized, disordered monodisperse O/W emulsions near and above the jamming point. The EEI model assumes that minimization of a quasi-equilibrium free energy, which includes terms related to entropic crowding, screened electrostatic repulsions, and droplet interfacial deformation, is a reasonable approximation for disordered emulsions in the weak jamming limit. The parameter values that we use here in the EEI model are those that have been shown to describe the mechanically measured $G'_{p,mech}(\phi)$ of other similar polydimethyl siloxane (PDMS) O/W monodisperse emulsions having nano- and microscale radii at the same 10 mM bulk SDS concentration[135]. By determining the dominant contribution to $G'_{p,EEI}$ at different ϕ [135], we find that $0.562 < \phi < 0.592$ corresponds to the electrostatically jammed regime (*i.e.*, screened charge repulsion dominates) and $\phi \geq 0.592$ corresponds to the interfacially jammed regime (*i.e.*, droplet interfacial deformation dominates). The entropic regime lies below the ϕ range that we have explored here. We find that $G'_{p,mech}(\phi)$ is in excellent agreement with $G'_{p,EEI}(\phi)$ using a = 459 nm. Thus, $G'_{p,mech}(\phi)$ of this emulsion is highly consistent with past mechanical measurements on other fractionated emulsions that have similar compositions.

Since the EEI model smoothly captures the steep rise in $G'_p(\phi)$, we use it to demonstrate that even relatively small experimental uncertainties in ϕ of emulsion samples can lead to very large uncertainties in G'_p at the onset of jamming. We first numerically calculate the first partial derivative of $G'_{p,EEI}$ with respect to ϕ. In Figure 3.2(b), we plot the predicted relative magnitude of the variation in $G'_p(\phi)$, which is proportional to this first partial derivative and also proportional to the magnitude of the uncertainty in the droplet volume fraction, $\Delta\phi$. Even for small $\Delta\phi$ significantly less than 1%, measured values of G'_p near the onset of jamming could exhibit significant scatter and uncertainty of a factor of 2 or more. This highlights the need to control ϕ very carefully in all studies of mechanical properties of jammed emulsions, irrespective of whether these measurements are based on mechanical rheometry or on light scattering. Here, we have controlled ϕ to a high degree and have kept $\Delta\phi$ very low. Moreover, we have ensured a direct comparison between mechanical and light scattering measurements on exactly the same emulsion at the same set of ϕ values, thereby avoiding the large uncertainties in G'_p highlighted by the peaks in Figure 3.2(b), which adversely affected a prior comparison near and above the jamming point[67].

3.3.2 – Diffusing Wave Spectroscopy: Intensity Autocorrelation Function

To facilitate comparison with mechanical results, we performed DWS studies on the same emulsion at identical ϕ. The measured, normalized, time-averaged intensity autocorrelation functions, $g_2(t)$ - 1, for each different ϕ are shown for DWS transmission (Figure 3.3(a)) and backscattering (Figure 3.3(b)). In these measured $g_2(t)$ - 1, after initial decays, we observe long-time plateaus over at least several orders of magnitude in t, except at the lowest ϕ. Such plateau behavior indicates that droplets in the emulsion are confined by other surrounding droplets. The

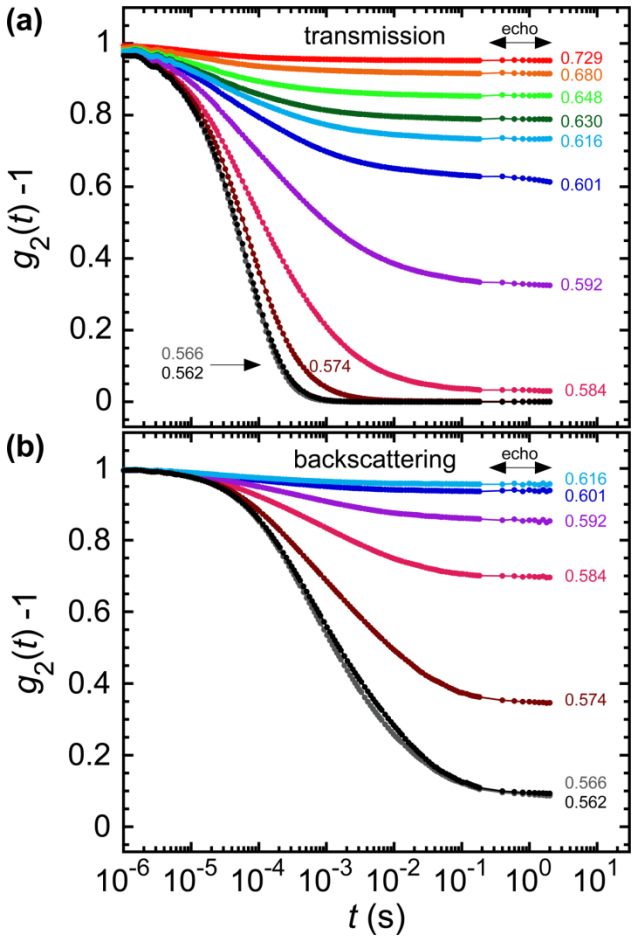

Figure 3.3. Normalized, averaged temporal DWS intensity correlation functions, $g_2(t)$ - 1, of a monodisperse emulsion having a = 459 nm. The droplets have the same set of ϕ (values on right) as in Figure 3.2(a) using (a) transmission and (b) backscattering configuration of the DWS as described in section 3.2.3. DWS echo data are indicated by arrows in the range $t \gtrsim 0.2$ seconds. Lines guide the eye.

magnitudes of these plateaus increase systematically toward unity for larger ϕ, indicating greater droplet confinement. For $\phi \geq 0.574$, transmission $g_2(t) - 1$ curves remain above the baseline even for long times extending into the echo regime. By contrast, for $\phi < 0.574$, $g_2(t)$ - 1 becomes unresolvable from the baseline at long times; so, plateau behavior, if present, cannot be readily determined using transmission DWS for such low ϕ. To overcome this limitation, we also measure $g_2(t)$ - 1 using backscattering DWS. We also test several larger ϕ to compare backscattering plateaus with clearly resolved transmission plateaus. For $\phi > 0.616$, the

backscattering DWS correlation functions do not decay sufficiently to be readily analyzed. For the two lowest ϕ, $g_2(t)$ - 1 are similar; this is likely caused by experimental uncertainties when setting ϕ.

3.3.3 – Extracting Apparent Mean Square Displacements of Dense Probes

At each ϕ, we use ℓ^* and details of the scattering geometries to extract apparent MSDs $\langle \Delta r^2_a(t) \rangle$ from DWS $g_2(t)$ - 1 using standard procedures[136]. We extract the normalized field correlation function $g_1(t)$ using the Siegert relation $g_2(t) = 1 + g_1^2(t)$, where $\beta \sim 0.95$ is the instrument-specific coherence factor that can be obtained experimentally (5) by extrapolation to $t \rightarrow 0$. We then determine dimensionless $x(t)$, describing the ensemble- and time-average droplet translational dynamics, in the transmission slab geometry using[112]:

$$g_1(t) = \frac{\left(\frac{L}{\ell^*} + \frac{4}{3}\right)\sqrt{x(t)}}{\left(1 + \frac{4}{9}x(t)\right)\sinh\left(\frac{L\sqrt{x(t)}}{\ell^*}\right) + \frac{4}{3}\sqrt{x(t)}\cosh\left(\frac{L\sqrt{x(t)}}{\ell^*}\right)} \qquad (3.1)$$

where $k = 2\pi n_s/\lambda_{DWS}$ is the wavenumber in the solvent and $x(t) = k^2\langle \Delta r^2_a(t) \rangle$. In the backscattering geometry, we independently determine the γ_{VH} factor for cross-polarized detection and also the photon loss parameter c using 910 nm diameter polystyrene spheres, which have $\ell^* \sim 200$ μm similar to the emulsion samples, by matching backscattering $g_1(t)$ with transmission $g_1(t)$ using:

$$g_1(t) \propto \exp\left(-\gamma_{VH}\sqrt{x(t)+c}\right) \Big/ \left(1 + \frac{2}{3}\sqrt{x(t)+c}\right) \qquad (3.2)$$

The photon loss parameter c accounts for light leakage out of the cuvette's side walls or via transmission[114]. Using these independently determined values, $c = 0.07$ and $\gamma_{VH} = 1.95$, the MSDs for droplets in the backscattering geometry are then calculated. We find that MSDs

obtained from transmission and backscattering experiments for the same emulsions overlap. The transmission experiment probes longer light paths and thus are more accurate for smaller displacements (*i.e.* short times, high concentrations), whereas backscattering experiments perform better at larger displacements, extending the range of long-time plateau displacements that can be probed by DWS.

3.3.4 –True Self-Motion Mean Square Displacements of Probes

For passive DWS microrheology using tracer probes at low $\phi \sim 1$ - 2% [84, 119, 127], collective scattering effects are negligible and $\langle \Delta r^2_a(t) \rangle$ reduces to the true $\langle \Delta r^2(t) \rangle$ associated with probe self-motion. However, for higher probe concentrations, as in the emulsions here, the individual scattering processes are modulated by the microstructure. In single scattering, this leads to the well-known de Gennes narrowing of the intensity-spectrum $I(q, \omega)$, where q is the magnitude of the scattering wavevector and ω is the frequency of quasi-elastically scattered coherent radiation, near the peak of the structure factor of simple liquids[137]. The experimental collective diffusion coefficient of colloids $D_c \propto 1/S(0)$ measured by dynamic light scattering increases with concentration, where the structure factor at low q, $S(0)$, drops sharply[137-139]. In DWS, collective scattering effects contribute at all scattering wavevectors; consequently, to obtain the self-motion MSD of probes, it is necessary to correct the apparent MSD by multiplying it with the average structure factor $\langle S(q) \rangle$ of the emulsion: $\langle \Delta r^2(t) \rangle = \langle S(q) \rangle \langle \Delta r^2_a(t) \rangle$. $\langle S(q) \rangle$ is defined by the integral of $S(q)$, over all $q \in [0, 2k]$, weighted by the scattering power $P(q)$ and normalizing: $\langle S(q) \rangle = \int_0^{2k} q^3 P(q) S(q) dq \Big/ \int_0^{2k} q^3 P(q) dq$, where $P(q)$ denotes the form factor of the scatterers and $k = 2\pi n_s/\lambda_{DWS}$ is the wavenumber in the solvent with refractive index $n_s = 1.33$ for water[136, 140]. In correcting the apparent MSD, we have neglected a possible

contribution by an additional possible q-dependent term due to hydrodynamic interactions, known as the distinct part of the hydrodynamic function $H_d(q)$[136, 139, 141], because the distinct part of the hydrodynamic function is small in comparison. The contribution of $H_d(q)$ is secondary to $\langle S(q)\rangle$, and over the range of densities previously studied, it exhibits relatively weak q-dependent oscillations ± 20%, which largely cancel out when taking the average over all scattering vectors. For $q \gg q_{max}$ it vanishes completely. Moreover, hydrodynamic effects would not be expected to influence the measured long-time plateau MSD of a solid emulsion.

To quantify $\langle S(q)\rangle$, we determine the $1/\ell^*(\phi)$ for the emulsion with a = 459 nm over a wide range of ϕ from the measured $\ell^*(\phi)$ (Figure 3.4(a)). Collective scattering also influences static light scattering and thus ℓ^*. Typically, this leads to an increase of ℓ^*, although in some particular cases it can also lead a reduction, *e.g.* close to a photonic pseudo-gap or for high refractive index scatterers[142-143]. In Figure 3.4(a) we plot the calculated $1/\ell^*_{ISA} \propto \phi$ (dashed line) in the absence of collective scattering, also known as the independent scattering approximation (ISA). Using n_s = 1.33 for water, we infer that the refractive index of the oil inside the droplets is n = 1.401 using the criterion that $1/\ell^*_{ISA}$ and $1/\ell^*$ must merge as $\phi \rightarrow 0$. This oil refractive index is in excellent agreement with refractometry measurements that we have made (n = 1.40 at $\lambda \sim$ 580 nm) and also the supplier's reference data (n = 1.403). Knowing ℓ^*_{ISA}, we determine $\langle S(q)\rangle$ directly by taking advantage of a local collective scattering approximation (CSA) for spherical scatterers: $\langle S(q)\rangle = \ell^*_{ISA}/\ell^*$ [140] (Figure 3.4(b)). The validity of this relation has been demonstrated for micron sized Mie scatterers, polystyrene spheres with n ≃ 1.6 in water, up to concentrations of $\phi \sim 0.5$ [140]. We emphasize however, that in the Rayleigh-Gans-Debye limit, $\frac{2\pi}{\lambda/n_s} a \left|1-\frac{n}{n_s}\right| \ll 1$, CSA is not restricted to $\phi < 0.5$. It is strictly valid as long as the scatterers

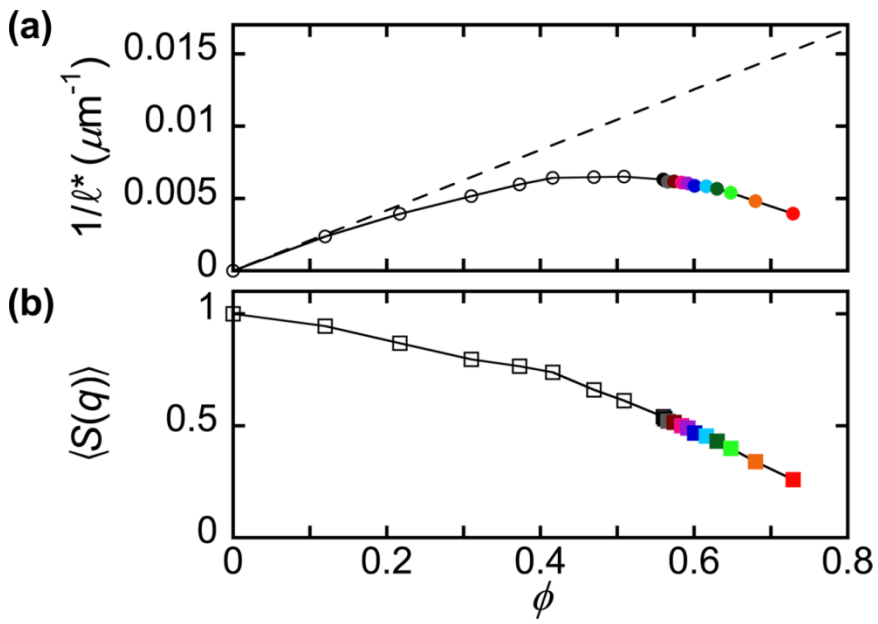

Figure 3.4. Mean free path of optical transport ℓ^* and the average structure factor $\langle S(q)\rangle$. (a) Measured inverse mean free path of optical transport, $1/\ell^*$ (circles), for a monodisperse emulsion having a = 459 nm as a function of ϕ. Colored solid circles encode ϕ of elastically jammed droplets (Figure 3.3). Solid line guides the eye. Straight dashed line corresponds to the ISA (main text) and approaches the measured $1/\ell^*$ at low ϕ. (b) Measured average ϕ-dependent structure factor $\langle S(q)\rangle$ (squares) determined by dividing $1/\ell^*$ by the extrapolated dashed line $1/\ell^*_{\mathrm{ISA}}$ in (a). Line guides the eye. Solid squares are color coded as in (a).

retain their spherical shape, and it is independent of any prior knowledge about $S(q)$. In our case, $\frac{2\pi}{\lambda/n_s} a\left|1-\frac{n}{n_s}\right| = 0.3$ and we thus expect the CSA to hold quantitatively up to concentrations $\phi \sim$ 0.75, beyond which droplets start to deform. Based on the EEI model[135], we calculate that the average surface area per droplet has changed by only ≈ 2% at the largest $\phi = 0.729$ we probe, so the droplets remain nearly spherical for all ϕ in our study. Interestingly, $\langle S(q)\rangle$ is reduced by nearly a factor of 4 at the highest ϕ we explore. Thus, accounting for collective scattering necessitates substantial ϕ-dependent corrections to DWS MSDs in concentrated probe systems, as we have demonstrated for concentrated emulsions.

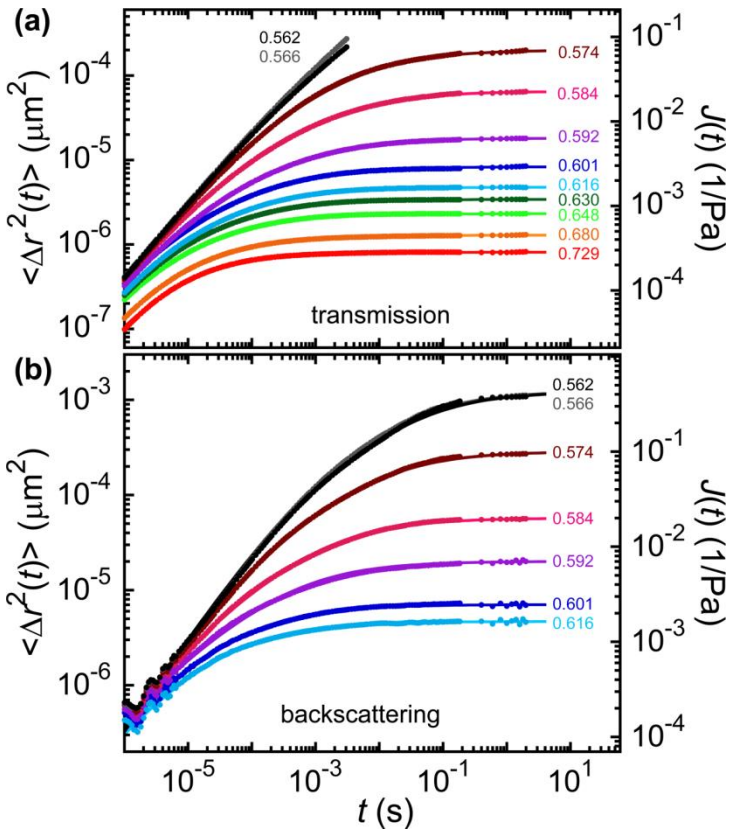

Figure 3.5. Ensemble-averaged temporal mean square displacements, $\langle \Delta r^2(t) \rangle$. Self-motion mean square displacement $\langle \Delta r^2(t) \rangle$ in a jammed monodisperse emulsion are extracted from $g_2(t)$ - 1 (Figure 3.3) using $1/\ell^*$ values (Figure 3.4(a)) after correcting with ϕ-dependent $\langle S(q) \rangle$ (Figure 3.4(b)) measured from (a) transmission DWS and (b) backscattering DWS. Solid lines are least-squares fits to an emulsion MSD model in equation (3.11); labels for each ϕ are color coded as in Figure 3.3. Right axes show shear creep compliance $J(t) \sim \langle \Delta r^2(t) \rangle$ obtained via passive microrheology using the GSER. In (a), we display only the portions of the transmission MSDs for $\phi = 0.562$ and 0.566 that can be reliably extracted above the baseline of $g_2(t)$ - 1.

We correct $\langle \Delta r^2_a(t) \rangle$ using the empirically determined $\langle S(q) \rangle$, yielding $\langle \Delta r^2(t) \rangle$ corresponding to true droplet self-motion. DWS transmission results are shown in Figure 3.5(a). The measured MSDS increase nearly linearly at short times ($t \lesssim 10^{-5}$ s), gradually bend, and saturate to plateau values at long times ($t \gtrsim 10^{-1}$ s). The transmission MSDs for $\phi = 0.562$ and 0.566 have been truncated at longer times because $g_2(t)$ - 1 becomes indistinguishable from the baseline there. For lower ϕ, backscattering DWS $g_2(t)$ - 1 [cross-polarized detection, denoted VH[114]] provides a more reliable result for $\langle \Delta r^2(t) \rangle$ (Figure 3.5(b)). Backscattering MSDs have

nearly the same shapes and long-time plateau values as transmission MSDs, yet backscattering MSDs at early times are noisier because light paths are shorter overall and there is less averaging than in transmission. As ϕ is raised, the long-time plateau MSDS $\langle \Delta r^2 \rangle_p$ decrease, indicating higher droplet confinement.

3.3.5 – DWS-GSER Microrheology

We analyze these droplet self-motion MSDs by developing a time-domain fitting function that accounts for the gradual bend in the shape of the dense emulsion MSDs, in addition to the short-time linear rise associated with a high-frequency viscosity η_∞ and a long-time G'_p.

The generalized Stokes-Einstein relation (GSER) for the frequency-dependent viscoelastic shear modulus using a 3D MSD, assuming stick boundary conditions, and ignoring inertia is given by[84]:

$$\tilde{G}(s) = \frac{k_B T}{\pi a s \left\langle \Delta \tilde{r}^2(s) \right\rangle}, \tag{3.3}$$

where s is the Laplace frequency, a is the radius of a probe sphere, k_B is Boltzmann's constant, and T is the temperature. We re-write this, solving for the MSD in the Laplace domain in terms of the s-dependent shear modulus $\tilde{G}$:

$$\left\langle \Delta \tilde{r}^2(s) \right\rangle = \frac{k_B T}{\pi a s \tilde{G}(s)}. \tag{3.4}$$

We assume that a suitable model for the viscoelastic modulus of dense emulsions includes constant and linear terms appropriate for a harmonically bound Brownian particle as well as a term proportional to $s^{1/2}$ [67, 85]:

$$\tilde{G}(s) = G'_p[1 + (s\tau)^{1/2}] + \eta_\infty s. \tag{3.5}$$

This gradual bend for dense emulsion systems can be attributed to an $s^{1/2}$ contribution to the frequency-dependent viscoelastic modulus in the Laplace frequency s domain[67, 85]. We have introduced a time scale τ, associated with the $s^{1/2}$ power-law term. We reason that the magnitude of this $s^{1/2}$ term is most appropriately set by G'_{p}, since either electrostatic or interfacial contributions to the quasi-equilibrium free energy can dominate G'_{p} over the range of ϕ that we explore in our study. We substitute this model into the equation for the Laplace-domain MSD and re-express the result using factors in the denominator that can be readily separated:

$$\left\langle \Delta\tilde{r}^2(s) \right\rangle = \frac{k_{\mathrm{B}}T}{\pi a \eta_\infty} \frac{1}{s(s^{1/2}+y)(s^{1/2}+z)}, \tag{3.6}$$

where we have defined y and z such that

$$y+z = G'_{\mathrm{p}}\tau^{1/2} \Big/ \eta_\infty \tag{3.7}$$

and

$$yz = G'_{\mathrm{p}} / \eta_\infty . \tag{3.8}$$

Here, the value of G'_{p} is related to the long-time plateau value of the MSD through the GSER in that limit:

$$G'_{\mathrm{p}} = k_{\mathrm{B}}T \Big/ \left(\pi a \left\langle \Delta r^2 \right\rangle_{\mathrm{p}} \right). \tag{3.9}$$

The prefactor in this equation for plateau values differs from the prefactor proposed in earlier work (see equation (16) of reference by Mason *et al.*[67]), and the above equation for plateau values is completely self-consistent with the broader framework of the GSER. The complete time-domain MSD is given by the inverse Laplace transform operation, L^{-1}, acting on the frequency domain MSD:

$$\left\langle \Delta r^2(t) \right\rangle = L^{-1}\left\{ \left\langle \Delta\tilde{r}^2(s) \right\rangle \right\}. \tag{3.10}$$

Using Mathematica functions *Apart* and *InverseLaplaceTransform*, we obtain the time-domain MSD involving the complementary error function, erfc:

$$\left\langle \Delta r^2(t) \right\rangle = \frac{k_B T}{\pi a \eta_\infty} \frac{(y-z) + z e^{y^2 t} \mathrm{erfc}\left(y\sqrt{t}\right) - y e^{z^2 t} \mathrm{erfc}\left(z\sqrt{t}\right)}{y^2 z - y z^2}. \tag{3.11}$$

Using this equation (3.11), which has three fitting parameters, η_∞, G'_p, and a time scale τ associated with the $s^{1/2}$ power law, we least-squares fit both transmission and backscattering MSDs (lines in Figure 3.5). We denote the values of G'_p obtained by equation (3.11) as $G'_{p,GSER}$ to distinguish them from mechanical results. For all ϕ, we find excellent agreement between the fits and measured MSDs.

In addition, because the MSDs are proportional to the linear viscoelastic shear creep compliance, $J(t)$, we directly report the measured and fitted $J(t)$ (Figure 3.5, right axes). Assuming stick boundary conditions for the GSER[115]:

$$J(t) = \frac{\pi a \left\langle \Delta r^2(t) \right\rangle}{k_B T}, \tag{3.12}$$

which after substitution of the MSD yields:

$$J(t) = \frac{(y-z) + z e^{y^2 t} \mathrm{erfc}\left(y\sqrt{t}\right) - y e^{z^2 t} \mathrm{erfc}\left(z\sqrt{t}\right)}{\eta_\infty \left(y^2 z - y z^2\right)}. \tag{3.13}$$

Considering the long-time limit, the plateau creep compliance J_p is proportional to the long-time plateau MSD:

$$J_p = 1 \Big/ G'_p = \pi a \left\langle \Delta r^2 \right\rangle_p \Big/ \left(k_B T\right). \tag{3.14}$$

3.3.6 – Comparison: DWS-GSER and Mechanical Plateau Shear Moduli

In Figure 3.6, we plot the microrheological $G'_{p,GSER}(\phi)$ obtained as fit parameters to DWS self-motion MSDs and compare these directly to the macroscopic mechanical $G'_{p,mech}(\phi)$ and the predicted $G'_{p,EEI}(\phi)$ of the EEI model. Over the entire range of ϕ, we find excellent agreement between DWS microrheological and mechanical G'_p measurements without applying any arbitrary correction factors, which had been previously applied to dense emulsion systems on an *ad hoc* and ϕ-independent basis[67, 109]. Accounting for collective scattering effects in DWS MSDs by using ϕ-dependent $\langle S(q) \rangle$, based on the measured $\ell^*(\phi)$, is necessary to achieve such quantitative agreement.

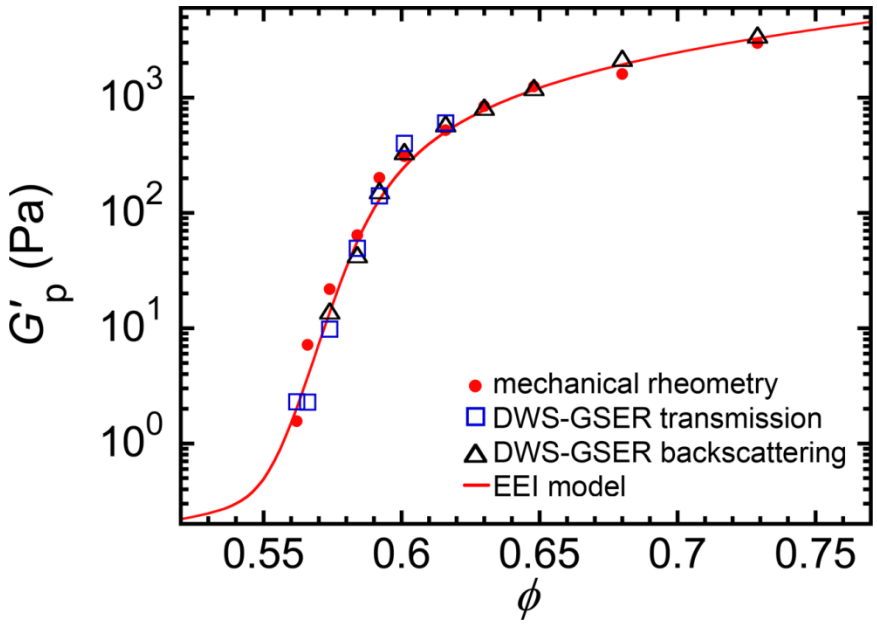

Figure 3.6. Comparison of plateau shear elastic moduli G'_p of jammed a = 459 nm monodisperse emulsion. $G'_{p,mech}(\phi)$ was measured using mechanical shear rheometry (solid red circles) (Figure 3.1). $G'_{p,GSER}(\phi)$ was measured using the $\langle S(q) \rangle$-corrected plateau DWS MSDs at long times t in Figure 3.5 through the GSER of passive microrheology: transmission (open black triangles) and backscattering (open blue squares). Red solid line shows $G'_{p,EEI}(\phi)$ predicted by the EEI model.

3.3.7 – Plateau Shear Moduli and $s^{1/2}$ Viscoelastic Response

We find also that $\tau(\phi)$ decreases strongly as droplets jam toward larger ϕ (Figure 3.7(a)). In addition, by plotting $G'_{p,GSER}$ vs. τ (Figure 3.7(b)), we find that an empirical power-law relationship $G'_{p,GSER} \sim \tau^{-\chi}$, where $\chi = 0.86 \pm 0.02$, holds through the jamming regime over many orders of magnitude in both $G'_{p,GSER}$ and τ. Thus, the low-frequency plateau viscoelastic moduli of jammed emulsions appear to be correlated in a nontrivial manner to the time scales associated with the higher-frequency $s^{1/2}$ viscoelastic response.

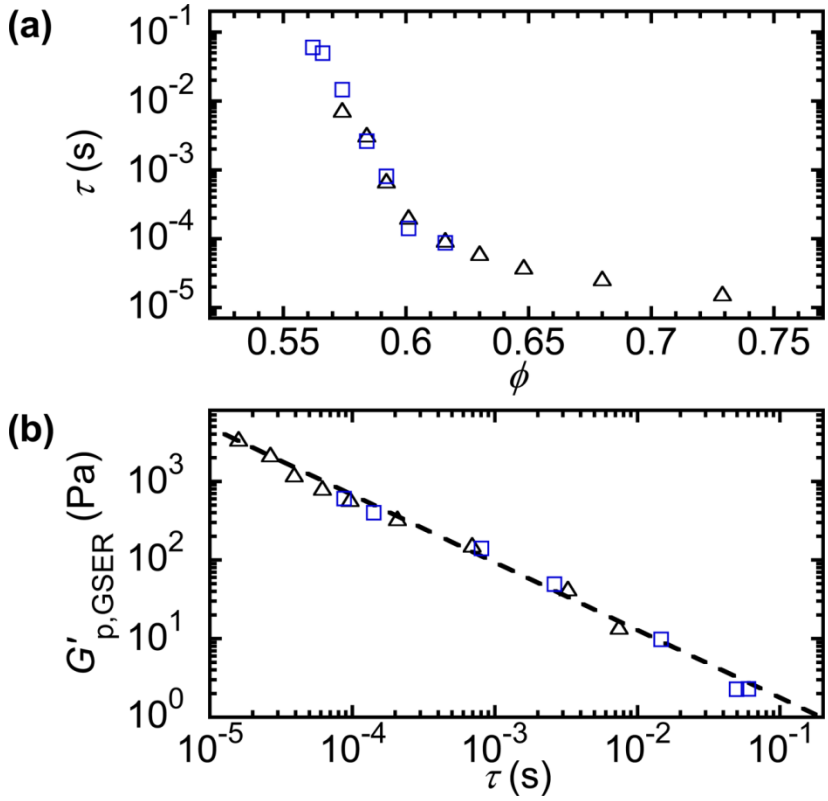

Figure 3.7. Volume fraction dependent τ-values for a = 459 nm jammed monodisperse emulsion determined from DWS-GSER. (a) Characteristic time scale τ of the $(s\tau)^{1/2}$ term in the viscoelastic emulsion model given in equation (3.11), obtained from fits to DWS MSDs in Figure 3.5, as a function of ϕ measured in transmission (open black triangles), and backscattering (open blue squares). (b) Plateau elastic storage modulus $G'_{p,GSER}$ as a function of τ, both obtained as fit parameters of DWS MSDs in Figure 3.5. Symbols are as in (a). Dashed line: fit using a power law, $G'_{p,GSER} \sim \tau^{-\chi}$, yielding an exponent $\chi = 0.86 \pm 0.02$.

3.3.8 – DWS MSDs at Very Short Sub-μs Times

Several different effects make the interpretation of DWS $g_2(t)$ - 1 at very short times particularly challenging. Backscattering DWS creates a much shorter overall distribution of light paths, and this complicates analysis at very short times; so, our discussion here largely centers on transmission DWS. Besides the simple translational motion of the probes associated with an effective high frequency viscosity η_∞, the two most prominent influences on DWS $g_2(t)$ - 1 are the effective inertia of the droplet-probes[84, 113] as well as their shape fluctuations[134]. We have largely suppressed shape fluctuations by using a PDMS oil inside droplets that has a higher viscosity, over one order of magnitude, compared to the oil viscosity at which shape fluctuations of similarly sized oil droplets in water have been readily observed[134]. However, the influence of the inertia of the droplet-probes in our study can still be seen for time scales shorter than the characteristic inertial time[113], and we find that DWS MSDs of droplets in our system have log-slopes greater somewhat larger than one for these very early times (*i.e*. extracted MSDs appear super-diffusive). Inertial effects are most evident at the few lowest values of ϕ we have studied. Although we only fit DWS self-motion MSDs for times greater than the characteristic inertial time to obtain rheological parameters, the influence of probe inertia on the fit parameter η_∞ becomes evident at these lower values of ϕ.

In Figure 3.8, we report the values of the fit parameter $\eta_\infty(\phi)$ for the emulsions in our study. For large enough ϕ ($\phi > 0.60$) beyond which short-time noise does not adversely influence the MSDs, we find that $\eta_\infty(\phi)$ rises with increasing ϕ. The rise in $\eta_\infty(\phi)$ for $\phi > 0.60$ could potentially be explained in the future by a model that considers the complex viscous flows in the continuous phase of a jammed and weakly deformed emulsion at high ϕ. Since the quasi-equilibrium EEI model does not include any hydrodynamic contributions, it can only be used to

compare with experimental G'_p. However, for $\phi < 0.60$ the fit parameter values for $\eta_\infty(\phi)$ in Figure 3.8 cannot be taken literally as rheological values because of inertial effects. We find that the other two longer-time parameters G'_p and τ do not strongly depend on deviations in η_∞ needed to make $\eta_\infty(\phi)$ behave as a monotonically increasing function, which would be expected rheologically. Exploring the very early time corrections for both inertia and shape fluctuations that would be required to extract translational DWS self-motion MSDs of droplet-probes over a wide range of emulsion compositions represents an interesting direction for future studies.

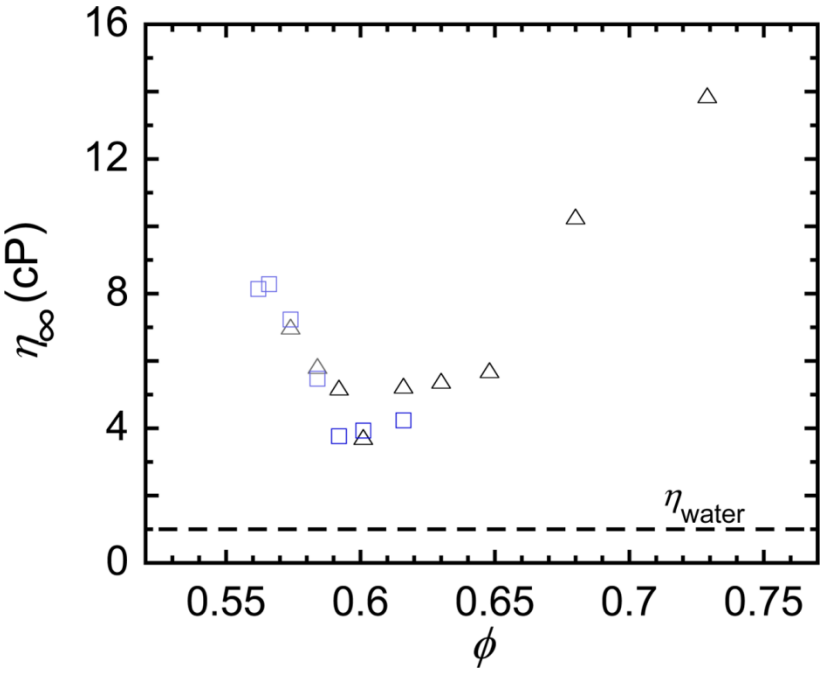

Figure 3.8. Volume fraction dependent high-frequency viscosity, η_∞, values for a = 459 nm jammed monodisperse emulsion determined from DWS-GSER. High-frequency viscosity, η_∞, found by fitting DWS self-motion MSDs (open triangles: transmission DWS; open squares: backscattering DWS) to the viscoelastic emulsion model given in equation (3.11) at droplet volume fractions, ϕ ranging from 0.562 to 0.729, for a fractionated and concentrated O/W emulsion having average radius a = 459 nm, stabilized using 10 mM SDS. For $\phi < 0.60$, symbols for η_∞ have been lightened to emphasize that inertial effects are likely influencing these values strongly. Dashed horizontal line represents the viscosity of water $\eta_\infty(\phi)$.

3.4 – Conclusions

Since the advent of passive microrheology, apparent DWS MSDs have been used in combination with the GSER to show trends in $G'_p(\phi)$ of dense glassy and jammed colloidal systems, including emulsions, yet until now a highly accurate quantitative match with macroscopic mechanical measurements has not been obtained over a wide range of ϕ. In past experiments, the lack of conversion of apparent MSDs into true self-motion MSDs has led to the introduction of various correction factors to rescale microrheological measurements into mechanical measurements as well as theoretical speculations about appropriateness of boundary conditions and other assumptions inherent in the GSER. Here, we have shown that invoking such *ad hoc* correction factors is unnecessary, and we have presented and demonstrated a well-defined empirical method for correcting DWS MSDs in dense, highly scattering systems using ϕ-dependent $\langle S(q) \rangle$ to account for collective scattering. Although the q^3 weighting inherent in DWS does favor self-motion in the extracted MSDs, such extracted MSDs still require significant ϕ-dependent corrections for collective scattering from probes at high densities, up to a factor of 4 or more, as we have demonstrated for jammed emulsions. The excellent agreement we find between $G'_p(\phi)$ measured using both modern DWS-GSER microrheology and mechanical rheometry implies that the GSER does work very well for dense emulsion systems if the DWS MSDs have been properly corrected for collective scattering. In addition, the microrheological $G'_p(\phi)$ matches the predicted $G'_p(\phi)$ of the EEI model as droplets become jammed, which enables us to identify that the GSER is applicable when both screened electrostatic repulsions and droplet interfacial deformations dominate $G'_p(\phi)$. Moreover, we have derived a time-domain equation for MSDs of droplets in dense emulsions, based on the GSER and a model that has an $s^{1/2}$-dependent

contribution to the linear viscoelasticity, and have used this equation to fit measured DWS self-motion MSDs, yielding excellent agreement. From these fits, we have determined the ϕ-dependent time scale τ associated with the $(s\tau)^{1/2}$ term in the viscoelastic model. In future theoretical investigations, it would be useful to determine quantitative predictions for $\tau(\phi)$ and the power-law scaling identified for $G'_p(\tau)$ that could be compared with our measurements. We also note that similar $s^{1/2}$-contributions to the linear viscoelastic shear modulus can arise from hydrodynamic interactions in dense suspensions of hard spheres[144], so the equations we have developed might also be applicable to these dense systems as well. These equations might also potentially apply to certain elastic polymer systems that are in a viscous solvent. We anticipate that broader application of the method we have demonstrated for correcting DWS MSDs of jammed emulsions with the ϕ-dependent $\langle S(q) \rangle$ could lead to improved quantitative accuracy of passive microrheology using the GSER in other dense colloidal soft materials that are highly scattering.

Chapter 4 – Diffusing Wave Microrheology of Attractive Disordered Monodisperse Emulsions

4.1 – Introduction

We apply DWS to explore the microrheological behavior of an attractive disordered monodisperse emulsion at droplet volume fractions ϕ near and somewhat below the volume fraction ϕ_{MRJ} associated with maximal random jamming of hard spheres. This emulsion is characterized by a secondary attractive interaction potential between droplets that has a controllable well depth yet also a strongly repulsive barrier compared to thermal energy k_BT at very short range (see Figure 4.1 inset), such that droplets do not come into contact with each other under entropic excitations and remain stable against coalescence. The depth of the secondary well can be controlled through the addition of a nanoscale depletion agent. Because droplets are smooth to the molecular scale, a convenient and suitable depletion agent consists of self-assembled surfactant micelles at higher surfactant concentrations than those that are necessary to stabilize droplets against coalescence. Thus, depending on the magnitude of the secondary attractive interaction, the droplets can flocculate, form clusters, or gel without any size evolution of droplet radius via coalescence. By contrast, droplets in a purely charge-screened repulsive system are repelled from each other at short range. Because this secondary attraction in the interaction potential can cause droplets to adhere and because such adhesion can also alter the emulsion's structure, the rheological properties between attractive and repulsive systems can highly differ.

Such depletion-induced attractive emulsion systems were first created and studied using mechanical rheometry by Mason *et al.*[15, 23, 32] and later by Datta *et al.*[23]. The monodisperse emulsion system that we investigate in this chapter is very similar in composition and in average droplet radius to the monodisperse emulsion system used by Mason *et al*. Each of these studies by Mason *et al*. and Datta *et al*. explored a different depletion-induced emulsion system at high ϕ yet below ϕ_{MRJ}, and both found a two-step yielding behavior, related to the presence of strong attractions between droplets that were many times thermal energy k_BT. Furthermore, large differences in the behavior of the ϕ-dependent plateau shear moduli, $G'_p(\phi)$, between repulsive and attractive emulsions were found. The comparison of $G'_p(\phi)$ between attractive versus repulsive emulsions showed that attractive emulsions can exhibit a dominant $G'_p(\phi)$ for ϕ □well below ϕ_{MRJ}. This effect of attraction was attributed to the formation of space-spanning networks of aggregated and gelled droplets which can support shear stress. By contrast, the repulsive microscale emulsions were marked by a sharp drop in $G'_p(\phi)$ for ϕ below ϕ_{MRJ}. While the consequences of a strong depletion attraction clearly confers to a dominant elastic plateau shear modulus down to significantly lower ϕ than for emulsions having hard or short-range repulsive interactions, the quantitative behavior of $G'_p(\phi)$ as a function of the magnitude of the attractive well depth U_{attr} is still not well characterized and understood for weaker attractions. A prior attempt has been made to investigate this[91], but the behavior could not be understood quantitatively due to the high droplet size polydispersity in the emulsion used in that study.

In this chapter, we present diffusing wave spectroscopy (DWS) microrheology measurements investigating the effect of the strength of the depletion attraction on the behavior of G'_p of monodisperse emulsion near and below ϕ associated with jamming of disordered hard spheres that have hard interactions. Given the advances in quantitative DWS of dense highly

scattering emulsions in Chapter 3, DWS might also be suitable for quantitatively studying attractive emulsions because no external perturbation, such as an imposed shear strain by a mechanical rheometer, might potentially cause alteration of the fragile aggregated structures of networks of droplet aggregates formed in certain attractive emulsions. This method, furthermore, is sensitive to probe displacements approaching 1 Å[110-114], is capable of providing rheological information at short time scales (*i.e.* high frequency) beyond traditional mechanical rheometers. Thus, diffusing wave microrheology can potentially reveal interesting information with regards to short time dynamics. In our experiments, as in previous chapters, we use sodium dodecyl sulfate (SDS) stabilized poly-dimethylsiloxane oil-in-water (O/W) emulsions; SDS micelles serve as depletion agents. The use of SDS micelles is also advantageous since we avoid introducing additional chemical compositional complexity, and since the magnitude of the depletion attraction $|U_{attr}|$ can be conveniently tuned by adjusting the SDS concentration. By adapting and extending the improved DWS analysis developed in Chapter 3 to these DWS measurements on attractive emulsions, we reveal interesting rheological in the light scattering signatures and microrheology of attractive emulsions that are not present in repulsive emulsions.

4.2 – Materials and Methods

4.2.1 – Monodisperse O/W Emulsion System

We recover the sodium dodecyl sulfate (SDS; Fisher Scientific; electrophoresis grade 99% purity) stabilized poly-dimethylsiloxane (PDMS; Gelest Inc.; viscosity 350 cSt) oil-in-water (O/W) monodisperse emulsions having a = 459 nm used in the non-destructive DWS microrheology study from Chapter 3. We prepare a 10 mM SDS solution using SDS and deionized water (Millipore Milli-Q; resistivity 18.2 MΩ·cm) to dilute the recovered emulsion to roughly $\phi \approx 0.15$ while simultaneously washing the emulsion to set [SDS] = 10 mM. This diluted

emulsion is then concentrated via centrifugation (Beckman L8-55 ultracentrifuge, 6 SW-28 swinging buckets of ≈ 30 mL capacity, 10k rpm, 1.25 h) into a dense elastic plug of cream at higher ϕ. We repeat the dilution and centrifugation steps for two more times to ensure that the surfactant concentration in the aqueous continuous phase is set at [SDS] = 10 mM. We combine the dense plugs of cream from the last centrifugation step and store the master concentration emulsion in a jar. This jar is then stored in a temperature controlled chamber (T = 20 °C) for later use; the constant temperature environment of this chamber prevents evaporation-condensation issues that can cause ϕ of this master sample to evolve and that normally occur if the jar of emulsion is stored on the lab bench without such control.

4.2.2 – Diffusing Wave Spectroscopy and Mechanical Rheometry: Varying ϕ at fixed [SDS]

We re-adjust the emulsion SDS concentration to 20 mM by repeatedly washing and centrifuging the recovered emulsion. We dilute the recovered emulsion with 20 mM SDS to volume fraction $\phi \sim 0.15$ and centrifuge the resultant dilution at 10k rpm for 1.25 h to higher ϕ to wash the emulsion to [SDS] = 20 mM. We repeat the washing procedure for a total of three times. We then combine the dense plugs from last centrifugation step to form a master monodisperse emulsion sample having [SDS] = 20 mM. This master emulsion is stored in a T = 20 °C controlled chamber. The average droplet radius in the master emulsion is verified by dynamic light scattering to be unchanged from prior studies that found a = 459 nm. We have characterized the droplet volume fraction of this master emulsion using a gravimetric evaporation method[99], yielding $\phi_{m,20mM} = 0.737$. From this particular master sample, we prepare samples of emulsions at different ϕ, near but below $\phi_{m,20mM}$ by diluting this master emulsion sample with a 20 mM SDS solution using an analytical balance (Denver Instruments APX-200, 0.1 mg precision). The resulting ϕ of each different sample can be calculated from these

measured masses using measured densities of the SDS solution and of the PDMS[99]. We perform DWS and mechanical rheometry on the prepared samples to characterize this emulsion's rheological properties. The measurements are conducted using similar conditions described in sections 3.2.2 and 3.2.3. We perform mechanical rheometry (Rheometrics RFS II) using a frequency sweep with a peak shear strain of $\gamma = 0.005$. We also perform DWS (Rheolab III, LS Instruments) using 5 mm pathlength glass sample cuvettes with a correlation run time of 300 s and an echo setting of 60 s.

4.2.3 – Diffusing Wave Spectroscopy and Mechanical Rheometry: Varying [SDS] at fixed ϕ

We re-use and readjust emulsions used in section 4.2.2 to [SDS] = 10 mM by following procedures described in 4.2.1. We characterize the droplet volume fraction of this new master emulsion set at 10 mM SDS using a gravimetric evaporation method[99] and find $\phi_{m,10mM} = 0.737 \pm 0.006$. We prepare emulsion samples to have a nearly fixed ϕ, but different final SDS concentration, by diluting the 10 mM SDS master emulsion with different aqueous SDS solutions having a range of SDS concentrations. The mass of the added SDS solution and the mass of the master emulsion used to prepare each of the samples are measured using an analytical balance. From these recorded masses, we calculate the resulting ϕ of each different sample using the measured mass densities of the SDS solution and of the PDMS[99]. We explore two ϕ values that are near but below the jamming limit of hard spheres: $\phi = 0.584$ and $\phi = 0.592$.

We perform DWS measurements and mechanical rheometry to characterize the microscopic dynamics of droplets in these attractive emulsions as well as their macroscopic rheological properties. The measurements are conducted using similar conditions described in section 4.2.2. For $\phi = 0.584$, we perform mechanical rheometry (Rheometrics RFS II) using a frequency sweep with a peak shear strain of $\gamma = 0.005$, and we use DWS (Rheolab III, LS

Instruments) with a correlation run time of 100 s and an echo setting of 60 s. For ϕ = 0.592, DWS measurements are made using same procedures; no mechanical rheometry have been taken.

4.3 – Results and Discussion

4.3.1 – Behavior of Attractive Emulsions: Varying ϕ at Fixed [SDS]

We perform DWS measurements of attractive PDMS O/W emulsions at [SDS] = 20 mM to investigate the effect of weak depletion attractions in concentrated monodisperse emulsions having average droplet radius a = 459 nm. We estimate the magnitude of the depletion attraction, $|U_{attr}|$, using a formula derived in a prior work[32]:

$$|U_{attr}| = 4\pi a^3 C_m N_0 k_B T (a_m/a)^2, \quad (4.1)$$

where C_m is the concentration of micelles, N_0 is Avogadro's number, k_B is Boltzmann's constant, T is the temperature, and a_m is the radius of an SDS micelle. Since an SDS micelle, which has a_m = 2 nm, is composed of $v_m \approx 70$ dodecyl sulfate monomers, we can relate the micelle concentration C_m to [SDS] by:

$$C_m = \frac{[SDS] - C^*}{v_m}, \quad (4.2)$$

where the critical micelle concentration of SDS is $C^* \approx 8.1$ mM. We calculate $|U_{attr}|$ for emulsions having a = 459 nm as a function of [SDS], shown in Figure 4.1. For these emulsions washed at [SDS] = 20 mM, we calculate $|U_{attr}| \approx 2.4\ k_B T$. While the primary effect of raising [SDS] is to induce a depletion attraction that can cause droplets to form attractive networks, a secondary effect, reducing the Debye screening length through higher overall ionic content in the continuous phase, is also expected. With both of these potential effects in mind, we have

explored attractive emulsions at fixed [SDS] = 20 mM for $0.573 \leq \phi \leq 0.647$ near yet below hard-sphere jamming.

In Figure 4.2, we present the measured average normalized intensity correlation functions, $g_2(t)$ - 1, of the emulsions having fixed [SDS] = 20 mM. Beyond the features in the repulsive emulsion's $g_2(t)$ - 1 curves (see Figure 3.3), the weakly attractive emulsion's $g_2(t)$ - 1 exhibits an additional decay to a plateau at long times, as seen in both transmission and backscattering configurations (see Figure 4.2). This additional decay is much more accentuated in the transmission signal. This deviation from a simple decay to a plateau to what appears to be a two-step decay to a final long-time plateau is weak for ϕ towards the hard-sphere jamming limit at ϕ

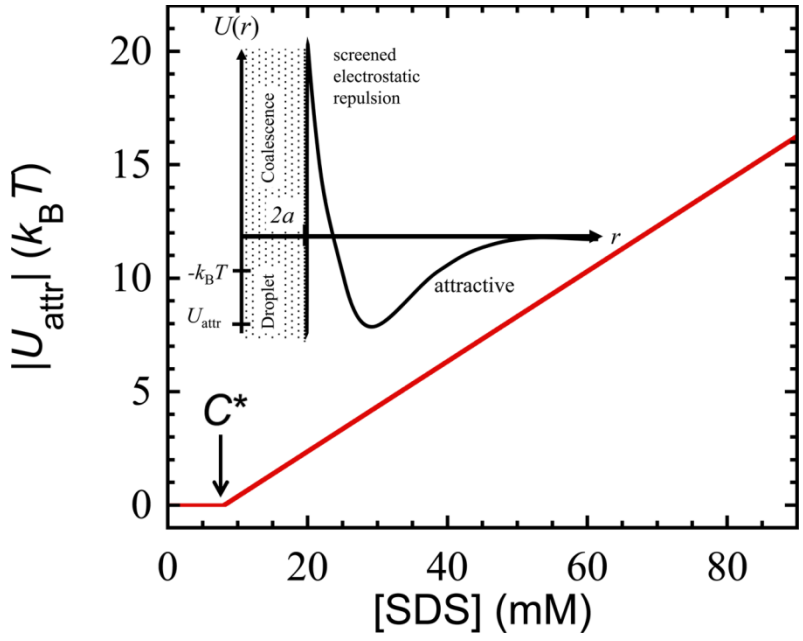

Figure 4.1. Estimated magnitude of the potential energy at contact between two droplets caused by a micellar depletion attraction as a function of SDS concentration. The magnitude of the depletion attraction, $|U_{attr}|$, caused by SDS micelles, present for [SDS] > C^*, where C^* is the critical micelle concentration, is given in equation (4.1). Red solid line: $|U_{attr}|$ (in units of thermal energy k_BT) for droplets having average radius a = 459 nm. Inset: idealized sketch of the droplet pair interaction potential $U(r)$ as a function of center-to-center separation between the droplets. The secondary attractive well, caused by depletion, has a well-depth $|U_{attr}|$. At slightly smaller separation r, there is a repulsive barrier, created by stabilizing surfactant. For even smaller r, the primary attractive well associated with van der Waals interactions dominates, and these attractions would cause droplet coalescence.

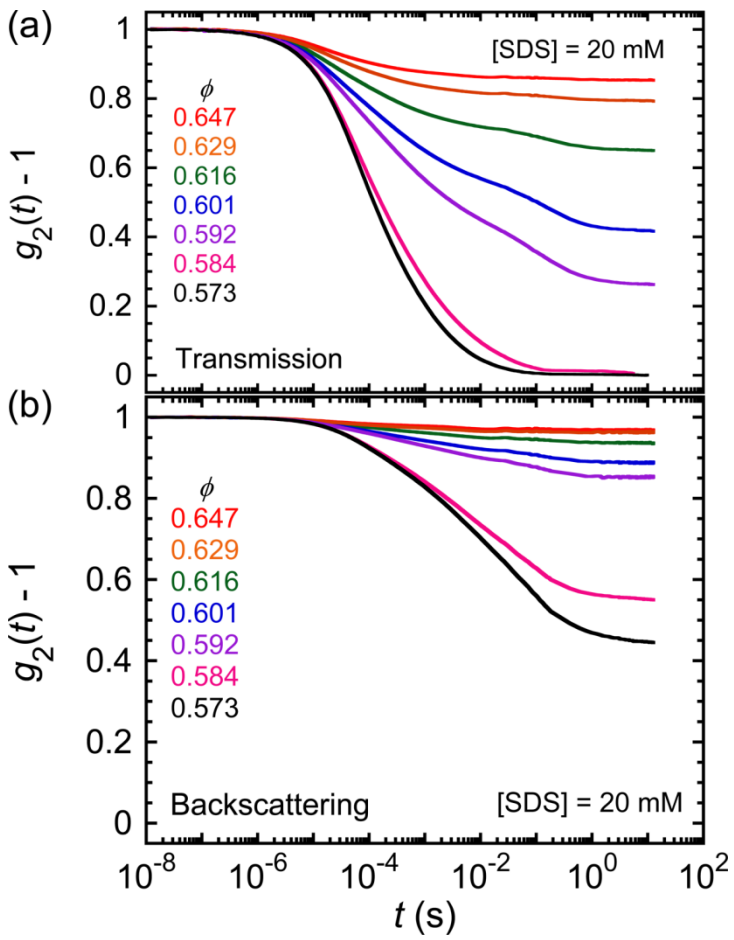

Figure 4.2. Averaged normalized DWS intensity autocorrelation functions, $g_2(t)$ - 1, of attractive emulsions at fixed [SDS] = 20 mM. Emulsions having radius a = 459 nm with varying ϕ (listed on left; top to bottom) are measured using DWS at a temperature T = 20 °C: (a) transmission and (b) backscattering geometries. The $g_2(t)$ – 1 signals are averaged over 10 individual runs. The transmission $g_2(t)$ - 1 for ϕ = 0.584 have been smoothed out with an interpolated fit through original data to more smoothly connect correlation and echo measurements. The measurements are made 10 days after the sample preparation, except for the ϕ = 0.573 sample, which was measured 1 day after sample preparation.

≈ 0.64, but then becomes progressively accentuated towards lower ϕ. Interestingly, the time scales over which this additional decay occurs are around 10^{-2} s $\lesssim t \lesssim 10^{-1}$ s, independent of ϕ.

We then attempt to extract the measured true self-motion mean square displacements, $\langle \Delta r^2(t) \rangle$, of the depletion-induced attractive emulsion droplets to investigate further how DWS response of attractive emulsions differs from that of repulsive emulsions. Although the

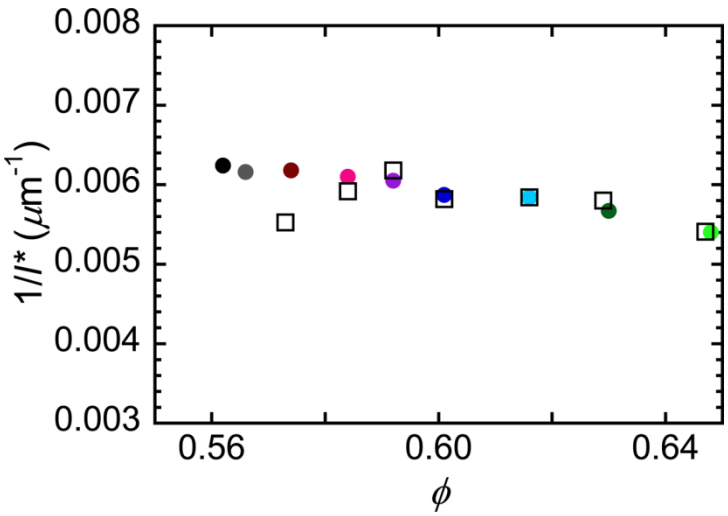

Figure 4.3. Inverse optical transport mean free path as a function of ϕ for depletion-induced attractive emulsions. Open squares: measured $1/\ell^*$ for PDMS O/W emulsions (average radius a = 459 nm) that have been washed to set [SDS] = 20 mM. Colored circles (see Figure 3.4(a) for color designations): measured $1/\ell^*$ for the same PDMS O/W emulsions that have been washed to set [SDS] = 10 mM.

emulsions experience weak depletion attractions, we assume here that the collective scattering effects present in DWS intensity correlation function $g_2(t) - 1$ can still be corrected in the same manner as that of repulsive emulsions as discussed in Chapter 3. We use the measured inverse optical transport mean free path $1/\ell^*$ (open squares, Figure 4.3) to calculate the average structure factor $\langle S(q) \rangle$ and thereby correct for collective scattering effects. The measured $1/\ell^*$ for depletion-induced attractive emulsions compare well to the measured $1/\ell^*$ determined for the repulsive case (circles, Figure 4.3) within the measurement error of the DWS instrument. Moreover, at [SDS] = 20 mM, the micellar depletion only induces inter-droplet attractions of $|U_{attr}| \approx 2.4\ k_B T$, that are somewhat larger than thermal energy. Thus, we assume the method of correcting for collective scattering effects at this SDS concentration is reasonable. Using the improved DWS analysis outlined in sections 3.3.3 - 3.3.4, we obtain the mean square displacements, $\langle \Delta r^2(t) \rangle$, corrected for collective scattering effects, from the DWS measurements using transmission and backscattering geometries as shown in Figures 4.4 and 4.5 respectively.

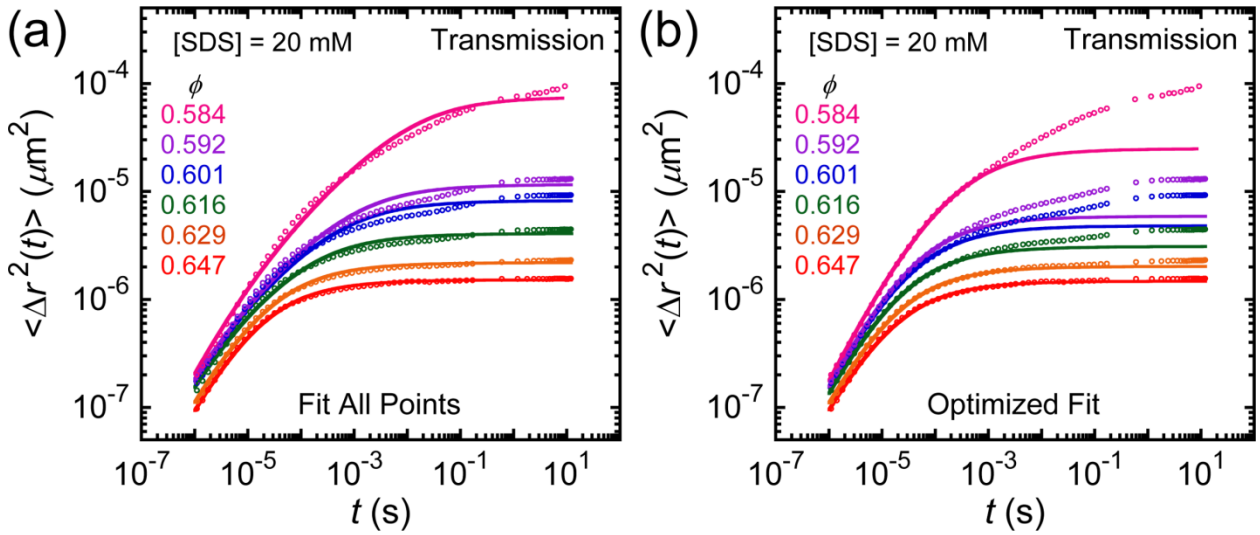

Figure 4.4. Transmission mean square displacements $\langle \Delta r^2(t) \rangle$ measured by DWS of attractive emulsions at different ϕ and fixed [SDS] = 20 mM. The mean square displacements $\langle \Delta r^2(t) \rangle$ (circles; displayed every 1 in 3 data points for clarity), measured in transmission DWS, are fitted to the time-domain MSD function for the repulsive emulsions, given in equation (3.11) through: (a) all points and (b) a partial set of early time $\langle \Delta r^2(t) \rangle$ to yield an early-time optimized fit. The fits are shown as lines. The droplet volume fractions ϕ are listed for curves from top to bottom. The optimized early-time fit parameters are described in Table 4.1.

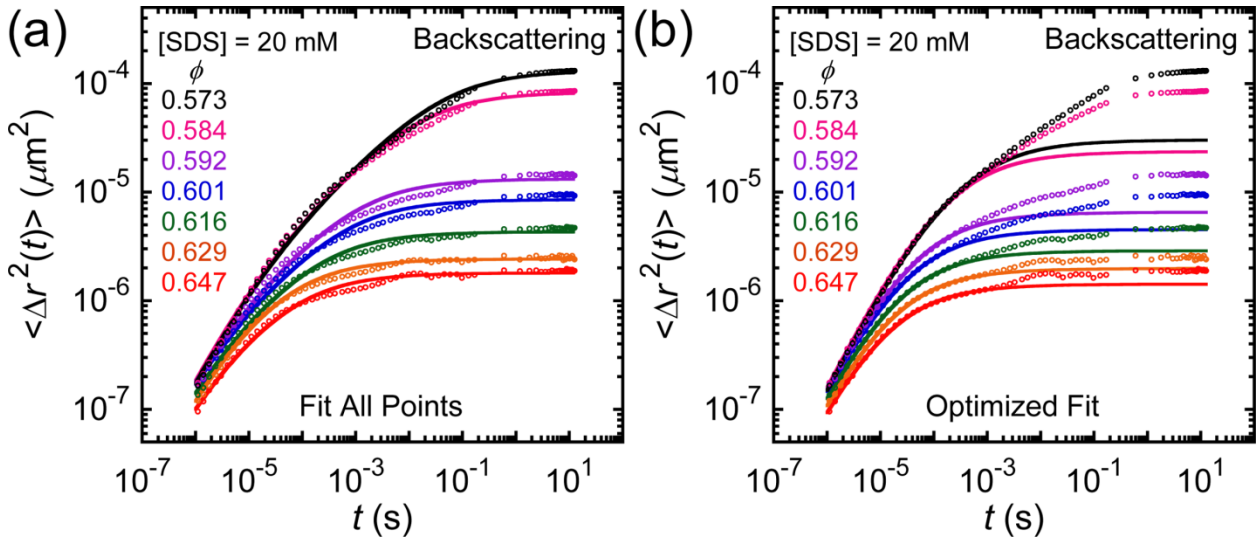

Figure 4.5. Backscattering mean square displacements $\langle \Delta r^2(t) \rangle$ measured by DWS of attractive emulsions at different ϕ and fixed [SDS] = 20 mM. The mean square displacements $\langle \Delta r^2(t) \rangle$ (circles; displayed every 1 in 3 data points for clarity), measured in backscattering DWS, are fitted to the time-domain MSD function for the repulsive emulsions, given in equation (3.11) through (a) all points and (b) a partial set of early time $\langle \Delta r^2(t) \rangle$ for an early-time optimized fit. The fits are shown as lines. The droplet volume fraction ϕ are listed for curves from top to bottom. The optimized early-time fit parameters are described in Table 4.1.

Inspection of the corrected MSDs, $\langle \Delta r^2(t) \rangle$, reveals a slight upward trend in the mean-square displacement near intermediate times ($t \sim 10^{-2}$ s), which correspond to the observed additional decay in the $g_2(t)$ - 1 signals. Moreover, a final long-time plateau is observed for $t > 10^{-1}$ s, mostly in the echo region.

We analyze the more complex $\langle \Delta r^2(t) \rangle$ of attractive emulsions to quantify how the depletion attraction caused by the additional micelles at [SDS] = 20 mM impact the DWS results, as compared to repulsive emulsions. We first try fitting the $\langle \Delta r^2(t) \rangle$ to the time-dependent MSD for repulsive emulsion determined in equation (3.11) through all points determined by transmission and backscattering DWS, as shown in Figures 4.4(a) and 4.5(a). Upon comparison, we find that this fitting procedure yields poor results, and there are large systematic deviations of the measurements from the fitted lines. The deviations from the fit become more pronounced as ϕ decreases away from jamming to lower ϕ. There is an excess decay in the correlation decay of these attractive emulsions at long times compared to repulsive emulsions, and this excess decay for the attractive emulsions also leads to long-time excesses in the MSDs caused by additional droplet dynamics that are not present in the repulsive emulsions.

We hypothesize that only a portion of the dynamics seen in the attractive emulsions relates to droplets in space-filling networks that can support macroscopic shear stress; the excess dynamics at long times relates to Brownian excitations of clusters of droplets that are dangling and not well integrated into the primary shear-stress-bearing networks of droplets. Furthermore, we hypothesize that the non-excess portion of the MSDs at early times in these attractive systems can be described by the same equations as for repulsive emulsions. To test these hypotheses, we optimize the fits to the early-time data for $\langle \Delta r^2(t) \rangle$, as shown in Figures 4.4(b) and 4.5(b). To fit, we use equation (3.11) yet restrict the range of the fit to early time points, which correspond to

short and intermediate time scales, before the additional decay observed in $g_2(t)$ - 1. During the early-time fit optimization process, we have found very small oscillating signal present at early times, likely resulting from slight mechanical vibrations and resonances in the DWS instrument, which makes optimization of the fit through minimization of residuals less precise. Despite these minor oscillations, we restrict our early time fit range such that the oscillating residual signals are minimized in magnitude and only positive residuals result beyond the fitted time range.

By restricting and optimizing these fits to early and intermediate times, we capture the average single droplet MSD contributions well there; moreover, at longer times, we begin to reveal additional features in the DWS signal that arise from Brownian excitations of collections of attractive droplets as a consequence of the imposed micellar depletion effect. As shown in Figures 4.4(b) and 4.5(b), we find the measured $\langle \Delta r^2(t) \rangle$ at long times are always higher in magnitude than the early-time optimized fit. This additional MSD signal likely arises from thermal-entropic excitations of clusters and dangling ends of the gel networks formed in attractive emulsions. Unlike repulsive emulsions, in which all droplets are equally likely to contribute to an elastic response to an imposed shear stress, only a fraction of droplets in attractive emulsions are well incorporated into space-spanning, shear-stress-bearing gel networks. Other droplets, which are not part of these networks, can form clusters and become loosely attached to the struts of the shear-stress-bearing gel networks. The vibrational motion of these weak, loosely attached clusters would cause an additional decay in $g_2(t)$ - 1 and thereby provide an additional excess contribution to the mean-square displacement.

We quantify this additional signal in MSD that appears at longer times by calculating the differences between the DWS $\langle \Delta r^2(t) \rangle$ and the early-time optimized fit MSD, $\langle \Delta r^2(t) \rangle_{\text{fit}}$. While recognizing that these excess fluctuations at longer times should not necessarily be interpreted as

single droplet motion, we define an excess MSD function as: $\langle \Delta r^2(t) \rangle_{xs} = \langle \Delta r^2(t) \rangle - \langle \Delta r^2(t) \rangle_{fit}$. We show the measured $\langle \Delta r^2(t) \rangle_{xs}$ in Figure 4.6. From Figure 4.6, we find $\langle \Delta r^2(t) \rangle_{xs}$ is largest for the lowest ϕ explored at long times and rapidly decreases almost 3 orders in magnitude as ϕ approaches ϕ_{MRJ}. This trend is consistent with the notion that droplets would be much more confined with less space to move in void regions at higher ϕ, such that dynamics of dangling clusters would be restricted.

We can further quantify the behavior by fitting this $\langle \Delta r^2(t) \rangle_{xs}$ using an empirical equation, motivated in part by the harmonically bound Brownian particle (HBBP). We create a new fitting function that for simplicity we call a modified bound Brownian particle (MBBP):

$$\langle \Delta r^2(t) \rangle_{xs} = \langle \Delta r^2 \rangle_{xs,p} \{1 - \exp[(-t/t_D)^{\beta}]\}, \qquad (4.3)$$

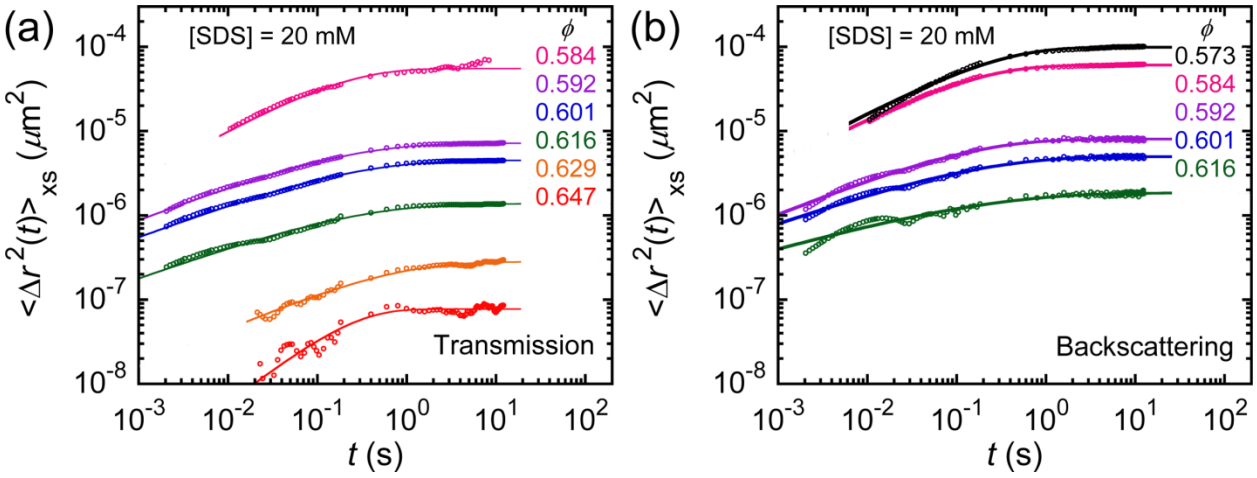

Figure 4.6. Excess mean square displacements $\langle \Delta r^2(t) \rangle_{xs}$ as a function of ϕ for fixed [SDS] = 20 mM. The temporal excess MSD signal $\langle \Delta r^2(t) \rangle_{xs}$, for a = 459 nm emulsions are determined by taking the difference between the measured MSD and the early-time optimize fits to equation (3.11), shown in Figures 4.4(b) and 4.5(b). The excess MSDs are determined for: (a) transmission and (b) backscattering DWS geometries. The droplet volume fractions ϕ are listed on the right for data shown (top to bottom). All sets of data have been fit to an equation describing a modified bound Brownian particle (MBBP): $\langle \Delta r^2(t) \rangle_{xs} = \langle \Delta r^2 \rangle_{xs,p} \{1 - \exp[-(t/t_D)^{\beta}]\}$. The fit parameters are given in Table 4.2.

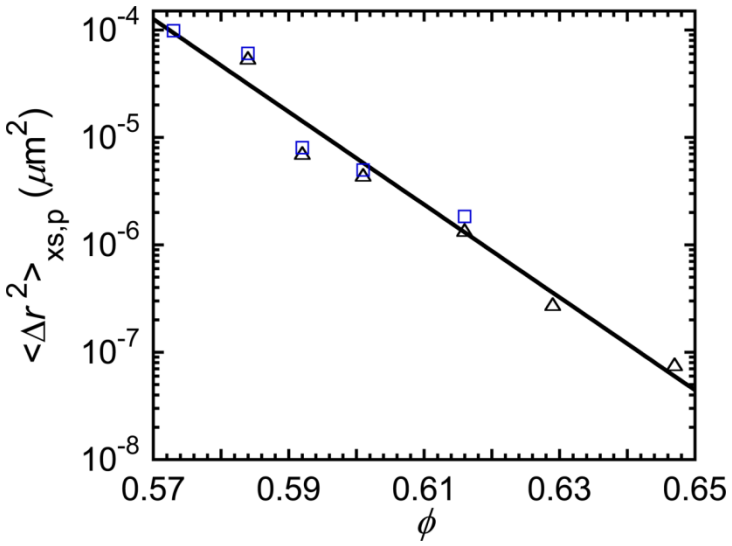

Figure 4.7. Plateau excess mean square displacements $\langle \Delta r^2 \rangle_{xs,p}$ as a function of ϕ for fixed [SDS] = 20 mM. The determined fit parameter $\langle \Delta r^2 \rangle_{xs,p}$ for a = 459 nm emulsions are plotted as a function of volume fraction ϕ. Transmission: black triangles. Backscattering: blue squares. Empirically, the ϕ-dependence of $\langle \Delta r^2 \rangle_{xs,p}$ can be described by an exponential decay function: $\langle \Delta r^2 \rangle_{xs,p} = A_{xs,p} \exp[-(\phi - \phi_{MRJ})/(\Delta\phi_{xs,p})]$, where $\phi_{MRJ} \approx 0.646$ and determined fit parameters are $A_{xs,p} = (6.6 \pm 2.1) \times 10^{-8}$ μm^2 and $\Delta\phi_{xs,p} = (1.01 \pm 0.06) \times 10^{-2}$.

where $\langle \Delta r^2 \rangle_{xs,p}$ describes the maximum plateau MSD of the Brownian object, t_D is the time scale associated with diffusion, and β is the exponent which describes the sub-diffusive power-law rise to a long-time plateau MSD when $\beta < 1$. In the limit $\beta = 1$, the more general MBBP becomes the simpler HBBP. If $\beta < 1$, it indicates that Brownian objects contributing to the excess MSD signal are not freely diffusing, which would be consistent for loose dangling clusters of droplets trapped within the main stress-bearing gel network of droplets. The results of the fits to $\langle \Delta r^2(t) \rangle_{xs}$ are described in Table 4.2. In general, we observe that $\beta < 1$ (average β = 0.46 ± 0.09 for ϕ points below $\phi_{MRJ} \approx 0.646$), which provides further support that this excess signal arises from sub-diffusion processes. Furthermore, we notice that β decreases as ϕ increases, except at the highest $\phi = 0.647$ which shows a much significantly higher β, although there is much less excess MSD signal at this particular ϕ, so this change in the behavior of β is

less certain. We also note that the plateau fit parameter $\langle \Delta r^2 \rangle_{xs,p}$ increases as ϕ decreases below ϕ_{MRJ}, as seen in Figure 4.7. This is consistent with the notion that there is more available 'void' space for loosely bound dangling clusters of droplets to move in less dense void regions in attractive emulsions as ϕ is reduced below the jamming point. We find empirically that this observed ϕ-dependence of $\langle \Delta r^2 \rangle_{xs,p}$ can be well described by an exponential decay function: $\langle \Delta r^2 \rangle_{xs,p} = A_{xs,p} \exp[-(\phi - \phi_{MRJ})/\Delta\phi_{xs,p}]$, where ϕ_{MRJ} is fixed to be 0.646 (see Figure 4.7). From the fit, we determine the fit parameters: $A_{xs,p} = (6.6 \pm 2.1) \times 10^{-8}$ μm^2 and $\Delta\phi_{xs,p} = (1.01 \pm 0.06) \times 10^{-2}$. Lastly, we note that $t_D \approx 0.1$ s for all ϕ points explored at [SDS] = 20 mM; this result from fitting the excess MSD signal is directly connected to the observation that the secondary decays in $g_2(t) - 1$ all occur for 10^{-2} s $\lesssim t \lesssim 10^{-1}$ s.

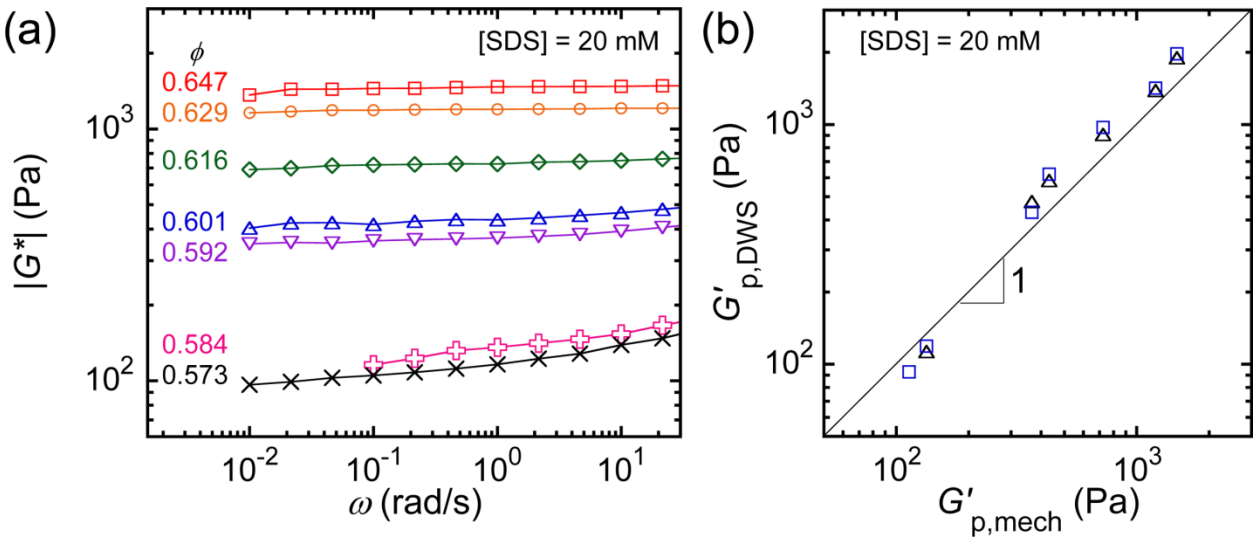

Figure 4.8. Mechanical measurements and comparison of plateau shear elastic moduli G'_p. (a) Mechanically measured magnitude of the complex shear modulus $|G^*(\omega)|$ (squares, lines guide the eye) as a function of frequency ω at droplet volume fractions, ϕ ranging from 0.729 to 0.573 (top to bottom) from a oscillatory test with a fixed peak shear strain of $\gamma = 0.005$ is shown. Measured values of the shear elastic storage modulus G' (not shown) are almost equal to $|G^*(\omega)|$ over the frequency range explored. (b) $G'_{p,mech}$ values are extracted from the frequency sweep at ω = 1 rad/s and compared against $G'_{p,DWS}$ values, obtained from the G'_p parameter from the early-time optimized fit of equation (3.11) shown in Figures 4.4 and 4.5. DWS transmission: (black triangles). DWS backscattering: (blue squares). The diagonal solid line indicates a 1-to-1 match between $G'_{p,mech}$ and $G'_{p,DWS}$.

We also compare the DWS early-time optimal fit G'_p values to the mechanically measured values of G'_p, as shown in Figure 4.8. The mechanical frequency sweeps of the same exact samples, taken immediately after the DWS measurements shown, are plotted in Figure 4.8(a). For 10^{-1} rad/s $\leq \omega \leq 10^2$ rad/s, the mechanical frequency sweeps display relatively flat plateau values of $|G^*(\omega)|$ which are mostly dominated by the linear shear elastic storage modulus G'. We select the mechanically measured value of G' at $\omega = 1$ rad/s and label it as $G'_{p,mech}$. This value is compared against the early-time optimal fit G'_p parameter values, denoted as $G'_{p,DWS}$ in Figure 4.8(b). Within the run-to-run uncertainties of both mechanical and DWS measurements, the values of G'_p obtained by using the two different techniques lie reasonably close to the 1-to-1 line, implying that removing the additional long-time decay associated with dangling clusters and the excess MSD signal is appropriate in order to make a valid microrheological interpretation of these attractive emulsions that quantitatively connects with macroscopic rheometry. The deviation for the lower values of $G'_p \sim 100$ Pa, which correspond to $\phi = 0.573$ and $\phi = 0.583$, may be explained by the sensitivity of G'_p in this ϕ range for the repulsive emulsions as shown in Figure 3.2(b). For the larger $G'_{p,DWS}$ data points (*i.e.* higher ϕ points) where G'_p is not as sensitive, $G'_{p,DWS}$ appears to be only 10% higher than $G'_{p,mech}$; however, this small departure from the 1-to-1 line could be due to the difference between time of sample handling and the time when the sample was measured in the two measurements. The DWS measurements were taken after 10 days after significant sample handling while the corresponding mechanical measurements only used 5 minutes of wait time after loading the sample and applying the pre-shear. This disparity of the time scales may have slightly biased the measurements towards a certain direction since the attractive systems could be dependent on the sample handling procedures such as aging. Nevertheless, reasonable agreement between $G'_{p,DWS}$

and $G'_{p,mech}$ provides reasonable support for our approach of using the early-time optimized fits to extract the MSDs of the droplets involving stress supporting network while revealing additional MSD signals that may be related to other dynamics within the network that do not directly influence the macroscopic rheology of these attractive emulsions.

4.3.2 – Depletion-Induced Attractive Emulsions: Varying Attraction Strengths at Fixed ϕ

To investigate the effect of the SDS depletion attraction strengths on highly concentrated emulsions, we perform DWS measurements on concentrated emulsions which are set to a constant ϕ but diluted with different concentrations of SDS solutions. We explore the effect of SDS concentration at two volume fractions: ϕ = 0.584 and ϕ = 0.592. Without any depletion effects, these ϕ values lie within the electrostatically jammed regime or lie near the boundary of the electrostatic and interfacially jammed regimes predicted by the EEI model. The measured average normalized intensity correlation functions g_2(t) - 1 are shown at different concentrations for ϕ = 0.584 and ϕ = 0.592 in Figures 4.9 and 4.10, respectively, and their respective measured optical mean free paths ℓ^* as a function of [SDS] are also presented (see Figure 4.11). In the following sections, we discuss the results at each of the two fixed ϕ values individually.

4.3.2.1 – Depletion-Induced Attractive Emulsions: Varying [SDS] at Fixed ϕ = 0.584

The measured $g_2(t)$ - 1 curves for ϕ = 0.584 at various SDS concentrations are shown in Figure 4.9. Starting from the repulsive emulsions at [SDS] = 10.0 mM, we notice that there is a non-zero long-time plateau value of $g_2(t)$ - 1 for both transmission and backscattering geometries. Upon increasing the SDS concentration to 20.0 mM, the non-zero long-time $g_2(t)$ - 1 signal disappears for the same measurement conditions used. On the surface, this might be interpreted to indicate that the emulsion at 20.0 mM SDS displays a significantly weaker elasticity than emulsions at 10.0 mM SDS. This type of behavior could be similar to adding ionic salt, such as

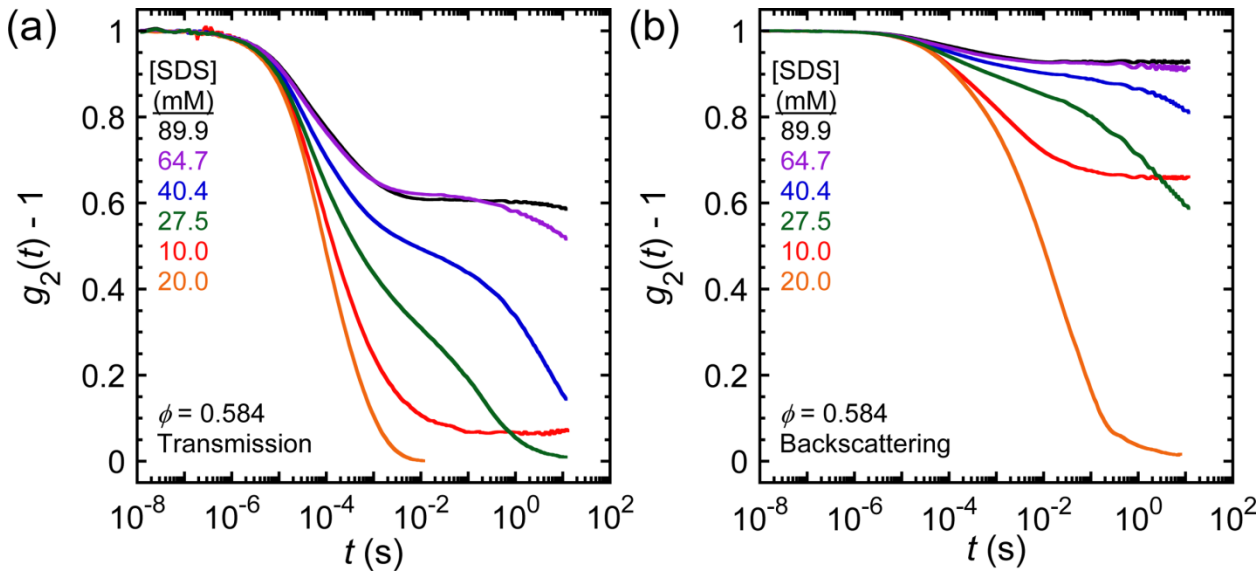

Figure 4.9. Averaged normalized intensity autocorrelation functions, $g_2(t)$ - 1, for different [SDS] of attractive emulsions at ϕ = 0.584. The $g_2(t)$ - 1 signals (lines) are measured for a = 459 nm emulsions by DWS (a) transmission and (b) backscattering geometry using 5 mm optical cuvettes at temperature T = 20 °C, 1 day after the sample preparation. The emulsions are diluted to different final [SDS] as listed on the left for correspondingly colored curves. The long time transmission $g_2(t)$ - 1 data for 20 mM SDS was unreliable and have been truncated to short times.

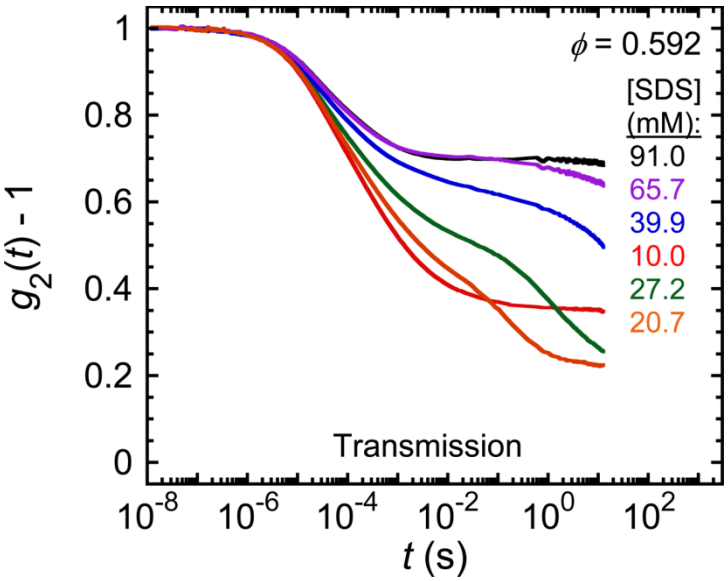

Figure 4.10. Averaged normalized intensity autocorrelation functions, $g_2(t)$ - 1, for different [SDS] of attractive emulsions at ϕ = 0.592. The $g_2(t)$ - 1 signals (lines) are measured for a = 459 nm emulsions by DWS transmission geometry using 5 mm optical cuvettes at temperature T = 20 °C, 1 day after the sample preparation. The emulsions are diluted to different final [SDS] as listed on the right, color-coded to the curves.

NaCl, which decreases the effective Debye screening length, such that the emulsion's elasticity could be lowered due to the decreased range of repulsive interactions. More interestingly, we observe that the $g_2(t) - 1$ signals from 20.0 mM SDS here are significantly different from $g_2(t)$ - 1 signals obtained from emulsions prepared in a different manner to the same ϕ and [SDS] (see section 4.3.1). This observed difference in $g_2(t)$ - 1 for what appears to be similar compositions suggests that the different routes of preparing and handling these attractive emulsions can potentially significantly affect DWS correlation functions.

As we increase [SDS] further, we notice interesting and non-monotonic trends in the values of the measured $g_2(t)$ - 1 at longer times in both transmission and backscattering DWS configurations, as shown in Figure 4.9. For attractive emulsions having [SDS] > 20.0 mM, we observe the reappearance of a non-zero long-time $g_2(t)$ - 1 value again, starting at [SDS] = 27.5 mM (*i.e.* $|U_{attr}| \approx 3.9\ k_BT$). This indicates that the emulsion system is becoming more strongly elastic, which is likely due to the formation of networks of gelled droplets resulting from the increased attraction strength. The long-time $g_2(t)$ - 1 values continue to rise up to [SDS] = 89.9 mM (*i.e.* $|U_{attr}| \approx 16.2\ k_BT$), indicating that these attractive emulsions are becoming more strongly elastic as the attractive depletion interactions between droplets are increased.

We also observe, at intermediate times ($t \sim 10^{-2}$ s), the appearance of a two-step decay signal to a final non-zero long-time plateau, which we had identified in previously in section 4.3.1. We had attributed this signal to dynamics of loose dangling clusters of droplets that are not well incorporated into the shear-stress-bearing regions of the main gel networks of droplets. As we increase [SDS] to induce stronger attractions, we find that this two-step decay to a non-zero plateau becomes more complicated and difficult to interpret. The time scales associated with the

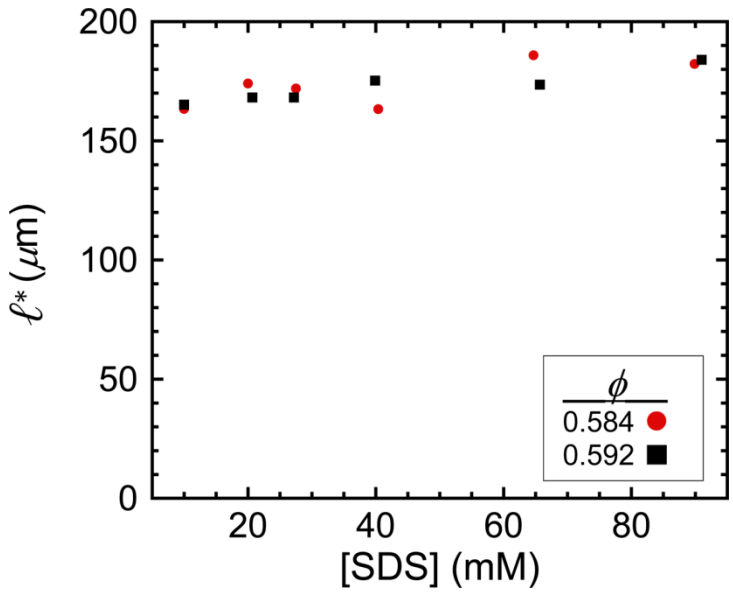

Figure 4.11. Measured [SDS]-dependent mean optical transport mean free paths ℓ^* at fixed $\phi = 0.584$ and $\phi = 0.592$. The values of ℓ^* for $\phi = 0.584$ (red circle) and $\phi = 0.592$ (black square) correspond to the set of DWS measured $g_2(t)$ -1 data shown in Figures 4.9 and 4.10.

second decay signal are seen to shift towards longer times with increasing [SDS], and sometimes the long-time plateau is not seen.

Using the measured ℓ^* values, shown in Figure 4.11, we obtain the mean square displacements, $\langle \Delta r^2(t) \rangle$, corrected for collective scattering via the average structure factor $\langle S(q) \rangle$, as shown in Figure 4.12. The values of ℓ^* are at most slightly increasing as [SDS] increases and this trend may be related to the aggregated structures that are formed in the gel networks of droplets. We first try fitting these $\langle \Delta r^2(t) \rangle$ to the time-dependent MSD function for repulsive emulsions, given by equation (3.11), and we find that this equation fits measured $\langle \Delta r^2(t) \rangle$ well over all measured time ranges for the repulsive emulsion at [SDS] = 10 mM as expected. Surprisingly, we find that the temporal MSD function also describes our $\langle \Delta r^2(t) \rangle$ data well for emulsions at [SDS] = 89.9 mM (*i.e.* $|U_{attr}| \approx 16.2\ k_B T$) over all measured t. These fits can be seen in Figure 4.12. The surprisingly good agreement at [SDS] = 89.9 mM is interesting since it

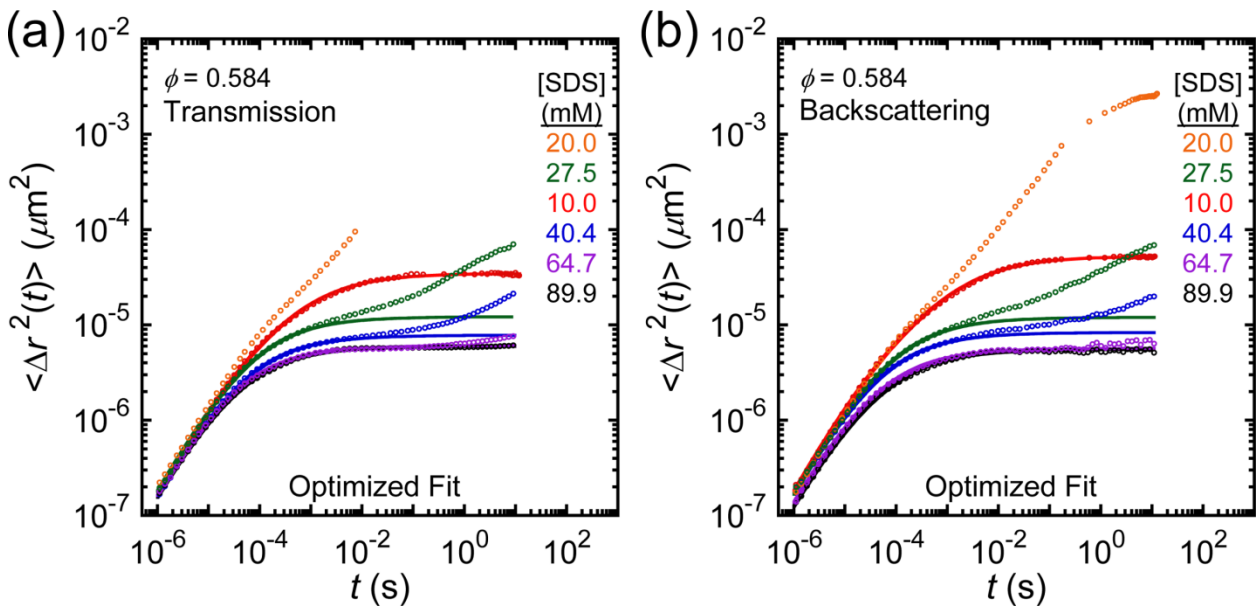

Figure 4.12. Measured mean square displacements $\langle \Delta r^2(t) \rangle$ and early-time optimized fits at $\phi = 0.584$. The mean square displacements $\langle \Delta r^2(t) \rangle$ (circles; displayed every 1 in 3 data points for clarity) are determined through (a) transmission and (b) backscattering DWS geometries. The $\langle \Delta r^2(t) \rangle$ values are optimized to fit early-time MSDs using equation (3.11). The fits are shown as line. The fits for [SDS] = 10.0 mM transmission and both [SDS] = 89.9 mM transmission and backscattering match the data well and no excess MSD can be readily detected. The [SDS] associated to each set of $\langle \Delta r^2(t) \rangle$ are listed (see right, color-coded to the data and fits). The optimized early-time fit parameters are described in Table 4.3.

suggests that $\langle \Delta r^2(t) \rangle$ signals purely arise from droplets within macroscopic stress supporting networks and that what would otherwise have been loose clusters are effectively incorporated by the very strong attraction into the main stress-bearing struts of these gel networks. There are no measurable dynamics associated with dangling clusters because they do not influence $\langle \Delta r^2(t) \rangle$ values over the time scale explored, as shown in Figure 4.12. This observation may indicate that the droplets are so strongly attracted that even the dangling clusters, which are responsible for the additional MSD signal, are attracted to the network and cannot be thermally excited. This causes a decrease in the population of mobile clusters, and it also arrests the dynamics of these clusters to time scales beyond those explored in our DWS measurements. For other sets of data at intermediate [SDS] = 27.5, 40.4, and 64.7 mM, the quality of fit of all data using equation

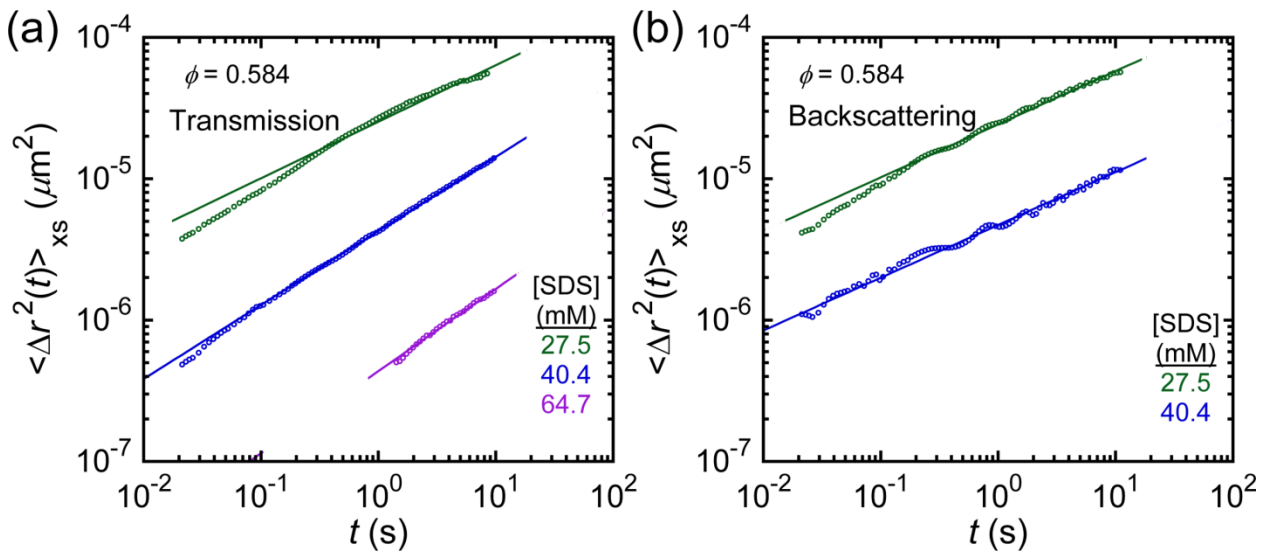

Figure 4.13. Excess mean square displacements $\langle \Delta r^2(t) \rangle_{xs}$ for different [SDS] at ϕ = 0.584. The calculated excess MSDs $\langle \Delta r^2(t) \rangle_{xs}$ (circles), are determined at different [SDS] for: (a) transmission and (b) backscattering DWS measurements. Data (backscattering, [SDS] = 64.7 mM) are excluded due to noisy background signal from mechanical vibrations. The corresponding [SDS] are listed (see legend, color-coded to data and fits). All sets of the data are fitted to a power law equation obtained in the early-time limit of the modified bound Brownian particle (MBBP): $\langle \Delta r^2(t) \rangle_{xs} = \langle \Delta r^2 \rangle_{xs,1s} (t/t_D)^{\beta}$, where t_D is fixed to be 1 s. The obtained fit parameters are described in Table 4.4.

(3.11) are poor, and no fit can be achieved for [SDS] = 20.0 mM given its very different shape, which could be caused by the proximity of the backscattering plateau in $g_2(t)$ - 1 to the baseline.

We further analyze $\langle \Delta r^2(t) \rangle$ for intermediate [SDS] (*i.e.* 27.5 mM to 64.7 mM) using the early-time optimized fit approach discussed in section 4.3.1. The optimized fit results for the [SDS] = 20.0 mM backscattering curve are not shown because the fit simply only matches the earliest time values, and the intermediate and long-time fitting parameters become ill-defined. The optimized fits for these [SDS] are shown in Figure 4.12. Fitting the early-time behavior of the $\langle \Delta r^2(t) \rangle$ reveals the presence of the excess MSDs at long-times. We quantify the excess MSD at long times through $\langle \Delta r^2(t) \rangle_{xs}$ and present the results in Figure 4.13. In both the transmission and backscattering signals, we find that the magnitude of $\langle \Delta r^2(t) \rangle_{xs}$ decreases with increasing [SDS] (*i.e.* increasing strength of the depletion attraction) for a given time scale. This indicates

that the existence of or movement of dangling loose clusters of droplets becomes more highly restricted as the attractive interactions are increased. This reasoning provides additional support for the earlier explanation made for emulsions at [SDS] = 89.9 mM, which hypothesized that stronger attractions effectively cause binding of these droplet clusters to the gelled networks and effectively eliminate the dynamics of collections of droplets that create the excess MSD signal. We also fit the $\langle \Delta r^2(t) \rangle_{xs}$ signals shown in Figure 4.13 using the early-time approximation describing dynamics of MBBP clusters. The early-time limit of the MBBP equation is given by a power law rise: $\langle \Delta r^2(t) \rangle_{xs} = \langle \Delta r^2 \rangle_{xs,1s} (t/t_D)^{\beta}$, where here we fix $t_D = 1$ s and $\langle \Delta r^2 \rangle_{xs,1s}$ is the excess MSD value at $t = 1$ s. We find that $\langle \Delta r^2 \rangle_{xs,1s}$ decreases as stronger attractions are induced at higher [SDS]. This is consistent with our hypothesis that droplet clusters are effectively attached to the stress supporting droplet networks in strong attraction limit. The fit analysis also showed that the all excess MSDs are sub-diffusive since $\beta < 1$ (average $\beta = 0.45 \pm 0.10$), and indicates that these clusters are being restrained by a gel network instead of freely diffusing in solution ($\beta = 1$ limit).

We have also compared our $G'_{p,DWS}$ extracted from early-time optimized fit to mechanical measurements for $\phi = 0.584$. We confirmed for the repulsive emulsion at [SDS] = 10 mM that the mechanically measured G'_p is within 20% of $G'_{p,DWS}$, which is within reasonable limits of uncertainty based on the sensitivity of G'_p to empirical inaccuracies in ϕ (see Figure 3.2). However, for the higher [SDS] measurements, a quantitative match of $G'_{p,DWS}$ with the mechanical measurements could not be obtained, even at [SDS] = 20.0 mM. Possible reasons for this relate to the differences in the sample preparation, difference in the time elapsed between the last sample handling and measurements for the two techniques, and that DWS imposes no

perturbation to the sample, whereas mechanical rheometry measurements require imposing an external shear strain which could cause re-arrangement of the gelled networks.

4.3.2.2 – Depletion-Induced Attractive Emulsions: Varying [SDS] at $\phi = 0.592$

We observe similar trends in the g_2(t) - 1 and the ℓ^* values (Figures 4.10 and 4.11) as a function of [SDS] for ϕ = 0.592 as we have already reported for ϕ = 0.584. Similar to the behavior found for ϕ = 0.584, the long-time values of $g_2(t)$ - 1 at ϕ = 0.592 initially decrease when [SDS] is increased to ≈ 20 mM. Thereafter, as [SDS] is raised, the long-time values of $g_2(t)$ - 1 rise again as [SDS] is further increased up to [SDS] = 91.0 mM. This suggests that even emulsions at ϕ = 0.592 may undergo initial melting due to addition of ionic SDS molecules before stronger depletion induced attractions give rise to elastic networks. One difference between the two data sets is that we can still measure a non-zero $g_2(t)$ - 1 signal for emulsions at ϕ = 0.592 with [SDS] ≈ 20 mM using the exact same DWS measurement configuration. This suggests that the emulsion having ϕ = 0.592 at 20 mM is more elastic than the emulsion having ϕ = 0.584 at [SDS] = 20 mM, consistent with the approach towards ϕ_{MRJ}. The trends of the two-step decay to non-zero long-time plateau that are observed in $g_2(t)$ -1 signals at ϕ = 0.584 are also observed for $g_2(t)$ -1 at ϕ = 0.592. With increasing [SDS], the second decay becomes more accentuated and delayed towards longer time scales, when compared with the $g_2(t)$ - 1 at ϕ = 0.584. We notice that the measured ℓ^* values for ϕ = 0.592, shown in Figure 4.11 with the ϕ = 0.584, lie close together so corrections to the DWS MSDs for collective scattering effects are similar. Over the range of [SDS] explored, there is some scatter in the measured ℓ^* values, and some of this scatter may be related to the absence of a high degree of homogeneity in the attractive emulsions and sensitivity to handling and loading.

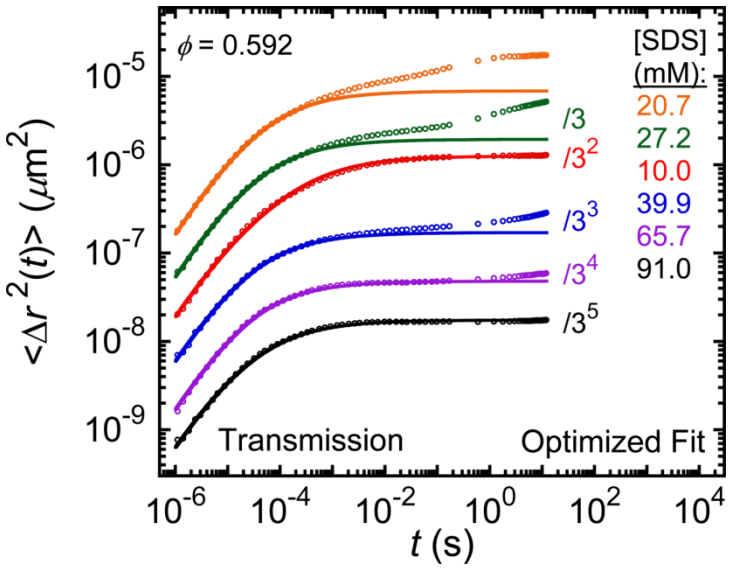

Figure 4.14. Measured mean square displacements $\langle \Delta r^2(t) \rangle$ and early-time optimized fits for different [SDS] at $\phi = 0.592$. The mean square displacements $\langle \Delta r^2(t) \rangle$ (circles; displayed every 1 in 3 data points for clarity) are determined through transmission DWS geometry. The $\langle \Delta r^2(t) \rangle$ values are optimized to fit early-time MSDs using equation (3.11). The fits are shown as line. No improvement to the fits (lines) could be found for 10.0 and 91.0 mM, so fit shown here goes through all available data. The [SDS] associated with each set of $\langle \Delta r^2(t) \rangle$ are listed (right) for data shown at long time t ~ 10 s (top to bottom). The optimized early-time fit parameters are described in Table 4.5. The fits and the $\langle \Delta r^2(t) \rangle$ are divided by the indicated factor next to the curve for visual clarity.

We analyze the measured $g_2(t)$ - 1 and obtain the $\langle S(q) \rangle$-corrected mean square displacements, $\langle \Delta r^2(t) \rangle$, shown in Figure 4.14. We find that the time-dependent MSD function for repulsive emulsions (equation (3.11)) describes the measured $\langle \Delta r^2(t) \rangle$ obtained from both the repulsive [SDS] = 10 mM and attractive emulsions at [SDS] ≈ 90 mM. For the samples at intermediate [SDS] between these limits, the fit does not describe all of our measured $\langle \Delta r^2(t) \rangle$ for all times well, akin to the results we showed for $\phi = 0.584$. So, we perform an early-time $\langle \Delta r^2(t) \rangle$ optimized fit to [SDS] = 20.7, 27.2, 39.9, and 65.7 mM (lines in Figure 4.14) and obtain the excess residual MSD signals $\langle \Delta r^2(t) \rangle_{xs}$ as displayed in Figure 4.15.

We fit the excess MSD $\langle \Delta r^2(t) \rangle_{xs}$ to the MBBP equation and extract sub-diffusive behavior of $\langle \Delta r^2(t) \rangle_{xs}$, as shown in Figure 4.15. The emulsion at [SDS] = 20.7 mM SDS has a

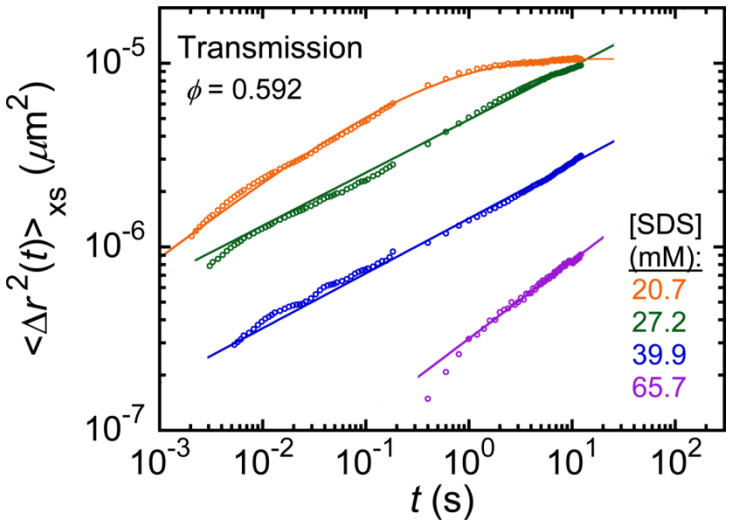

Figure 4.15. Excess mean square displacements $\langle\Delta r^2(t)\rangle_{xs}$ for different [SDS] at ϕ = 0.592. The calculated excess MSD signal $\langle\Delta r^2(t)\rangle_{xs}$ (circles), are determined from transmission DWS. The corresponding [SDS] are listed on the right for data shown (top to bottom). Data for 20.7 mM is fit to MBBP model shown in equation (4.3) and other sets of the data are fitted to a power law equation obtained in the early-time limit of the MBBP equation: $\langle\Delta r^2(t)\rangle_{xs} = \langle\Delta r^2\rangle_{xs,1s}(t/t_D)^{\beta}$, where t_D is fixed to be 1 s.The obtained fit parameters are described in Table 4.6.

distinguishable plateau and the corresponding $\langle\Delta r^2(t)\rangle_{xs}$ is fit to the total MBBP equation. Excess MSDs at other [SDS] are fitted to the early-time approximation of the MBBP equation. The obtained fit parameters are summarized in Table 4.6. We confirm that the excess MSDs are sub-diffusive (average β = 0.36 ± 0.08). However, unlike the results discussed for ϕ = 0.584, we notice that the magnitude of the $\langle\Delta r^2(t)\rangle_{xs}$ at long-times may not be monotonically decreasing as a function of increasing [SDS]. At long times around $t \approx 1$ s, the $\langle\Delta r^2(t)\rangle_{xs}$ signals for emulsions at [SDS] = 20.7 mM and 27.2 mM are almost identical in value. Emulsions with [SDS] = 20.7 mM have a $\langle\Delta r^2(t)\rangle_{xs}$ signal which has already plateaued to a value $\langle\Delta r^2\rangle_{xs,p}$ = (2.54 ± 0.02) x 10^{-5} μm^2. For emulsions at [SDS] = 27.2 mM, $\langle\Delta r^2(t)\rangle_{xs}$ appears to extend beyond the value $\langle\Delta r^2\rangle_{xs,p}$ found for [SDS] = 20.7 mM, as suggested by the extrapolation of the fit (shown in Figure 4.15). Due to the lack of $\langle\Delta r^2(t)\rangle_{xs}$ at longer times, it is difficult to reach accurate conclusions, but the extrapolated trend does suggest that the magnitude of $\langle\Delta r^2(t)\rangle_{xs}$ at long-times may be

monotonically decreasing only beyond a certain threshold [SDS]. Further experiments would be necessary to confirm this possibility.

4.3.2.3 – Depletion-Induced Attractive Emulsions: Elastic Shear Modulus and Excess MSD

In this section, we highlight two additionally observed trends that are seen both for ϕ = 0.584 and ϕ = 0.592. As emphasized previously, these ϕ points are within or near the electrostatically jammed regime for repulsive emulsions. From the early-time optimized fit analysis, we identify trends in $G'_{p,DWS}$ as a function of [SDS]. These values exhibit a rise and a plateau behavior with increasing [SDS] for both ϕ = 0.584 and ϕ = 0.592. This [SDS]-dependent behavior in $G'_{p,DWS}$ is well captured by an empirical sigmoid equation given by: $G'_{p,DWS}([SDS]) = G'_{p,max}/\{1+\exp[-([SDS]-[SDS]_0)/B]\} + G'_{p,0}$. Since the elasticity of repulsive emulsions will remain essentially unchanged at low [SDS], below 10 mM, we weighted the empirical sigmoidal equation by adding (unseen) points at [SDS] = 1 mM and 5 mM which corresponded to the $G'_{p,DWS}$ values obtained at [SDS] = 10 mM. By fitting each set of $G'_{p,DWS}$ at each ϕ to the sigmoidal curve, we obtain the following parameters: $G'_{p,max}$ = 460 ± 37 Pa, $[SDS]_0$ = 10.5 ± 2.2 mM, B = 32 ± 2 mM, and $G'_{p,0}$ = 45 ± 28 Pa for ϕ = 0.592 and $G'_{p,max}$ = 482 ± 155 Pa, $[SDS]_0$ = 8.3 ± 2.4 mM, B = 25 ± 2 mM, and $G'_{p,0}$ = 206 ± 44 Pa for ϕ = 0.584.

We also quantify the time scale associated with the onset of the excess MSD signal as function of attractive interaction potential for droplets in this electrostatically jammed regime. We define the onset time of the excess MSD, t_{xs}, to be the time at which the measured $\langle\Delta r^2(t)\rangle$ deviates from the early-time optimized $\langle\Delta r^2(t)\rangle_{fit}$ by more than 10% in value (*e.g.* t_{xs} represents the time beyond which $\langle\Delta r^2(t)\rangle_{xs}/\langle\Delta r^2(t)\rangle_{fit}$ becomes larger than 0.1). This criterion was chosen since the oscillating early-time signals due to vibrations present in the measurement have on average a maximum of ≈ 5% deviation when the fit to equation (3.11) is optimized. We combine

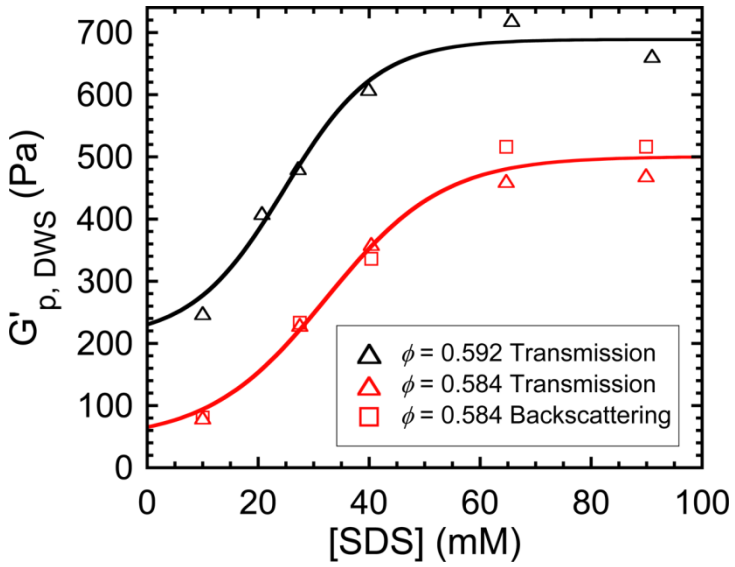

Figure 4.16. Dependence of DWS plateau shear elastic moduli $G'_{p,DWS}$ on [SDS] for attractive emulsions. The $G'_{p,DWS}$ parameter values at $\phi = 0.584$ (red) and $\phi = 0.592$ (black) are determined from G'_p parameter from the early-time optimized fit to equation (3.11). The fits performed can be found in Figures 4.12 and 4.14. $G'_{p,DWS}$ are determined from transmission (triangles) and backscattering (squares) signals. $G'_{p,DWS}([SDS])$ values at each ϕ are fit through an empirical sigmoidal curve $G'_{p,DWS}([SDS]) = G'_{p,max}/\{1+\exp(-([SDS]-[SDS]_0)/B)\} + G'_{p,0}$ and shown as lines. The determined parameters from the sigmoidal fit are $G'_{p,max} = 460 \pm 37$ Pa, $[SDS]_0 = 10.5 \pm 2.2$ mM, $B = 32 \pm 2$ mM, and $G'_{p,0} = 45 \pm 28$ Pa for $\phi = 0.592$ and are $G'_{p,max} = 482 \pm 155$ Pa, $[SDS]_0 = 8.3 \pm 2.4$ mM, $B = 25 \pm 2$ mM, and $G'_{p,0} = 206 \pm 44$ Pa for $\phi = 0.584$.

the results from $\phi = 0.584$ and $\phi = 0.592$ and co-plot t_{xs} as a function of [SDS], as shown in Figure 4.17. Interestingly, we observe that all set of t_{xs} can be well described by an exponential function: $t_{xs} = A_{txs} \exp([SDS]/[SDS]_{txs})$, where A_{txs} and $[SDS]_{txs}$ are fit parameters. We find that $A_{txs} = (2.2 \pm 1.0) \times 10^{-5}$ s and $[SDS]_{txs} = 5.7 \pm 0.4$ mM from the fit. It is worth noting that t_{xs} is proportional to exp([SDS]). Since [SDS] is linearly proportional to $|U_{attr}|$ in units of k_BT, such scaling relation implies that the onset time of the excess MSD signals, which may be related to thermal excitations of loose clusters, could be related to an attractive energy relative to a thermal energy in a Boltzmann factor.

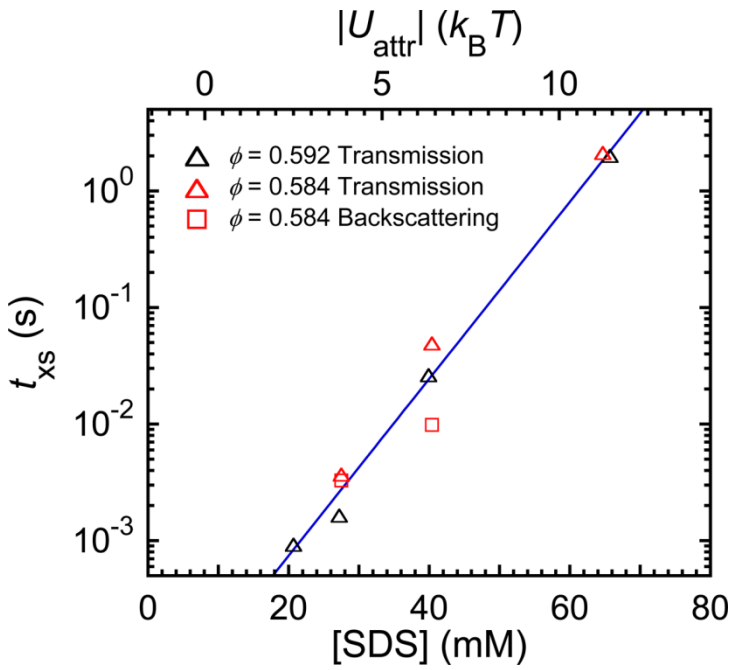

Figure 4.17. Excess MSD onset time t_{xs} as a function of [SDS]. The excess MSD onset time t_{xs} is the time at which the measured $\langle \Delta r^2(t) \rangle$ deviates from the early-time optimized fit of (3.11) by more than 10% in value. The data from transmission (triangles) and backscattering (squares) are color coded red (ϕ = 0.584) and black (ϕ = 0.592). All results shown are fitted to a [SDS]-dependent exponential function (blue line): $t_{xs} = A_{txs} \exp([SDS]/[SDS]_{txs})$. The determined parameters are: A_{txs} = (2.2 ± 1.0) x 10^{-5} s and $[SDS]_{txs}$ = 5.7 ± 0.4 mM. The attractive energies $|U_{attr}|$ associated with the given [SDS] are labeled along the top horizontal axis.

4.4 – Conclusions and Future Directions

We have investigated the microrheological behavior of depletion-induced attractive emulsions using DWS. We have begun by assuming that the MSD contributions from droplets in the main stress supporting structures, which are present in attractive emulsions, can be quantified through the temporal MSD equation developed for repulsive emulsions, yet fit only to early and intermediate time MSD data. Using weakly attractive emulsions as a starting point, we have demonstrated that this adaptation of the improved DWS microrheology analysis yields a reasonable agreement with mechanical measurements. By effectively removing the primary MSD signals, related to the stress supporting gel network of droplets, we have obtained excess

MSD signals, which we have attributed to excess dynamics of less highly bound clusters of droplets. Interestingly, the excess MSDs are described empirically by a MBBP equation. From fits using this MBBP equation, we have determined these excess MSDs are characterized by sub-diffusive dynamics at early times. Moreover, we have clearly shown that increasing $|U_{attr}|$ from ≈ $2.4k_BT$ to ≈ $16k_BT$ in depletion-induced attractive emulsions results in increases in the measured G'_p at fixed ϕ near but below ϕ_{MRJ}. Thus, we have shown that we can begin to quantify dynamic features associated with attractive emulsions via DWS and to make meaningful microrheological interpretations of the more complex dynamics found for attractive emulsions.

Based on the success of the adaptation in the weak attraction limit, we have expanded our analytical approach to emulsions experiencing stronger attractive interaction potentials. We have identified trends and quantified dynamics associated with droplet clusters inside gelled network of droplet as a function of [SDS] (*i.e.* strength of depletion induced attractions). Despite the revelation of interesting DWS microrheological features in attractive emulsions shown here, we have not validated against mechanical measurements. Therefore, further experimentation is needed to verify the validity of this analytical approach or to modify this approach in order to describe strongly attractive emulsions. Moreover, it is not clear whether the DWS analysis can be extended to attractive emulsions for ϕ far below ϕ_{MRJ}. To corroborate this DWS analysis, a more refined experimental protocol, which emphasizes strict control of sample handling and pre-treatment, may be required. Nonetheless, we believe the analytical approach described herein serves as a starting point for investigating attractive emulsions, since we have established quantitative agreement between DWS microrheology results and mechanical rheometry using weakly attractive emulsions that have been washed repeatedly to set [SDS] = 20 mM.

4.5 – Tables

Table 4.1. Parameters used for optimized early-time MSD fit: 20 mM SDS emulsions.

ϕ	DWS geometry	G'_p (Pa)	τ (s)	η_∞ (Pa s)
0.584	Transmission	113 ± 3	0.1370 ± 0.0008	0.026 ± 0.001
0.592	Transmission	476 ± 11	0.1079 ± 0.0004	0.0139 ± 0.0001
0.601	Transmission	584 ± 8	0.0097 ± 0.0002	0.0137 ± 0.0001
0.616	Transmission	909 ± 13	0.0081 ± 0.0002	0.0148 ± 0.0002
0.629	Transmission	1386 ± 12	0.0071 ± 0.0002	0.0172 ± 0.0003
0.647	Transmission	1897 ± 11	0.0064 ± 0.0001	0.0192 ± 0.0003
0.573	Backscattering	93 ± 4	0.0339 ± 0.0019	0.0160 ± 0.0001
0.584	Backscattering	119 ± 4	0.0248 ± 0.0012	0.0156 ± 0.0001
0.592	Backscattering	430± 10	0.1160 ± 0.0005	0.0145 ± 0.002
0.601	Backscattering	620 ± 20	0.0097 ± 0.0005	0.0144 ± 0.0002
0.616	Backscattering	972 ± 15	0.0081 ± 0.0003	0.0159 ± 0.0001
0.629	Backscattering	1417 ± 13	0.0070 ± 0.0002	0.0176 ± 0.0002
0.647	Backscattering	1973 ± 14	0.0063 ± 0.0001	0.0194 ± 0.0003

Table 4.2. MBBP fit parameters to excess MSDs: 20 mM SDS emulsions.

ϕ	DWS geometry	$\langle \Delta r^2 \rangle_{xs,p}$ (μm^2)	t_D (s)	β
0.584	Transmission	$(5.5 \pm 0.05) \times 10^{-5}$	$(1.5 \pm 0.05) \times 10^{-1}$	$(6.0 \pm 0.5) \times 10^{-1}$
0.592	Transmission	$(7.15 \pm 0.01) \times 10^{-6}$	$(1.24 \pm 0.02) \times 10^{-1}$	$(4.23 \pm 0.03) \times 10^{-1}$
0.601	Transmission	$(4.47 \pm 0.01) \times 10^{-6}$	$(1.39 \pm 0.03) \times 10^{-1}$	$(4.12 \pm 0.04) \times 10^{-1}$
0.616	Transmission	$(1.37 \pm 0.01) \times 10^{-6}$	$(1.49 \pm 0.05) \times 10^{-1}$	$(3.95 \pm 0.06) \times 10^{-1}$
0.629	Transmission	$(2.80 \pm 0.02) \times 10^{-7}$	$(4.1 \pm 0.3) \times 10^{-1}$	$(4.7 \pm 0.1) \times 10^{-1}$
0.647	Transmission	$(7.71 \pm 0.09) \times 10^{-8}$	$(2.1 \pm 0.2) \times 10^{-1}$	$(8.3 \pm 0.8) \times 10^{-1}$
0.573	Backscattering	$(9.85 \pm 0.03) \times 10^{-7}$	$(2.07 \pm 0.05) \times 10^{-1}$	$(5.7 \pm 0.1) \times 10^{-1}$
0.584	Backscattering	$(6.05 \pm 0.01) \times 10^{-5}$	$(1.21 \pm 0.02) \times 10^{-1}$	$(5.54 \pm 0.08) \times 10^{-1}$
0.592	Backscattering	$(8.01 \pm 0.02) \times 10^{-6}$	$(8.9 \pm 0.3) \times 10^{-2}$	$(4.44 \pm 0.07) \times 10^{-1}$
0.601	Backscattering	$(4.96 \pm 0.02) \times 10^{-6}$	$(9.8 \pm 0.4) \times 10^{-2}$	$(3.82 \pm 0.07) \times 10^{-1}$
0.616	Backscattering	$(1.84 \pm 0.02) \times 10^{-6}$	$(8.7 \pm 0.9) \times 10^{-2}$	$(3.2 \pm 0.1) \times 10^{-1}$

Table 4.3. Parameters used for optimized early-time MSD fit: $\phi = 0.584$ emulsions. Data sets marked with * indicate obtained MSD fit parameters through entire set since fit could not be optimized.

[SDS] (mM)	DWS geometry	G'_p (Pa)	τ (s)	η_∞ (Pa s)
10.0	Transmission*	80.7 ± 0.3	0.0414 ± 0.0001	0.0141 ± 0.0002
20.0	Transmission	N/A	N/A	N/A
27.5	Transmission	230 ± 10	0.015 ± 0.0004	0.013 ± 0.001
40.4	Transmission	360 ± 15	0.0128 ± 0.0002	0.0145 ± 0.0001
64.7	Transmission	461 ± 6	0.0108 ± 0.0003	0.0134 ± 0.0001
89.9	Transmission*	470 ± 1	0.0114 ± 0.0001	0.0137 ± 0.0001
10.0	Backscattering	81 ± 4	0.034 ± 0.002	0.0141 ± 0.0001
20.0	Backscattering	N/A	N/A	N/A
27.5	Backscattering	233 ± 5	0.0162 ± 0.0007	0.0139 ± 0.0001
40.4	Backscattering	336 ± 5	0.0126 ± 0.0004	0.0134 ± 0.0001
64.7	Backscattering	516 ± 7	0.011 ± 0.003	0.0159 ± 0.0001
89.9	Backscattering*	516 ± 2	0.0131 ± 0.0002	0.0173 ± 0.0001

Table 4.4. Early-time MBBP approximation fit parameters: $\phi = 0.584$ emulsions.

[SDS](mM)	DWS geometry	$\langle \Delta r^2 \rangle_{xs,1s}$ (μm^2)	β
27.5	Transmission	$(2.54 \pm 0.02) \times 10^{-5}$	$(4.00 \pm 0.06) \times 10^{-1}$
40.4	Transmission	$(4.29 \pm 0.01) \times 10^{-6}$	$(5.23 \pm 0.01) \times 10^{-1}$
64.7	Transmission	$(4.37 \pm 0.06) \times 10^{-7}$	$(5.80 \pm 0.08) \times 10^{-1}$
27.5	Backscattering	$(2.43 \pm 0.01) \times 10^{-5}$	$(3.76 \pm 0.03) \times 10^{-1}$
40.4	Backscattering	$(4.72 \pm 0.03) \times 10^{-6}$	$(3.73 \pm 0.04) \times 10^{-1}$

Table 4.5. Parameters used for optimized early-time MSD fit: $\phi = 0.592$ emulsions. Data sets marked with * indicate obtained MSD fit parameters through entire set since fit could not be optimized.

[SDS] (mM)	G'_p (Pa)	τ (s)	η_∞ (Pa s)
10.0*	249 ± 1	0.0236 ± 0.0003	0.0118 ± 0.0002
20.7	410 ± 7	0.0114 ± 0.0003	0.0134 ± 0.0001
27.2	482 ± 10	0.01051 ± 0.0004	0.0133 ± 0.0001
39.9	609 ± 17	0.0092 ± 0.0004	0.0129 ± 0.0002
65.7	720 ± 60	0.0085 ± 0.005	0.0155 ± 0.0005
91.0*	662 ± 14	0.0099 ± 0.0005	0.0129 ± 0.0003

Table 4.6. MBBP model fit parameters: $\phi = 0.592$ emulsions.

[SDS](mM)	$\langle \Delta r^2 \rangle_{xs,p}$ * or $\langle \Delta r^2 \rangle_{xs,1s}$ (μm^2)	t_D (s)	β
20.7 *	$(1.056 \pm 0.002) \times 10^{-5}$	$(2.68 \pm 0.06) \times 10^{-1}$	$(4.39 \pm 0.03) \times 10^{-1}$
27.2	$(4.92 \pm 0.03) \times 10^{-6}$	-	$(2.88 \pm 0.03) \times 10^{-1}$
39.9	$(1.425 \pm 0.007) \times 10^{-6}$	-	$(2.99 \pm 0.02) \times 10^{-1}$
65.7	$(3.16 \pm 0.06) \times 10^{-7}$	-	$(4.23 \pm 0.06) \times 10^{-1}$

Chapter 5 – Conclusions and Future Directions

Through this dissertation research, we have improved the quantitative description and diffusing wave microrheology measurements of jammed ionic monodisperse emulsions. In particular, we have explored the rheological properties of these systems, particularly the linear plateau shear elastic modulus G'_p. Starting with short-range repulsive emulsions, we have developed an analytical EEI model, and we have improved the DWS microrheology analysis by accounting for collective scattering effects, so that it is now possible to predict accurately G'_p values that match with macroscopic mechanical rheometry. We have also extended this improved DWS analysis for repulsive emulsions to DWS measurements of depletion-induced attractive emulsions in a certain limited range of ϕ near but below jamming. By extending this analysis to attractive emulsions, we have quantitatively identified DWS characteristics that are associated with such attractive emulsions, including additional ϕ-dependent features in the decays of the correlation functions $g_2(t)$ - 1 and in the extracted mean square displacements as a function of the attractive interaction potential.

In Chapter 2, we have developed the EEI model that now provides predictive capabilities of a colloidal, ionic, disordered monodisperse emulsion's G'_p and Π below, through, and above the jamming regime in the weak droplet deformation limit. Expanding on prior models, we have developed an analytical model, which accounts for all three main contributions to a quasi-equilibrium free energy (entropy, electrostatic repulsions, and interfacial deformation energies) for the first time. For model SDS-stabilized PDMS O/W emulsions, using only three universal adjustable parameters, we have demonstrated that the EEI model can accurately describe many sets of mechanical measurements of $G'_p(\phi)$, which span over three decades, for both micro- and

nano-scale droplets. This approach obviates the need for an *ad hoc* adjustment to the droplet volume fraction ϕ in order to create an effective volume fraction ϕ_{eff}, which has been the case for decades in the experimental literature on emulsion rheology. Furthermore, we have used this EEI model to distinguish between different regimes of jamming, such as electrostatically jammed and interfacially jammed regimes, and consequently there is now better physical insight into the fundamental origins of the jamming elasticity of such charge-stabilized repulsive emulsions. Given the success and simplicity of the EEI model, we believe that it will serve as an excellent prototype for generalization to other types of colloidal soft materials composed that contain monodisperse disordered jammed soft constituents other than droplets.

In Chapter 3, we have developed an improved DWS microrheology analysis for highly concentrated colloidal dispersions that yield accurate passive thermal-entropic microrheology measurements of G'_{p} for jammed emulsions. At high concentrations of droplets, as in jammed emulsions, we show that collective scattering effects can do much more than merely perturb DWS analysis, so the extracted MSDs, obtained using the standard DWS analysis protocol, do not yield single-probe self-motion MSDs that are necessary for accurate microrheology predictions via the GSER. We have performed mechanical and DWS measurements on the same exact jammed monodisperse emulsion samples prepared at different ϕ to facilitate direct corroboration of the mechanical and microrheology measurements and to investigate the effect of collective scattering in DWS measurements and analysis. The apparent DWS MSDs are corrected for collective scattering effects using an empirically determined average structure factor $\langle S(q) \rangle$. This $\langle S(q) \rangle$ is ϕ-dependent and can be readily determined from measurements of the optical transport mean free paths ℓ^* from dilute to concentrated ϕ. Moreover, we have derived a fitting function for the time-dependent mean square displacement of a single droplet in the

jammed regime using the GSER. From the fits to MSDs corrected for collective scattering, we extract DWS measurement values for $G'_p(\phi)$, as we have demonstrated by comparing these against mechanical measurements of $G'_p(\phi)$. Thus, we have shown that there is a straightforward and viable route for correcting for collective scattering effects when performing DWS microrheology of highly concentrated homogeneous dispersions, including emulsions. Furthermore, we have extracted the ϕ-dependence of interesting high-frequency rheological properties of jammed emulsions, such as a power-law scaling expression describing the $s^{1/2}$ dependent anomalous viscous loss in jammed emulsions. We believe that this improved analysis route opens up many possibilities for accurately quantifying microrheological properties of other highly concentrated dispersions or soft matter, such as hard spheres and microgels.

Motivated by the advances in DWS microrheology for repulsive emulsions, we have performed DWS measurements on depletion-induced attractive emulsions by controlling the SDS micelle concentration. By using the improved DWS analysis and also the time-dependent MSD fitting function for average single droplet behavior in a jammed emulsion (developed in Chapter 3), we reveal new and interesting DWS features in the correlation functions and MSDs associated with attractive emulsions. Using weak attractions at 20 mM, we have established a method for extracting time-dependent excess MSDs $\langle \Delta r^2(t) \rangle_{xs}$, which we believe are associated with some loose or dangling clusters of droplets that move through Brownian excitations in lower-density void spaces between higher density stress-supporting struts in gelled networks of attractive droplets. We have quantified $\langle \Delta r^2(t) \rangle_{xs}$ as a function of ϕ and depletion attraction strengths near and below the jamming limit of hard spheres; this identification of an excess MSD has enabled us to identify that the dynamics of the loose aggregated structures is sub-diffusive in nature at early times. Although much more careful experiments and comparisons with

mechanical rheometry, theory, and simulation are needed to further explore the meaning of these findings, we anticipate that this approach will likely be useful in studying rheological properties of attractive emulsions and other attractive systems in the future.

References

1. Leal-Calderon, F.; Schmitt, V.; Bibette, J., *Emulsion Science - Basic Principles*. 2nd ed.; Springer-Verlag: New York, 2007.

2. Schramm, L. L., In *Emulsions, Foams, Suspensions, and Aerosols*, Wiley-VCH Verlag GmbH & Co. KGaA: 2014.

3. Taylor, G. I., The formation of emulsions in definable fields of flow. *Proc. Royal Soc. Lond. A* 1934**,** *146* (858), 501-523.

4. Fryd, M. M.; Mason, T. G., Advanced nanoemulsions. *Annu. Rev. Phys. Chem* 2012**,** *63* (1), 493-518.

5. Mason, T. G.; Wilking, J. N.; Meleson, K.; Chang, C. B.; Graves, S. M., Nanoemulsions: Formation, structure, and physical properties. *J. Phys. Condens. Matter* 2006**,** *18* (41), R635.

6. Meleson, K.; Graves, S.; Mason, T. G., Formation of concentrated nanoemulsions by extreme shear. *Soft Mater.* 2004**,** *2* (2-3), 109-123.

7. Taylor, P., Ostwald ripening in emulsions. *Adv. Colloid Interface Sci* 1998**,** *75* (2), 107-163.

8. Huang, J. S.; Kim, M. W., Critical behavior of a microemulsion. *Phys. Rev. Lett.* 1981**,** *47* (20), 1462-1465.

9. Langevin, D., Microemulsions - interfacial aspects. *Adv. Colloid Interface Sci* 1991**,** *34*, 583-595.

10. Pouchelon, A.; Chatenay, D.; Meunier, J.; Langevin, D., Origin of low interfacial tensions in systems involving microemulsion phases. *J. Colloid Interface Sci.* 1981**,** *82* (2), 418-422.

11. Reiss, H.; Ellerby, H. M.; Manzanares, J. A., Configurational entropy of microemulsions: The fundamental length scale. *J. Chem. Phys.* 1993**,** *99* (12), 9930-9937.

12. Forgiarini, A.; Esquena, J.; González, C.; Solans, C., Formation of nano-emulsions by low-energy emulsification methods at constant temperature. *Langmuir* 2001**,** *17* (7), 2076-2083.

13. Barnes, H. A., Rheology of emulsions - a review. *Colloids Surf. A* 1994**,** *91*, 89-95.

14. Lequeux, F., Emulsion rheology. *Curr. Opin. Colloid Interface Sci.* 1998**,** *3* (4), 408-411.

15. Mason, T. G.; Krall, A. H.; Gang, H.; Bibette, J.; Weitz, D. A., Monodisperse emulsions: Properties and use. In *Encyclopedia of Emulsion Technology*, Becher, P., Ed. Marcel Dekker, Inc.: New York, 1996; Vol. 4, pp 299-336.

16. Mason, T. G., New fundamental concepts in emulsion rheology. *Curr. Opin. Colloid Interface Sci.* 1999**,** *4* (3), 231-238.

17. Lozsan, A., Salt-induced fast aggregation of nano-emulsions: Structural and kinetic scaling. *Colloid Polym. Sci* 2012**,** *290* (15), 1561-1566.

18. Wilking, J. N.; Graves, S. M.; Chang, C. B.; Meleson, K.; Lin, M. Y.; Mason, T. G., Dense cluster formation during aggregation and gelation of attractive slippery nanoemulsion droplets. *Phys. Rev. Lett.* 2006**,** *96* (1), 015501.

19. Aben, S.; Holtze, C.; Tadros, T.; Schurtenberger, P., Rheological investigations on the creaming of depletion-flocculated emulsions. *Langmuir* 2012**,** *28* (21), 7967-7975.

20. Meller, A.; Gisler, T.; Weitz, D. A.; Stavans, J., Viscoelasticity of depletion-induced gels in emulsion−polymer systems. *Langmuir* 1999**,** *15* (6), 1918-1922.

21. Meller, A.; Stavans, J., Stability of emulsions with nonadsorbing polymers. *Langmuir* 1996**,** *12* (2), 301-304.

22. Bibette, J.; Roux, D.; Nallet, F., Depletion interactions and fluid-solid equilibrium in emulsions. *Phys. Rev. Lett.* 1990**,** *65* (19), 2470-2473.

23. Datta, S. S.; Gerrard, D. D.; Rhodes, T. S.; Mason, T. G.; Weitz, D. A., Rheology of attractive emulsions. *Phys. Rev. E* 2011**,** *84* (4), 041404.

24. Petsev, D. N.; Denkov, N. D.; Kralchevsky, P. A., Flocculation of deformable emulsion droplets. *J. Colloid Interface Sci.* 1995**,** *176* (1), 201-213.

25. Steiner, U.; Meller, A.; Stavans, J., Entropy driven phase separation in binary emulsions. *Phys. Rev. Lett.* 1995**,** *74* (23), 4750-4753.

26. Asakura, S.; Oosawa, F., On interaction between two bodies immersed in a solution of macromolecules. *J. Chem. Phys.* 1954**,** *22* (7), 1255-1256.

27. Asakura, S.; Oosawa, F., Interaction between particles suspended in solutions of macromolecules. *J. Polym. Sci.* 1958**,** *33* (126), 183-192.

28. Fall, A.; Paredes, J.; Bonn, D., Yielding and shear banding in soft glassy materials. *Phys. Rev. Lett.* 2010**,** *105* (22), 225502.

29. Helgeson, M. E.; Moran, S. E.; An, H. Z.; Doyle, P. S., Mesoporous organohydrogels from thermogelling photocrosslinkable nanoemulsions. *Nat. Mater* 2012**,** *11* (4), 344-352.

30. Berryman, J. G., Random close packing of hard spheres and disks. *Phys. Rev. A* 1983**,** *27* (2), 1053-1061.

31. Torquato, S.; Truskett, T. M.; Debenedetti, P. G., Is random close packing of spheres well defined? *Phys. Rev. Lett.* 2000**,** *84* (10), 2064-2067.

32. Mason, T. G. Rheology of Monodisperse Emulsions. Ph. D. Dissertation, Princeton University, Princeton, 1995.

33. Mason, T. G.; Bibette, J.; Weitz, D. A., Elasticity of compressed emulsions. *Phys. Rev. Lett.* 1995**,** *75* (10), 2051-2054.

34. Mason, T. G.; Bibette, J.; Weitz, D. A., Yielding and flow of monodisperse emulsions. *J. Colloid Interface Sci.* 1996**,** *179* (2), 439-448.

35. Mason, T. G.; Lacasse, M. D.; Grest, G. S.; Levine, D.; Bibette, J.; Weitz, D. A., Osmotic pressure and viscoelastic shear moduli of concentrated emulsions. *Phys. Rev. E* 1997**,** *56* (3), 3150-3166.

36. Princen, H. M., Rheology of foams and highly concentrated emulsions. *J. Colloid Interface Sci.* 1983**,** *91* (1), 160-175.

37. Princen, H. M., Rheology of foams and highly concentrated emulsions. II. Experimental study of the yield stress and wall effects for concentrated oil-in-water emulsions. *J. Colloid Interface Sci.* 1985**,** *105* (1), 150-171.

38. Princen, H. M.; Kiss, A. D., Rheology of foams and highly concentrated emulsions: III. Static shear modulus. *J. Colloid Interface Sci.* 1986**,** *112* (2), 427-437.

39. Princen, H. M.; Kiss, A. D., Rheology of foams and highly concentrated emulsions. *J. Colloid Interface Sci.* 1989**,** *128* (1), 176-187.

40. Desmond, K. W.; Weeks, E. R., Influence of particle size distribution on random close packing of spheres. *Phys. Rev. E* 2014**,** *90* (2), 022204.

41. Dasgupta, B. R.; Tee, S.-Y.; Crocker, J. C.; Frisken, B. J.; Weitz, D. A., Microrheology of polyethylene oxide using diffusing wave spectroscopy and single scattering. *Phys. Rev. E* 2002**,** *65* (5), 051505.

42. Huang, J.-R.; Mason, T. G., Shear oscillation light scattering of droplet deformation and reconfiguration in concentrated emulsions. *Europhys. Lett.* 2008**,** *83* (2), 28004.

43. Huang, J.-R.; Mason, T. G., Deformation, restructuring, and un-jamming of concentrated droplets in large-amplitude oscillatory shear flows. *Soft Matter* 2009**,** *5* (11), 2208-2214.

44. Hales, T. C., A proof of the Kepler conjecture. *Ann. Math.* 2005**,** *162* (3), 1065-1185.

45. Mason, T. G.; Rai, P. K., Shear-induced elastification of concentrated emulsions probed by sinusoidal amplitude variation rheometry. *J. Rheol.* 2003**,** *47* (2), 513-533.

46. Wilking, J. N.; Mason, T. G., Irreversible shear-induced vitrification of droplets into elastic nanoemulsions by extreme rupturing. *Phys. Rev. E* 2007**,** *75* (4), 041407.

47. Scheffold, F.; Mason, T. G., Scattering from highly packed disordered colloids. *J. Phys. Condens. Matter* 2009**,** *21* (33), 332102.

48. Mason, T. G.; Scheffold, F., Crossover between entropic and interfacial elasticity and osmotic pressure in uniform disordered emulsions. *Soft Matter* 2014**,** *10* (36), 7109-7116.

49. Scheffold, F.; Wilking, J. N.; Haberko, J.; Cardinaux, F.; Mason, T. G., The jamming elasticity of emulsions stabilized by ionic surfactants. *Soft Matter* 2014**,** *10* (28), 5040-5044.

50. Mason, T. G.; Bibette, J., Emulsification in viscoelastic media. *Phys. Rev. Lett.* 1996**,** *77* (16), 3481-3484.

51. Mason, T. G.; Bibette, J., Shear rupturing of droplets in complex fluids. *Langmuir* 1997**,** *13* (17), 4600-4613.

52. Omi, S., Preparation of monodisperse microspheres using the Shirasu porous glass emulsification technique. *Colloids Surf. A* 1996**,** *109*, 97-107.

53. Vladisavljevic, G. T.; Schubert, H., Preparation and analysis of oil-in-water emulsions with a narrow droplet size distribution using Shirasu-porous-glass (SPG) membranes. *Desalination* 2002**,** *144* (1), 167-172.

54. Bragg, L.; Nye, J. F., A dynamical model of a crystal structure. *Proc. R. Soc. Lond. A Math. Phys. Sci.* 1947**,** *190* (1023), 474.

55. Umbanhowar, P. B.; Prasad, V.; Weitz, D. A., Monodisperse emulsion generation via drop break off in a coflowing stream. *Langmuir* 2000**,** *16* (2), 347-351.

56. Cubaud, T.; Mason, T. G., Capillary threads and viscous droplets in square microchannels. *Phys. Fluids* 2008**,** *20* (5), 053302.

57. Link, D. R.; Anna, S. L.; Weitz, D. A.; Stone, H. A., Geometrically mediated breakup of drops in microfluidic devices. *Phys. Rev. Lett.* 2004**,** *92* (5), 054503.

58. Ménétrier-Deremble, L.; Tabeling, P., Droplet breakup in microfluidic junctions of arbitrary angles. *Phys. Rev. E* 2006**,** *74* (3), 035303.

59. Bibette, J., Depletion interactions and fractionated crystallization for polydisperse emulsion purification. *J. Colloid Interface Sci.* 1991**,** *147* (2), 474-478.

60. Bernal, J. D.; Mason, J., Packing of spheres: Co-ordination of randomly packed spheres. *Nature* 1960**,** *188* (4754), 910-911.

61. Mason, T. G.; Weitz, D. A., Linear viscoelasticity of colloidal hard sphere suspensions near the glass transition. *Phys. Rev. Lett.* 1995**,** *75* (14), 2770-2773.

62. Russel, W. B.; Saville, D. A.; Schowalter, W. R., *Colloidal Dispersions*. Cambridge University Press: Cambridge, 1989.

63. Pusey, P. N.; van Megen, W., Phase behaviour of concentrated suspensions of nearly hard colloidal spheres. *Nature* 1986**,** *320* (6060), 340-342.

64. Cipelletti, L.; Weeks, E. R., Glassy dynamics and dynamical heterogeneity in colloids. In *Dynamical Heterogeneities in Glasses, Colloids, and Granular Media*, Berthier, L.; Biroli, G.; Bouchaud, J.-P.; Cipelletti, L.; van Saarloos, W., Eds. Oxford University Press: 2011.

65. Gary, L. H.; Eric, R. W., The physics of the colloidal glass transition. *Rep. Prog. Phys.* 2012**,** *75* (6), 066501.

66. Weeks, E. R.; Crocker, J. C.; Levitt, A. C.; Schofield, A.; Weitz, D. A., Three-dimensional direct imaging of structural relaxation near the colloidal glass transition. *Science* 2000**,** *287* (5453), 627-631.

67. Mason, T. G.; Gang, H.; Weitz, D. A., Diffusing-wave-spectroscopy measurements of viscoelasticity of complex fluids. *J. Opt. Soc. Am. A* 1997**,** *14* (1), 139-149.

68. Woodcock, L. V., Glass transition in the hard-sphere model and Kauzmann's paradox*. *Ann. N. Y. Acad. Sci.* 1981**,** *371* (1), 274-298.

69. Morse, D. C.; Witten, T. A., Droplet elasticity in weakly compressed emulsions. *Europhys. Lett.* 1993**,** *22* (7), 549-555.

70. Ikeda, A.; Berthier, L.; Sollich, P., Unified study of glass and jamming rheology in soft particle systems. *Phys. Rev. Lett.* 2012**,** *109* (1), 018301.

71. Ikeda, A.; Berthier, L.; Sollich, P., Disentangling glass and jamming physics in the rheology of soft materials. *Soft Matter* 2013**,** *9* (32), 7669-7683.

72. Lacasse, M. D.; Grest, G. S.; Levine, D.; Mason, T. G.; Weitz, D. A., Model for the elasticity of compressed emulsions. *Phys. Rev. Lett.* 1996**,** *76* (18), 3448-3451.

73. Clara-Rahola, J.; Brzinski, T. A.; Semwogerere, D.; Feitosa, K.; Crocker, J. C.; Sato, J.; Breedveld, V.; Weeks, E. R., Affine and nonaffine motions in sheared polydisperse emulsions. *Phys. Rev. E* 2015**,** *91* (1), 010301.

74. Schlegel, M.; Brujic, J.; Terentjev, E. M.; Zaccone, A., Local structure controls the nonaffine shear and bulk moduli of disordered solids. *Sci. Rep.* 2016**,** *6*, 18724.

75. Zhang, C.; O'Donovan, C. B.; Corwin, E. I.; Cardinaux, F.; Mason, T. G.; Möbius, M. E.; Scheffold, F., Structure of marginally jammed polydisperse packings of frictionless spheres. *Phys. Rev. E* 2015**,** *91* (3), 032302.

76. Brujic, J.; Edwards, S. F.; Grinev, D. V.; Hopkinson, I.; Brujic, D.; Makse, H. A., 3D bulk measurements of the force distribution in a compressed emulsion system. *Faraday Discuss.* 2003**,** *123* (0), 207-220.

77. Brujić, J.; Song, C.; Wang, P.; Briscoe, C.; Marty, G.; Makse, H. A., Measuring the coordination number and entropy of a 3D jammed emulsion packing by confocal microscopy. *Phys. Rev. Lett.* 2007**,** *98* (24), 248001.

78. Clusel, M.; Corwin, E. I.; Siemens, A. O. N.; Brujic, J., A 'granocentric' model for random packing of jammed emulsions. *Nature* 2009**,** *460* (7255), 611-615.

79. Jorjadze, I.; Pontani, L.-L.; Brujic, J., Microscopic approach to the nonlinear elasticity of compressed emulsions. *Phys. Rev. Lett.* 2013**,** *110* (4), 048302.

80. Zhang, C.; Gnan, N.; Mason, T. G.; Zaccarelli, E.; Scheffold, F., Dynamical and structural signatures of the glass transition in emulsions. *J. Stat. Mech.: Theory Exp.* 2016**,** *2016* (9), 094003.

81. Richard, P.; Oger, L.; Troadec, J. P.; Gervois, A., A model of binary assemblies of spheres. *Eur. Phys. J. E* 2001**,** *6* (4), 295-303.

82. O'Hern, C. S.; Silbert, L. E.; Liu, A. J.; Nagel, S. R., Jamming at zero temperature and zero applied stress: The epitome of disorder. *Phys. Rev. E* 2003**,** *68* (1), 011306.

83. Knowlton, E. D.; Pine, D. J.; Cipelletti, L., A microscopic view of the yielding transition in concentrated emulsions. *Soft Matter* 2014**,** *10* (36), 6931-6940.

84. Mason, T. G.; Weitz, D. A., Optical measurements of frequency-dependent linear viscoelastic moduli of complex fluids. *Phys. Rev. Lett.* 1995**,** *74* (7), 1250-1253.

85. Liu, A. J.; Ramaswamy, S.; Mason, T. G.; Gang, H.; Weitz, D. A., Anomalous viscous loss in emulsions. *Phys. Rev. Lett.* 1996**,** *76* (16), 3017-3020.

86. Tighe, B. P., Relaxations and rheology near jamming. *Phys. Rev. Lett.* 2011**,** *107* (15), 158303.

87. Bibette, J.; Mason, T. G.; Gang, H.; Weitz, D. A.; Poulin, P., Structure of adhesive emulsions. *Langmuir* 1993**,** *9* (12), 3352-3356.

88. Bibette, J.; Mason, T. G.; Hu, G.; Weitz, D. A., Kinetically induced ordering in gelation of emulsions. *Phys. Rev. Lett.* 1992**,** *69* (6), 981-984.

89. Bécu, L.; Manneville, S.; Colin, A., Yielding and flow in adhesive and nonadhesive concentrated emulsions. *Phys. Rev. Lett.* 2006**,** *96* (13), 138302.

90. Paredes, J.; Shahidzadeh-Bonn, N.; Bonn, D., Shear banding in thixotropic and normal emulsions. *J. Phys. Condens. Matter* 2011**,** *23* (28), 284116.

91. Erramreddy, V. V.; Ghosh, S., Influence of emulsifier concentration on nanoemulsion gelation. *Langmuir* 2014**,** *30* (37), 11062-11074.

92. Pusey, P. N.; van Megen, W., Observation of a glass transition in suspensions of spherical colloidal particles. *Phys. Rev. Lett.* 1987**,** *59* (18), 2083-2086.

93. Buzza, D., M. A.; D. Lu, C.-Y.; Cates, M., E., Linear shear rheology of incompressible foams. *J. Phys. II France* 1995**,** *5* (1), 37-52.

94. Scheffold, F.; Cardinaux, F.; Mason, T. G., Linear and nonlinear rheology of dense emulsions across the glass and the jamming regimes. *J. Phys. Condens. Matter* 2013**,** *25* (50), 502101.

95. Israelachvili, J. N., *Intermolecular and Surface Forces*. 3rd ed.; Academic Press: London, 2011.

96. Liu, A. J.; Nagel, S. R., The jamming transition and the marginally jammed solid. *Annu. Rev. Condens. Matter Phys* 2010**,** *1* (1), 347-369.

97. Seth, J. R.; Cloitre, M.; Bonnecaze, R. T., Elastic properties of soft particle pastes. *J. Rheol.* 2006**,** *50* (3), 353-376.

98. van Hecke, M., Jamming of soft particles: Geometry, mechanics, scaling and isostaticity. *J. Phys. Condens. Matter* 2010**,** *22* (3), 033101.

99. Zhu, X.; Fryd, M. M.; Huang, J.-R.; Mason, T. G., Optically probing nanoemulsion compositions. *Phys. Chem. Chem. Phys.* 2012**,** *14* (7), 2455-2461.

100. Hanson, J. A.; Chang, C. B.; Graves, S. M.; Li, Z.; Mason, T. G.; Deming, T. J., Nanoscale double emulsions stabilized by single-component block copolypeptides. *Nature* 2008**,** *455* (7209), 85-88.

101. Zuidema, H.; Waters, G., Ring method for determination of interfacial tension. *Ind. Eng. Chem., Anal. Ed.* 1941**,** *13* (5), 312-313.

102. Snook, I.; van Megen, W., Prediction of ordered and disordered states in colloidal dispersions. *J. Chem. Soc. Faraday Trans.* 1976**,** *72* (0), 216-223.

103. van Megen, W.; Snook, I., A hard sphere model for order-disorder transitions in colloidal dispersions. *Chem. Phys. Lett.* 1975**,** *35* (3), 399-402.

104. Bengtzelius, U.; Gotze, W.; Sjolander, A., Dynamics of supercooled liquids and the glass transition. *J. Phys. C* 1984**,** *17* (33), 5915-5934.

105. Larson, R. G., *Structure and Rheology of Complex Fluids*. Oxford University Press: 1999.

106. Cockbain, E. G., The adsorption of sodium dodecyl sulphate at the oil-water interface and application of the Gibbs equation. *Trans. Faraday Soc.* 1954**,** *50* (0), 874-881.

107. Kanellopoulos, A. G.; Owen, M. J., Adsorption of sodium dodecyl sulphate at the silicone fluid/water interface. *Trans. Faraday Soc.* 1971**,** *67* (0), 3127-3138.

108. Brambilla, G.; El Masri, D.; Pierno, M.; Berthier, L.; Cipelletti, L.; Petekidis, G.; Schofield, A. B., Probing the equilibrium dynamics of colloidal hard spheres above the mode-coupling glass transition. *Phys. Rev. Lett.* 2009**,** *102* (8), 085703.

109. Braibanti, M.; Kim, H. S.; Şenbil, N.; Pagenkopp, M. J.; Mason, T. G.; Scheffold, F., The liquid-glass-jamming transition in disordered ionic nanoemulsions. *Sci. Rep.* 2017**,** *7* (1), 13879.

110. Maret, G.; Wolf, P. E., Multiple light scattering from disordered media. The effect of brownian motion of scatterers. *Z. Phys. B* 1987**,** *65* (4), 409-413.

111. Pine, D. J.; Weitz, D. A.; Chaikin, P. M.; Herbolzheimer, E., Diffusing wave spectroscopy. *Phys. Rev. Lett.* 1988**,** *60* (12), 1134-1137.

112. Scheffold, F.; Schurtenberger, P., Light scattering probes of viscoelastic fluids and solids. *Soft Mater.* 2003**,** *1* (2), 139-165.

113. Weitz, D. A.; Pine, D. J.; Pusey, P. N.; Tough, R. J. A., Nondiffusive Brownian motion studied by diffusing-wave spectroscopy. *Phys. Rev. Lett.* 1989**,** *63* (16), 1747-1750.

114. Zhang, C.; Reufer, M.; Gaudino, D.; Scheffold, F., Improved diffusing wave spectroscopy based on the automatized determination of the optical transport and absorption mean free path. *Korea Aust Rheol. J.* 2017**,** *29* (4), 241-247.

115. Squires, T. M.; Mason, T. G., Fluid mechanics of microrheology. *Annu. Rev. Fluid Mech* 2010**,** *42* (1), 413-438.

116. Hemar, Y.; Pinder, D. N., DWS microrheology of a linear polysaccharide. *Biomacromolecules* 2006**,** *7* (3), 674-676.

117. Oelschlaeger, C.; Cota Pinto Coelho, M.; Willenbacher, N., Chain flexibility and dynamics of polysaccharide hyaluronan in entangled solutions: A high frequency rheology and diffusing wave spectroscopy study. *Biomacromolecules* 2013**,** *14* (10), 3689-3696.

118. Mason, T. G.; Dhople, A.; Wirtz, D., Concentrated DNA rheology and microrheology. *MRS Proc.* 1997**,** *463*, 153 -158.

119. Mason, T. G.; Ganesan, K.; van Zanten, J. H.; Wirtz, D.; Kuo, S. C., Particle tracking microrheology of complex fluids. *Phys. Rev. Lett.* 1997**,** *79* (17), 3282-3285.

120. Xing, Z.; Caciagli, A.; Cao, T.; Stoev, I.; Zupkauskas, M.; O'Neill, T.; Wenzel, T.; Lamboll, R.; Liu, D.; Eiser, E., Microrheology of DNA hydrogels. *Proc. Natl. Acad. Sci. U.S.A.* 2018**,** *115* (32), 8137-8142.

121. Gisler, T.; Weitz, D. A., Scaling of the microrheology of semidilute F-actin solutions. *Phys. Rev. Lett.* 1999**,** *82* (7), 1606-1609.

122. Mason, T. G.; Gisler, T.; Kroy, K.; Frey, E.; Weitz, D. A., Rheology of F-actin solutions determined from thermally driven tracer motion. *J. Rheol.* 2000**,** *44* (4), 917-928.

123. Palmer, A.; Mason, T. G.; Xu, J.; Kuo, S. C.; Wirtz, D., Diffusing wave spectroscopy microrheology of actin filament networks. *Biophys. J.* 1999**,** *76* (2), 1063-1071.

124. Scheffold, F.; Díaz-Leyva, P.; Reufer, M.; Ben Braham, N.; Lynch, I.; Harden, J. L., Brushlike interactions between thermoresponsive microgel particles. *Phys. Rev. Lett.* 2010**,** *104* (12), 128304.

125. Cardinaux, F.; Cipelletti, L.; Scheffold, F.; Schurtenberger, P., Microrheology of giant-micelle solutions. *Europhys. Lett.* 2002**,** *57* (5), 738.

126. Oelschlaeger, C.; Schopferer, M.; Scheffold, F.; Willenbacher, N., Linear-to-branched micelles transition: A rheometry and diffusing wave spectroscopy (DWS) study. *Langmuir* 2009**,** *25* (2), 716-723.

127. Willenbacher, N.; Oelschlaeger, C.; Schopferer, M.; Fischer, P.; Cardinaux, F.; Scheffold, F., Broad bandwidth optical and mechanical rheometry of wormlike micelle solutions. *Phys. Rev. Lett.* 2007**,** *99* (6), 068302.

128. Xue, J. Z.; Pine, D. J.; Milner, S. T.; Wu, X. l.; Chaikin, P. M., Nonergodicity and light scattering from polymer gels. *Phys. Rev. A* 1992**,** *46* (10), 6550-6563.

129. Romer, S.; Scheffold, F.; Schurtenberger, P., Sol-gel transition of concentrated colloidal suspensions. *Phys. Rev. Lett.* 2000**,** *85* (23), 4980-4983.

130. Scheffold, F.; Skipetrov, S. E.; Romer, S.; Schurtenberger, P., Diffusing-wave spectroscopy of nonergodic media. *Phys. Rev. E* 2001**,** *63* (6), 061404.

131. Schurtenberger, P.; Bissig, H.; Rojas, L.; Vavrin, R.; Stradner, A.; Romer, S.; Scheffold, F.; Trappe, V., Aggregation and gelation in colloidal suspensions: Time-resolved light and neutron scattering experiments. In *Mesoscale Phenomena in Fluid Systems*, American Chemical Society: 2003; Vol. 861, pp 143-160.

132. Viasnoff, V.; Lequeux, F.; Pine, D. J., Multispeckle diffusing-wave spectroscopy: A tool to study slow relaxation and time-dependent dynamics. *Rev. Sci. Instrum.* 2002**,** *73* (6), 2336-2344.

133. Zakharov, P.; Cardinaux, F.; Scheffold, F., Multispeckle diffusing-wave spectroscopy with a single-mode detection scheme. *Phys. Rev. E* 2006**,** *73* (1), 011413.

134. Gang, H.; Krall, A. H.; Weitz, D. A., Thermal fluctuations of the shapes of droplets in dense and compressed emulsions. *Phys. Rev. E* 1995**,** *52* (6), 6289-6302.

135. Kim, H. S.; Scheffold, F.; Mason, T. G., Entropic, electrostatic, and interfacial regimes in concentrated disordered ionic emulsions. *Rheol. Acta* 2016**,** *55* (8), 683-697.

136. Qiu, X.; Wu, X. L.; Xue, J. Z.; Pine, D. J.; Weitz, D. A.; Chaikin, P. M., Hydrodynamic interactions in concentrated suspensions. *Phys. Rev. Lett.* 1990**,** *65* (4), 516-519.

137. Hansen, J.-P.; McDonald, I. R., *Theory of Simple Liquids (4th edition)*. Academic Press: Oxford, 2013.

138. Ladd, A. J. C.; Gang, H.; Zhu, J. X.; Weitz, D. A., Time-dependent collective diffusion of colloidal particles. *Phys. Rev. Lett.* 1995**,** *74* (2), 318-321.

139. Nägele, G., On the dynamics and structure of charge-stabilized suspensions. *Phys. Rep.* 1996**,** *272* (5), 215-372.

140. Fraden, S.; Maret, G., Multiple light scattering from concentrated, interacting suspensions. *Phys. Rev. Lett.* 1990**,** *65* (4), 512-515.

141. Rojas, L. F.; Vavrin, R.; Urban, C.; Kohlbrecher, J.; Stradner, A.; Scheffold, F.; Schurtenberger, P., Particle dynamics in concentrated colloidal suspensions. *Faraday Discuss.* 2003**,** *123* (0), 385-400.

142. Gómez-Medina, R.; Froufe-Pérez, L. S.; Yépez, M.; Scheffold, F.; Nieto-Vesperinas, M.; Sáenz, J. J., Negative scattering asymmetry parameter for dipolar particles: Unusual reduction of the transport mean free path and radiation pressure. *Phys. Rev. A* 2012**,** *85* (3), 035802.

143. Rojas-Ochoa, L. F.; Mendez-Alcaraz, J. M.; Sáenz, J. J.; Schurtenberger, P.; Scheffold, F., Photonic properties of strongly correlated colloidal liquids. *Phys. Rev. Lett.* 2004**,** *93* (7), 073903.

144. Lionberger, R. A.; Russel, W. B., High frequency modulus of hard sphere colloids. *J. Rheol.* 1994**,** *38* (6), 1885-1908.